Micro-Welding of Nitinol Shape Memory Alloy

by

Billy Tam

A thesis
presented to the University of Waterloo
in fulfillment of the
thesis requirement for the degree of
Master of Applied Science
in
Mechanical Engineering

Waterloo, Ontario, Canada, 2010

I hereby declare that I am the sole author of this thesis. This is a true copy of the thesis, including any required final revisions, as accepted by my examiners.

Billy Tam

I understand that my thesis may be made electronically available to the public.

Billy Tam

Abstract

Nitinol shape memory alloys have revolutionized many traditional engineering designs with the unique properties of pseudoelasticity and shape memory effect. At the present moment, primary fabrication processes for Nitinol-based devices include laser cutting and manual techniques. As the interest in incorporating Nitinol in different micro applications and devices increases, the development of effective technology for micro-welding of Nitinol becomes necessary. In general, welding processes may induce significant changes to the processed area rendering the component incompatible or unusable. Strength reduction, inclusions of intermetallic compounds, and changes in pseudoelastic and shape memory effects are all examples of how Nitinol can be affected by welding.

The current study has examined the effects of two welding techniques on Nitinol: micro-resistance spot welding (MRSW) and laser micro-welding (LMW). Ni-rich Nitinol wires were welded in a crossed-wire configuration at different energy inputs by varying welding currents for MRSW and peak powers for LMW. The characterization of weld properties focused on the mechanical properties and bonding mechanisms, weld microstructure and formation, and phase transformation temperatures. Additionally, the effects of surface oxide on joint performance were also examined.

During MRSW, the primary bonding mechanism was solid state, which consisted of 6 main stages: cold collapse, dynamic recrystallization, interfacial melting, squeeze out, excessive flash, and surface melting. Attempt was made to correlate the joining mechanism with the contact resistances. Joint strength and fracture mechanism were closely linked to the metallurgical properties of the welds. Finally, differential scanning calorimetry (DSC) tests showed that weld metal underwent phase transformation at lower temperatures compared to base material.

The second part of this study investigated the effects of Nd:YAG laser micro welding have on Nitinol wires. The fracture strength, weld microstructure, and phase transformation temperatures resulting from the use of varying peak power inputs were studied and compared to both base metal and welds produced using the MRSW process. Results showed good retention of base metal strength and pseudoelastic properties. Moreover, the fusion zone underwent phase transformation at higher temperatures compared to base metal, which substantially altered the active functional properties of Nitinol at room temperature.

Acknowledgements

I would like to express my sincere thanks to my academic supervisors, Professor Y. Norman Zhou and Mohammad Ibraheem Khan for their continual support and guidance throughout my graduate research and education experience. Their dedication to excellence has been a source of inspiration and motivation. Their influences have touched me academically, professionally, and personally.

Funding of this work was provided by National Science and Engineering Research Council (NSERC).

I would like to thank members from the Centre for Advanced Materials Joining (CAMJ) at the University of Waterloo for making this experience so memorable. Special thanks extended to Dr. Wen Tan and Siu Kei Tang for their inputs and assistance.

Finally, I am indebted to my family, friends and loved ones for the unprecedented cares and encouragement given to me during my university experience.

To my family.

Table of Contents

List of Figures

List of Tables

Chapter 1: Introduction

1.1 Background

NiTi or Nitinol shape memory alloys (SMA) were first discovered in the 1959, but commercial applications have only recently begun, as fundamental understanding of their behaviour has improved. The unconventional properties of this alloy, pseudoelasticity and shape memory effects, are what drives their use in a wide variety of applications such as medical devices, aerospace applications and micro-electrical-mechanical systems (MEMS). To date, Nitinol provides the best combination of shape-memory material properties for commercial applications [1]. One market where Nitinol really excels in is the medical device industry due to the excellent biocompatibility, where the alloy is used for bone brackets, surgical staples, vascular stents, orthodontic arch wires and many more [1-3]. As the complexity of Nitinol-based devices continues to increase, other processing methods such as welding are required to help meet these expectations. For example, electrical connection, component integration, and hermitical sealing are areas where welding is more desired compared to other manufacturing processes.

1.2 Micro-Welding of NiTi

At the present moment, manufacturing processes for Nitinol-based devices include laser cutting and special hot/cold shaping techniques due to lack of understanding of the alloy's fabricability [4]. With increased demands for finer and more complex devices, advancement in effective processing methods becomes necessary. Therefore, the development of effective micro-welding of NiTi is an integral part of the future success of manufacturing of these Nitinol-based devices. However, welding processes can cause localized changes in the processed area, yielding properties that differ from the original material, and the severity of change can

escalate for a thermomechanical alloy like Nitinol. Strength reduction, inclusions of intermetallic compounds, and altered pseudoelastic and shape memory effects properties are all examples of how Nitinol can be affected by welding [4-14].

Micro-resistance spot welding (MRSW) and laser micro-welding (LMW) of crossed-wires are two commonly used processes for electrical interconnection and component integration for miniature devices such as pacemakers [15]. Thus far, literature has shown that process parameters can greatly influence the welding behaviour of Nitinol [5]. However, the microstructures and mechanical properties of welded Nitinol have not been examined in sufficient detail. Furthermore, previous studies on welding Nitinol wires have been restricted to spot melting or butt joint, which do not reflect the crossed-wire geometry generally used in applications. The aims of this research are to evaluate the effect of MRSW and LMW on the mechanical and metallurgical behaviours of welded crossed Nitinol wires.

1.2.1 Micro-Resistance Spot Welding (MRSW) of NiTi

The existing publications on resistance micro-welding of Nitinol are limited and most of them are in the form of feasibility studies; none have been reported for micro-resistance spot welding of crossed-wires. There are a few reported studies on resistance butt-weld Nitinol wires that showed solid-state bonding in addition to good retention of base metal strength and intrinsic shape memory effect property [11-12]. On the other hand, the work by Hall on resistance welded lap joints of Nitinol wires showed fusion welding [13]. The joining mechanism is greatly influenced by the generation of resistive heat at the interface, which is dictated by various process parameters and material properties [15-20]. However, there remains a lack of fundamental understanding and systematic analysis on the joining mechanism of MRSW of NiTi and the welding effects on material properties.

It is widely known that the functional properties of Nitinol are extremely sensitive to thermomechanical processing, in which MRSW can be included. Modifications to base metal transformation behaviours [21-23] and previous strengthening heat treatments [24-25] have

been shown to occur during the application of heat or mechanical deformation. For example, Kurita *et al.* [21] showed cold working widened the temperature range over which transformation occurred while Frick *et al.* [22] detailed the aging effects on hot-rolled and cold-rolled Nitinol. Similarly, various studies have successfully utilized Direct Electric Resistance Heat Treatment (DERHT) to modify hardness and stress-strain responses [24-25]. All of the aforementioned publications emphasized that the functional properties of Nitinol are sensitive to thermal and mechanical treatments, similar to those experienced during MRSW. Therefore, the changes induced by welding must be thoroughly understood in order to refine the protocol for achieving functional welds.

1.2.2 Laser Micro-Welding (LMW) of NiTi

Laser micro welding (LMW) is extensively used in manufacturing because of the advantages in welding complex geometries and special materials [26-27]. However, LMW of Nitinol is considered difficult because its functional properties (pseudoelasticity and shape memory effect) are sensitive to change due to thermal effects and chemical contamination, which laser welding can induce [4-10].

To date, there are limited studies detailing the mechanical properties of neodymium-doped yttrium aluminium garnet (Nd:YAG) laser welded Nitinol. In general, laser welded Nitinol exhibited good retention of base material strength [4, 6-7]. However, different results were reported regarding the pseudoelastic properties and fracture mechanisms. For example Schlossmacher *et al.* investigated Nd:YAG laser welding of Nitinol sheets, and observed no deterioration in pseudoelasticity and found that fracture occurred in a ductile manner [6]. In contrast, a study on Nd:YAG butt welded Nitinol wires conducted by Yan *et al.* reported a lower critical stress for stress-induced martensite (SIM) transformation and an increased residual strain upon unloading while observing a brittle fracture in the weld [4]. Similarly, a study by Ogata *et al.* reported that a brittle fracture mode occurred [7].

The functional properties (pseudoelasticity and shape memory effect) of Nitinol are strongly linked to its ability to transform between martensite and austenite. An earlier report by Hsu *et al.* observed a slight decrease in transformation temperature after CO_2 laser welding of Nitinol [8]. On the other hand, Ogata *et al.* and Tussi *et al.* showed minimal effect of laser welding on transformation temperatures [7, 9]. Falvo *et al.* stated that laser welding modified base material in a manner similar to solution treatment, removing the effect of previous thermomechanical processing [10]. Recently, Yan *et al.* observed laser welded wires began martensitic transformation 50 ^{o}C higher than base metal [4]. Similarly, Khan and Zhou clearly identified a distinct phase transformation behaviour in Nd:YAG laser processed Nitinol through work in differential scanning calorimetry (DSC), x-ray diffraction (XRD), and transmission electron microscopy (TEM), which effect could be translated to the mechanical properties [14]. Discrepancies in results suggest more work is required in this field as modifications to the mechanical and transformation behaviours in the welded region can significantly impede the usefulness of laser welding of Nitinol.

1.3 Objectives

The objective of this thesis is to methodically study the weldability of crossed Nitnol wires using the LMW and MRSW processes. It is split into three sub-objectives:

1. Observe and describe the joining mechanisms and weld morphology of welds produced from the two processes via metallographic examinations.
2. Determine the mechanical performance of Nitinol welds using the LMW and MRSW processes through micro-tensile tests as a function of energy input. Investigate the fracture mechanism and correlate it to fracture surface morphology and weld formation.
3. Examine the modification to phase transformation temperatures induced by welding using DSC tests and XRD analysis.

1.4 Thesis Outline

This dissertation is organized into six chapters. Chapter 2 reviews the material science of Nitinol and the fundamentals of laser and resistance welding. In Chapter 3 the experimental setup and conditions along with the performance testing are detailed. Chapter 4 examines MRSW of crossed Nitinol wires while Chapter 5 explores welds produced using the pulsed Nd:YAG LMW process. Finally, concluding statements for this work and recommendations for future work are presented in Chapter 6.

Chapter 2: Literature Review

2.1 Nitinol Shape Memory Alloy

Nitinol is an intermetallic compound (IMC) consisting of equiatomic or near equiatomic nickel and titanium. The unique properties of this alloy were first observed in 1960s at the Naval Ordnance Laboratory (NOL), from which the acronym Ni-Ti-NOL was created [1]. Unlike conventional IMCs, the alloy belongs to a class of special materials called shape memory alloys (SMA) and when properly processed, exhibits pseudoelastic and shape memory properties. It offers several advantages over other shape memory alloys (Cu-Zn-Al, Cu-Al-Ni, and Au-Cd) such as low elastic anisotropy, high electrical resistivity, and good corrosion resistance [1]. Since its discovery, Nitinol has revolutionized many traditional engineering designs with greater functional capacity such as stents and actuators.

The basics of pseudoelasticity and the shape memory effect are closely linked to the diffusionless solid-state phase transformation, also known as the martensitic transformation. Austenite is the high temperature phase with a simple cubic B2 crystal structure (Figure 2.1a) and martensite is the low temperature phase with a monoclinic B19' crystal structure (Figure 2.1b). In Nitinol, transformation involves no diffusional atomic migration and therefore is independent of time [1]. Phase transformations can occur between -150 ^{o}C and 200 ^{o}C, limited by the material and are generally described by four temperatures: martensite start (M_s), martensite finish (M_f), austenite start (A_s) and austenite finish (A_f), which can be determined by DSC [1, 28-29]. They are temperatures at which the martensite to austenite transformation and the reverse transformation begin and complete (Figure 2.2). Onset temperatures, M_s and A_f are generally accepted for classification. A hysteresis with a magnitude of 10 ^{o}C to 50 ^{o}C generally exists, which the width can be associated to the frictional force endured during lattice movement across interfaces and defects [1]. In other words, transformation occurs at different

temperatures during cooling and heating. The two phases of Nitinol have different material properties such as Young's modulus, electrical resistivity and thermal conductivity [2].

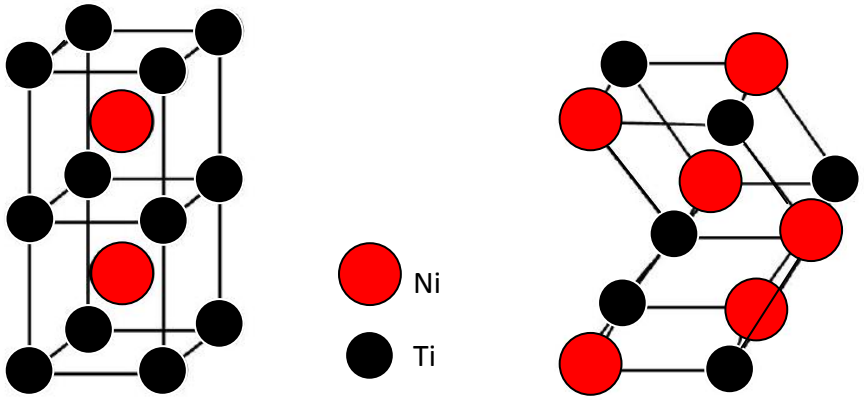

Figure 2.1: Lattice structure of (a) austenite and (b) martensite

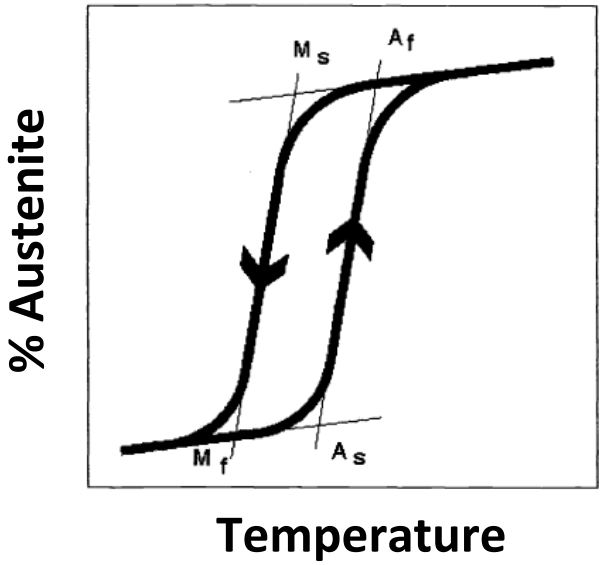

Figure 2.2: Schematic of percent austenite as a function of temperature

2.1.1 Martensitic Transformation

To understand the unique mechanical behaviours of Nitinol, it is necessary to become familiar with the principles of martensite and its formation [1]. During thermally-induced martensitic

transformation in steel, atomic rearrangement in the new phase inherits a different shape and volume. Nitinol differs by undergoing only a shape change. This macroscopic change in dimension has to be self-accommodated by either slip or twinning. Slippage of lattice plane is an irreversible process, which is capable of accommodating both shape and volume changes (Figure 2.3a). Twinning only accommodates a shape change, but is reversible (Figure 2.3b) and Nitinol is of the latter type.

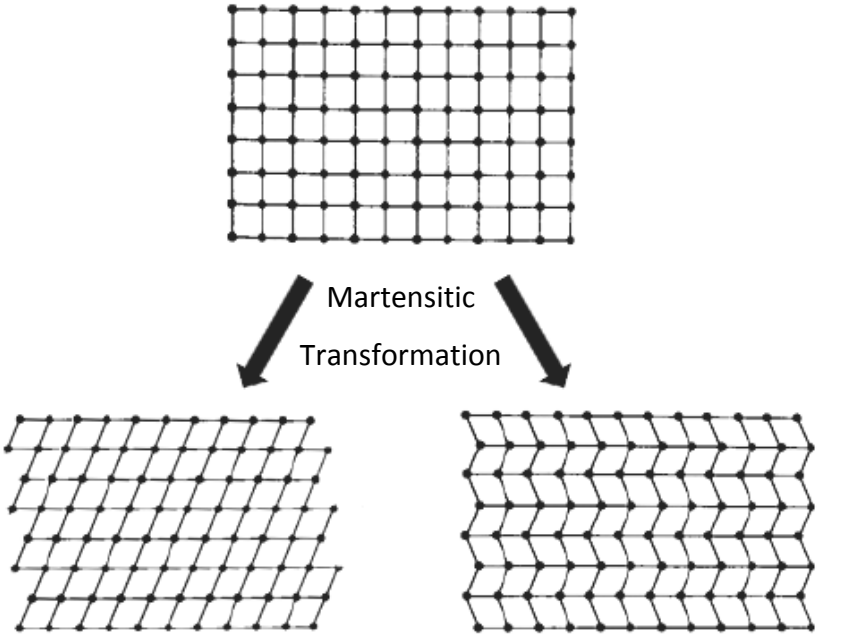

(a) accommodation by slip (b) accommodation by twinning

Figure 2.3: Schematic representation of the atomic motions associated to the self-accommodation step of a martensitic transformation: (a) by slip and (b) by twinning [1]

Twinning is the creation of mirrored structures as a result of atomic displacement across a particular atomic plane [1]. Atoms situated at the twin boundary see the same number and types of bonds in both directions [1]. As oppose to accommodation by slip, bonds are not broken during the twinning process. For this reason, twin boundaries have low energy and are highly mobile. They can reorient themselves from one orientation to another in favour of the direction of stress applied, also known as detwinning [1, 30]. During reorientation of the martensitic structure from twin variants to a single variant (Figure 2.4), a large amount of strain

can be produced. This unusual mechanical response is macroscopically represented by a stress plateau in a stress-strain curve (Figure 2.5). The twin movement process can only accommodate a certain amount of martensitic deformation and exceeding it will result in permanent plastic deformation of the structure.

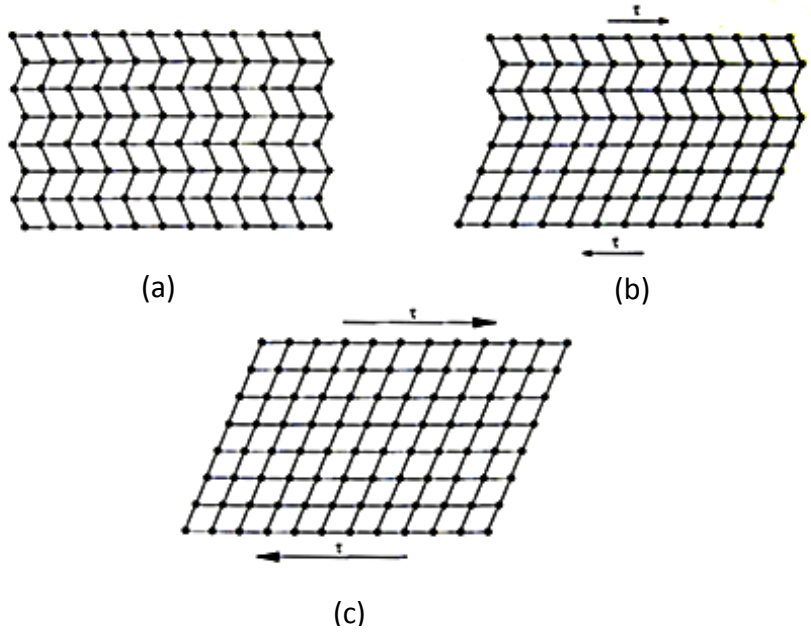

Figure 2.4: During the application of a shear stress, the twin structure can readily move to accommodate the strain by undergoing a detwinning process [1]

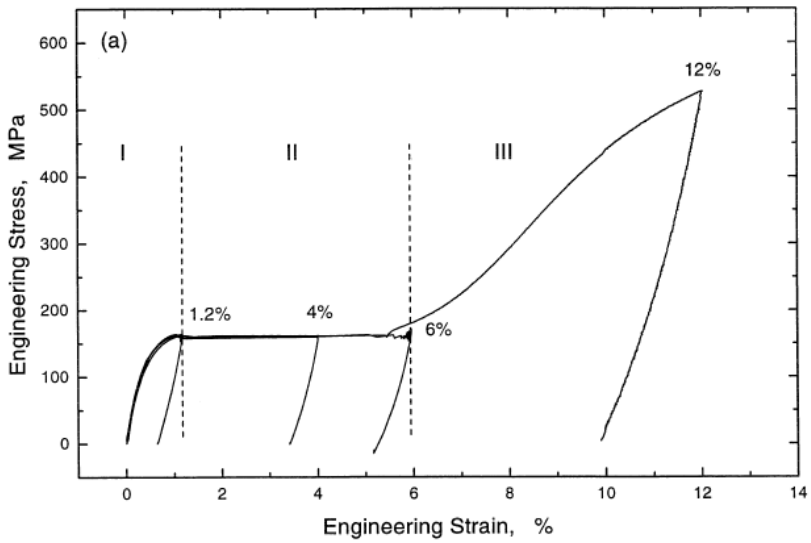

Figure 2.5: Deformation of NiTi under tension to several strains and subsequent unloading [32]

2.1.2 Shape Memory Effect

Shape memory effect is the ability to revert back to the original shape upon heating, after an apparent plastic deformation to the material, which is illustrated using Figure 2.6. Twinned martensite has the ability to accommodate large amounts of strain by undergoing detwinning, resulting in a biased distribution of martensite variants (Figure 2.4b) or in the extreme case, a single variant (Figure 2.4c) [1]. The strain is recovered upon heating above A_f when it phase transforms to austenite. The original shape is recovered because austenite is a symmetrical single variant structure [1]. Subsequent cooling below M_f allows the twinned martensite to be formed again. The process is repeatable as long as the stress applied is kept below the threshold where plastic deformation occurs, for example in region III of Figure 2.5.

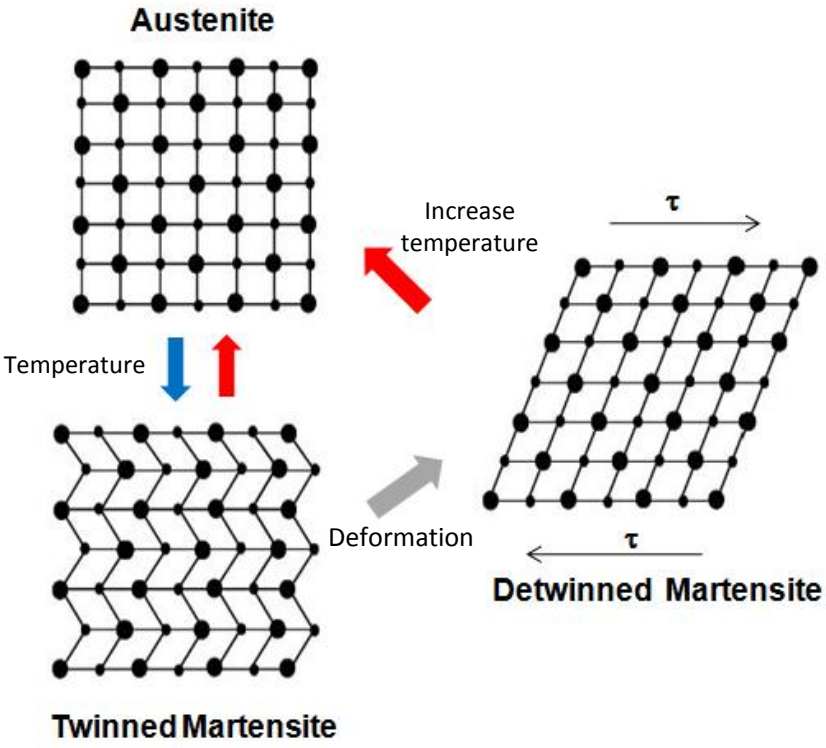

Figure 2.6: Crystallographic representation of shape memory effect

2.1.3 Stress-induced Phase Transformation and Pseudoelasticity

Martensitic transformation is a thermoelastic process, meaning martensite can be stabilized by temperature or by stress. When stress is the stabilizing agent, the martensite formed is termed stress-induced martensite (SIM). Similarly, SIM can accommodate stress readily due to its

multi-variant twinned structure [1]. The mechanical response is similar to detwinning; however, the underlying activity is slightly different and can be divided into three regions, shown in Figure 2.7. Initially austenite is elastically deformed obeying Hooke's Law (1). Upon reaching a critical stress, SIM is progressively being formed until the parent phase is fully consumed (2). The plateau is a result of the transformation from austenite to a variant of martensite predetermined by the direction of stress applied. The magnitude of strain during SIM formation can reach more than 8%. Subsequent application of stress would result in the elastic and ultimately plastic deformation of the detwinned martensite, again obeying Hooke's Law but governed by the martensitic modulus (3). Upon removal of stress within region 2, reverse transformation occurs at a lower stress, corresponding to the transformational hysteresis [31]. This mechanical response is referred as pseudoelasticity, which describes the nonlinear recoverable deformation behaviour of austenitic Nitinol.

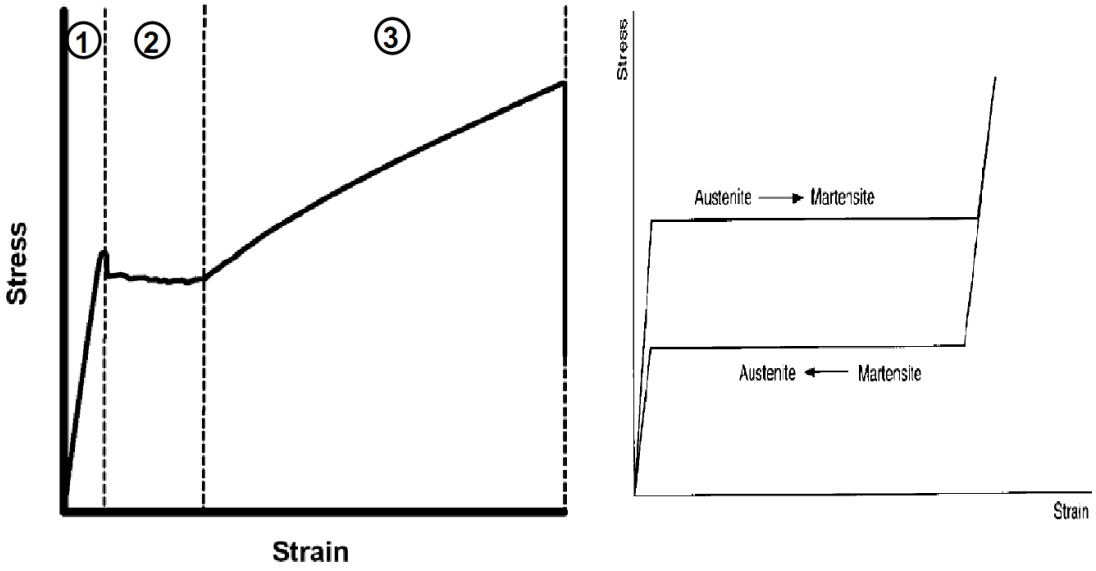

Figure 2.7: Stress-strain curves of Nitinol exhibiting pseudoelasticity; it begins with the (1) elastic response of austenite, followed by (2) stress-induced transformation, and (3) elastic and plastic deformation of martensite. [32]

The stable phase at the working temperature dictates which functional property is active. This dependence of temperature is shown in Figure 2.8. Below M_f, the temperature at which the

phase transformation to martensite is completed, the predominant functional property is the shape memory effect. Pseudoelasticity is only observed at temperatures above A_f but below the martensite deformation temperature (M_d), the highest temperature at which martensite will form from austenite in response to applied stress [28]. Austenite becomes more stable at higher temperature, thereby increasing the stress required to produce SIM, as shown in Figure 2.9. Above M_d, the critical stress exceeds the stress that would cause permanent yielding in austenite. At temperatures where the transformation is partially completed such as between M_s and M_f or A_s and A_f, the two phases will co-exist. Additionally, SIM generally occurs at higher stresses than detwinning of martensite because martensite in Nitinol is much softer than austenite.

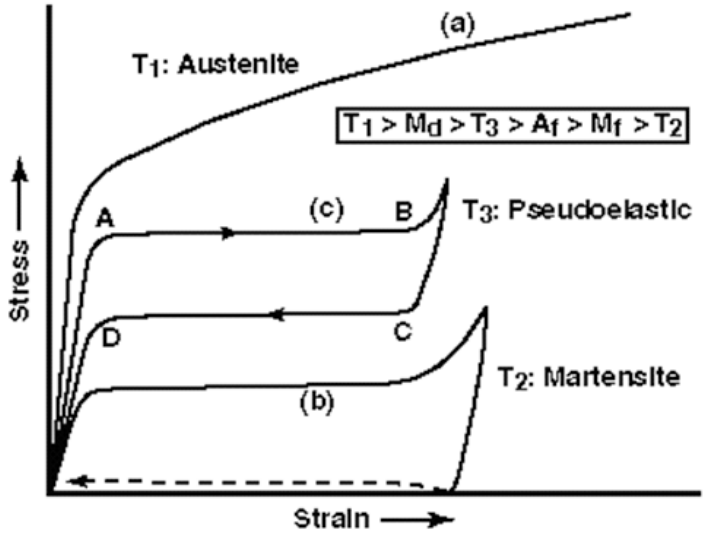

Figure 2.8: Hypothetical stress-strain curves of Nitinol conducted at different temperatures: (a) T_1 is above M_d, (b) T_3 is above A_f but below M_d, and (c) T_2 is below M_f.

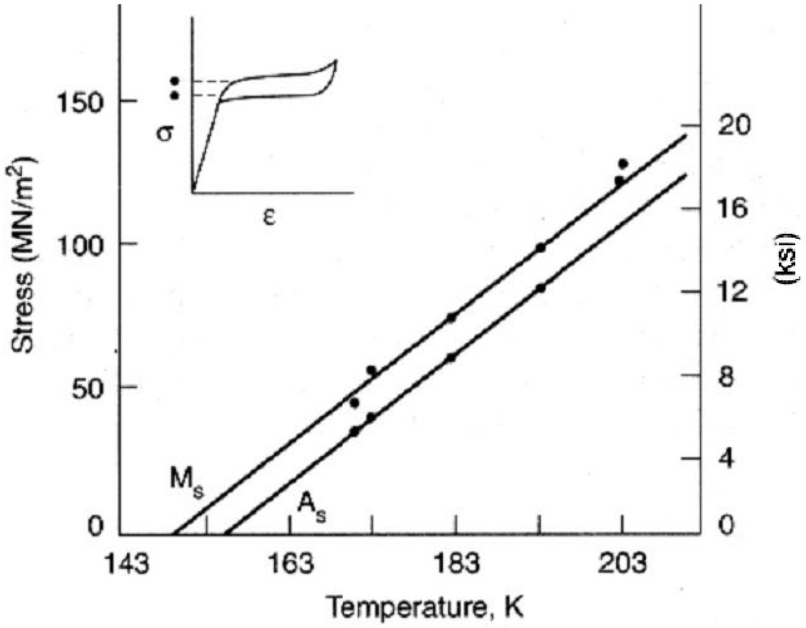

Figure 2.9: Temperature dependence of transformation stress [1]

2.1.4 Ni-Ti Phase Diagram

Figure 2.10 shows the phase diagram of nickel and titanium: the IMC of Ni and Ti is situated near 50 at.% Ni. Nitinol is a non-stoichiometric intermetallic compound, typically categorized as Ti-rich or Ni-rich. NiTi is bounded by Ti_2Ni and $TiNi_3$ phases, but studies have revealed the existence of metastable IMCs of Ti_3Ni_4 and Ti_2Ni_3 in the Ni-rich side after short duration of heat treatment at intermediate temperatures (300 ^{o}C to 600 ^{o}C) [33-36]. The solubility limit at the Ti-rich side is nearly vertical with composition close to 50 at.% Ni whereas on the Ni-rich side, the solubility of nickel increases rapidly with higher temperature beginning at approximately 500 ^{o}C. This higher solubility allows solid solutions of NiTi of different Ni contents to be formed [33].

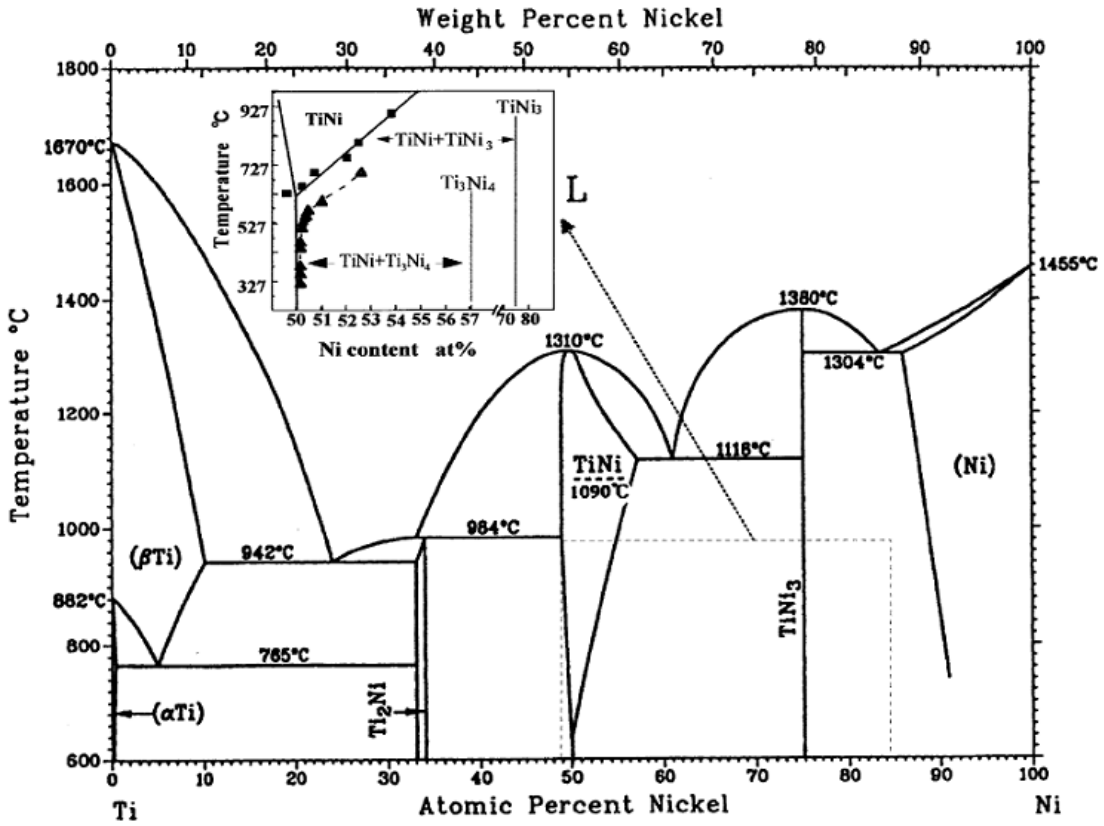

Figure 2.10: Ni-Ti phase diagram [33]

2.1.5 Transformation Temperatures

Phase transformation temperatures are a function of chemistry and thermomechanical processing. For Nitinol in its solid solution state, increasing Ni content results in lower transformation temperatures. Figure 2.11 shows the dependence of transformation temperature on Ni content. Ti-rich alloys are less sensitive to chemistry change because of the inability to dissolve excess Ti. In contrast on the Ni-rich side, M_s temperature can change from 50 ^{o}C to -150 ^{o}C within 1 at. % difference in Ni chemistry. Transformation temperatures based on chemistry are referred to as the intrinsic phase transformation temperatures.

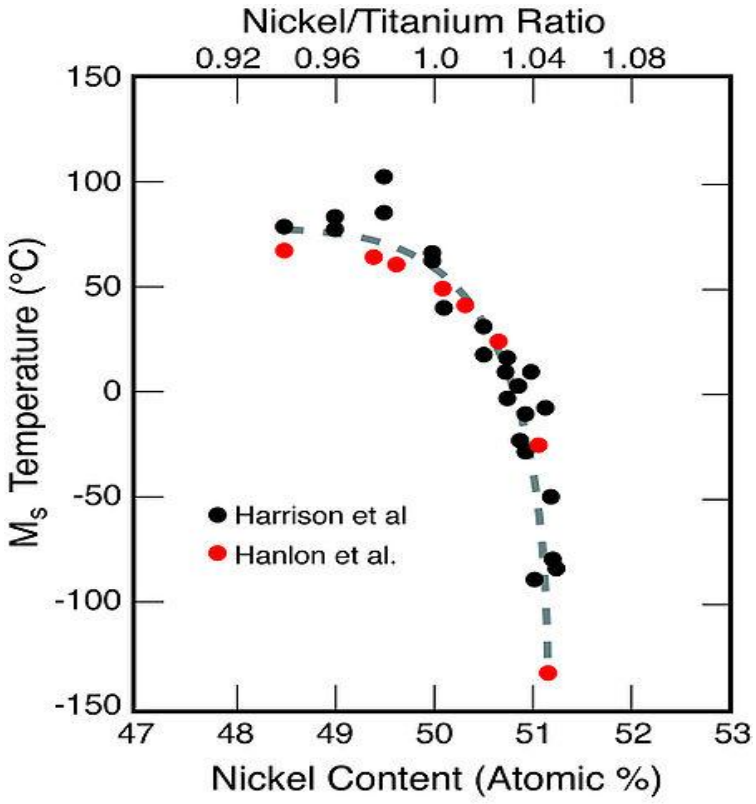

Figure 2.11: The dependence of M_s transformation temperature on Ni content

Thermomechanical processing is an effective way to modify the phase transformation behaviours of Nitinol, a technique often employed to achieve better mechanical properties. Cold-working gives higher yield strength, but it destroys the shape memory effect and pseudoelasticity as random dislocations would hinder the mobility of twin boundaries. Cold working can permanently deform the detwinned structure, reducing the latent heat of transformation and broadening the temperatures at which transformation occurs [21, 34-36]. Therefore, cold-working is generally coupled with heat treatment to increase toughness as well as to "restore" the memory effect by removing some of the lattice strain [1]. However, heat treatment at different temperatures and times can induce the precipitation of Ti_2Ni in the Ti-rich side, and Ti_3Ni_4, Ti_2Ni_3 and $TiNi_3$ in the Ni-rich side. Precipitation of IMCs can modify the chemistry, which effectively changes the intrinsic phase transformation temperatures [33]. Moreover, a 2 stage phase transformation between martensite, an intermediate phase referred

as R-phase, and austenite can be introduced after aging [33, 37]. A detailed description of R-phase and its development can be very complex and is beyond the scope of this thesis. Nonetheless, it can be seen from Figure 2.12 and Figure 2.13 that the phase transformation behaviours of Nitinol can be altered significantly via different thermomechanical treatments.

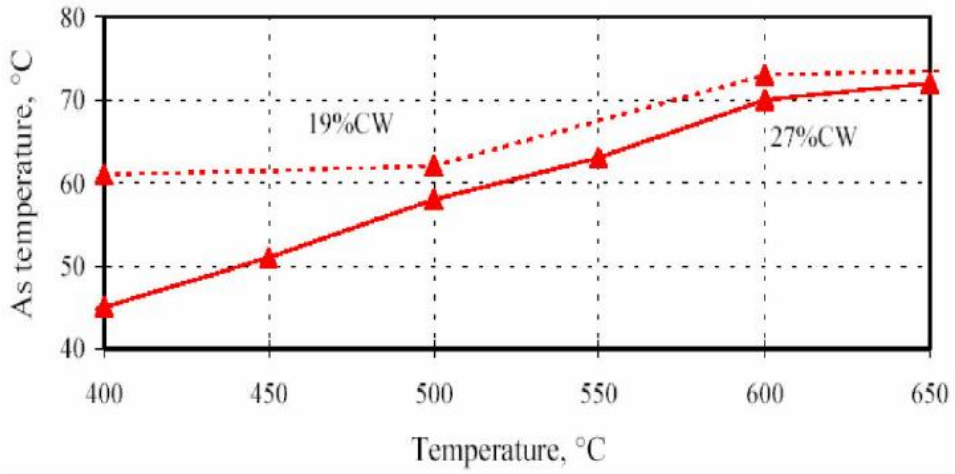

Figure 2.12: The dependence of A_s temperature on the amount of cold-working (CW) and subsequent heat treatment at various temperatures

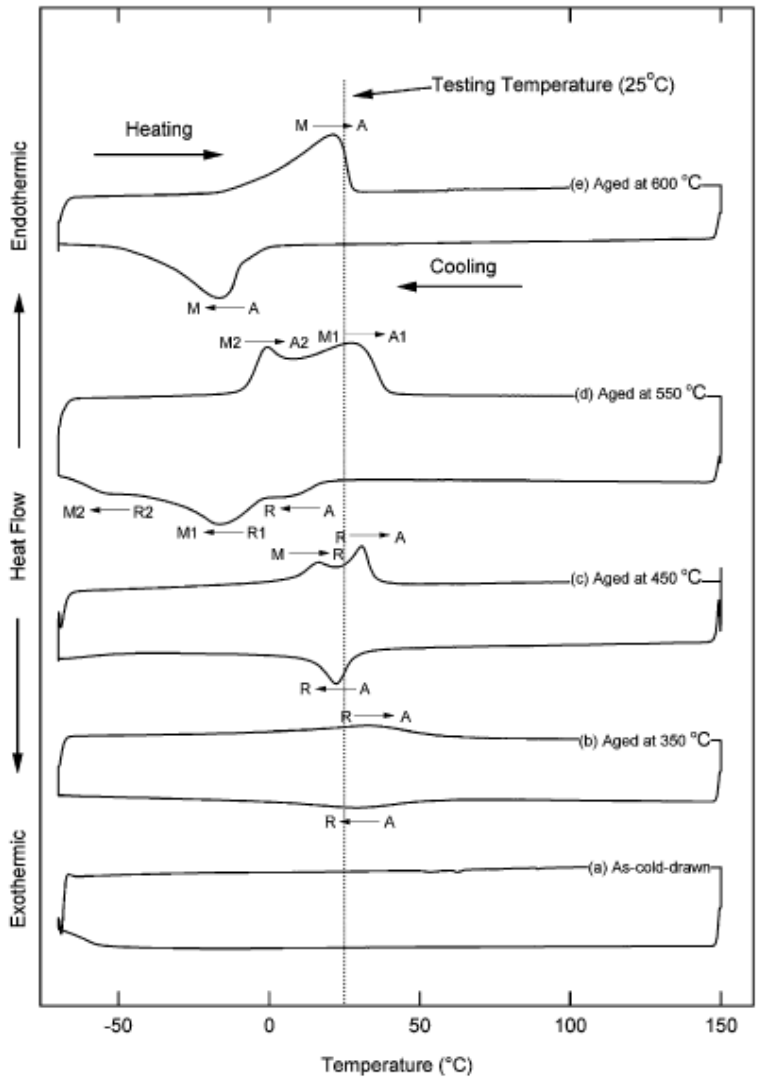

Figure 2.13: DSC curves of cold-drawn Nitinol after different heat treatments [34]

2.2 Laser Fundamentals

The word LASER is an acronym that stands for Light Amplification by Stimulated Emission of Radiation. The emitted light is spatially and temporally coherent with very low diffraction, and can be coupled with transmittance optics to focus the high intensity beam to a single spot of high energy density [26-27].

A laser system consists of three main components: (1) amplifying medium, (2) means of exciting the medium to its amplifying state or pump source and (3) an optical resonator [27]. The active medium is comprised of special materials that when excited produce energy-carrying photons of specific wavelengths. The pump source is determined by the type of active medium used. Examples of pump sources include flash lamps and electrical discharges for Nd:YAG and CO_2 medium, respectively [27]. The optical resonator, in the simplest form, is two parallel mirrors, one fully and one partially reflective, placed around the active medium to filter and transmit photons that fully satisfy specific conditions for oscillation [27].

As suggested by the acronym, stimulated emission is the primary mechanism responsible for light amplification. It creates population inversion, a required state for laser operation that exists when the number of photons being amplified per unit time is greater than the number of photons being absorbed [27, 38-39]. There are generally two scenarios in which photons can be emitted: spontaneous emission and stimulated emission. The former describes a one to one ratio of photon emission to electron relaxation (Figure 2.14). In stimulated emission, the incident photon collides with another energized atom causing an emission of another photon of equal frequency, phase polarization, and direction of travel (Figure 2.15) [38].

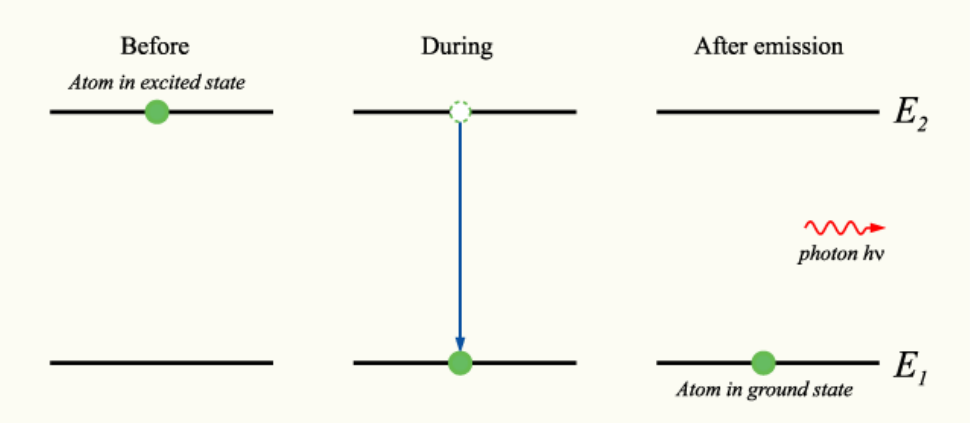

Figure 2.14: Schematic of spontaneous emission [40]

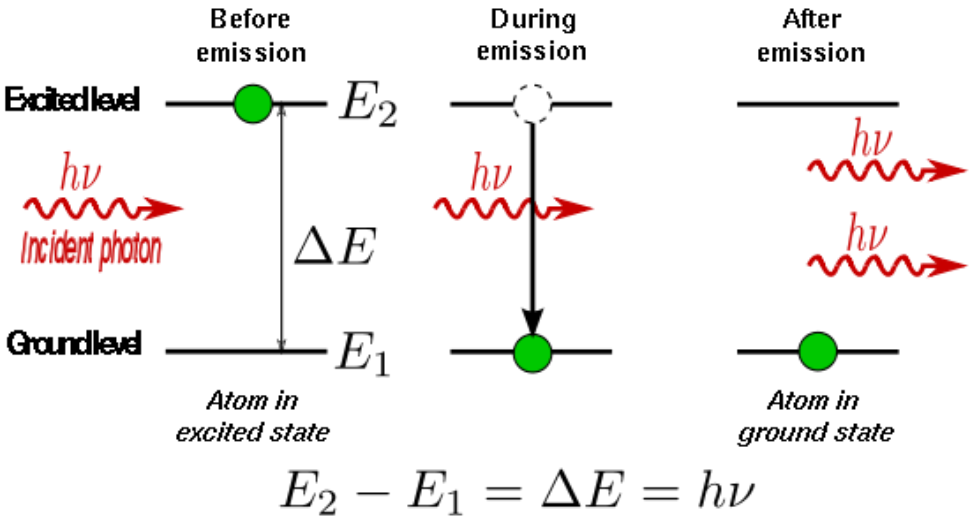

Figure 2.15: Schematic of stimulated emission [41]

During the operation of a laser, atoms are energized from the ground state to the excited state by pumping. Incoherent photons are emitted when the atoms relax back to the ground state. Photons that do not travel parallel to the optical axis of the laser are quickly lost in the resonator while photons that travel parallel to the optical axis are oscillated in the resonator with the possibility of inducing stimulated emission, from which a coherent photon is created [27]. Further populating monochromatic and unidirectional photons produces the highly energetic laser suitable for welding.

2.2.1 Small Scale Pulsed Nd:YAG laser welding

Pulsed Nd:YAG laser welding is a commonly used fusion welding technique to produce deep welds with low average heat input. Commercially available Nd:YAG lasers are generally rated with an average output powers of 0.3 kW to 3 kW, ideal for small scale use [27].

A schematic layout of a Nd:YAG laser system is shown in Figure 2.16. The cavity assembly is composed of an active medium, pumping source, and resonator. When excited, an yttrium aluminum garnet (YAG) crystal doped with neodymium (Nd) atoms produces photons with a wavelength of 1064 nm [27]. Excitation radiation is pumped using flash lamps. The laser

output is transmitted through the input coupling optic and into an optical fiber that connects to the working head before being delivered to the workpiece.

The Nd:YAG laser offers several advantages over other laser systems. The ability to deliver photons via fiber is advantageous for fabrication of complex components. Other advantages include higher processing efficiency, ability to create narrow welds with small heat affected zones (HAZ), weld special materials such as titanium and quartz [26-27].

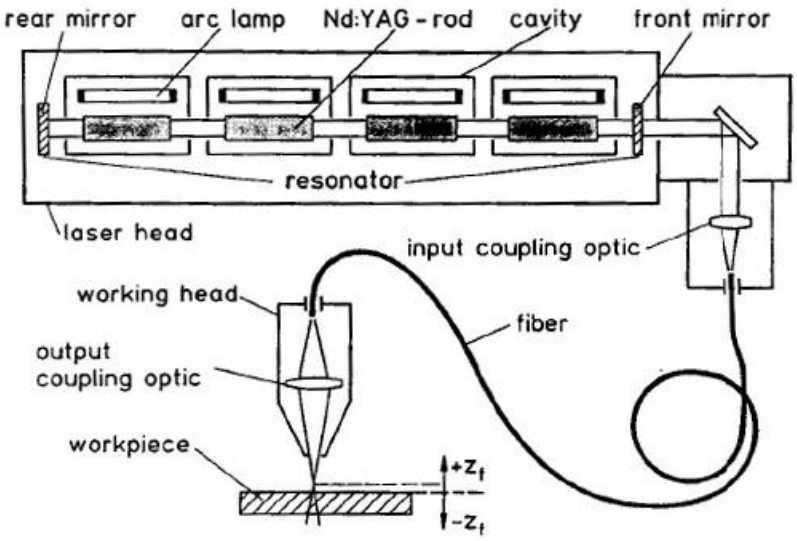

Figure 2.16: Schematic of Nd:YAG laser setup [26]

2.2.2 Welding Parameters

Several key parameters are used to define the laser pulses produced by a Nd:YAG laser. In spot welding, individual pulses are defined by peak power and pulse width. In seam welding, the amount of overlap between individual pulses is controlled by frequency and weld speed. Average power and pulse energy are for process feedback [31]. Figure 2.17 is a schematic of a temporal profile of laser pulses produced with the Nd:YAG laser process. Peak power is the max power of the laser pulse will outputted and weld width is the duration of the laser pulse, which typically ranges between 0.2 to 20 ms. Pulse energy is determined by the area under each laser pulse in Figure 2.17. Average power is the amount of energy averaged to a second,

which is normally used to conceptualize the energy input; however, the value may be deceptive in terms of the actual welding schedule [31]. Frequency is the number of pulses per second in Hz, and the overlaps of welds can be controlled by coupling with a specific welding speed. Optimization of these parameters defines the process window for producing acceptable welds. However, the quality assurance of welds still involves some form of microstructural and mechanical analysis.

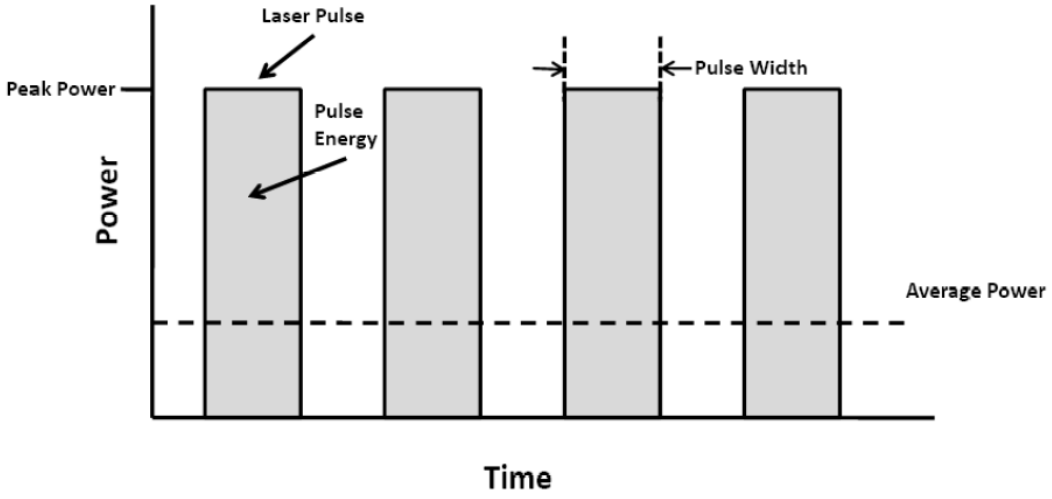

Figure 2.17: Schematic of laser pulses using Nd:YAG laser [31]

The advantage of laser welding is the ability to achieve high energy density thus producing maximum penetration of welds. This is achieved when the light is focused to a minimum beam waist diameter or focus spot size at the zero defocus distance (Figure 2.18) [27]. Offsetting from this distance will defocus the light, resulting in a decrease in power density. Focus spot size is specific to the combination of optics, laser characteristics, and welding parameters. A laser in its convergence range has the highest energy efficiency, and the focus position relative to the workpiece is dependent on welding mode (conduction or key-hole), geometry, and the use of filler metal [27]. The general rule is to focus at a distance where maximum penetration depth is attained through experimental verification.

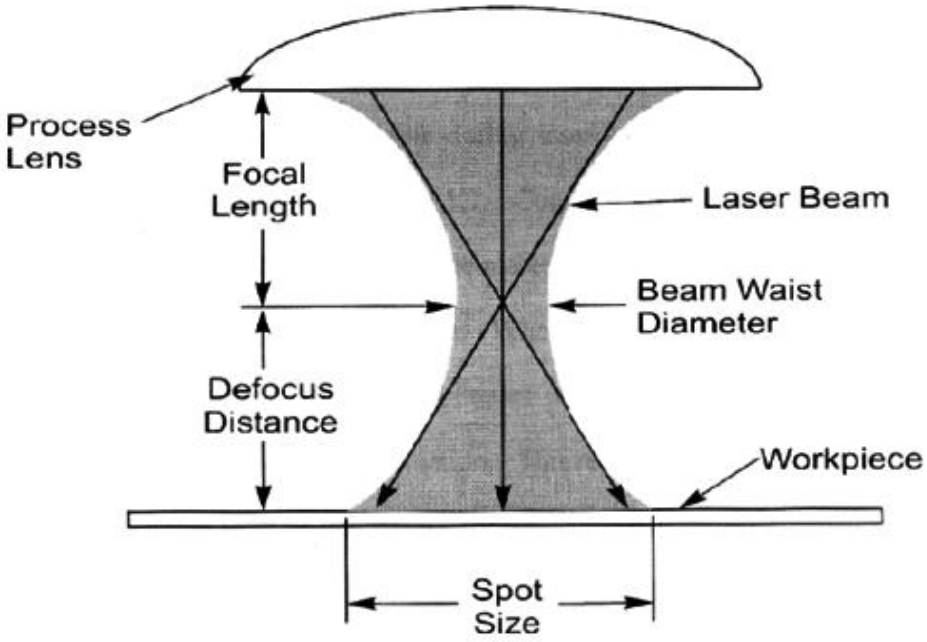

Figure 2.18: Schematic of propagation and convergence of laser beam [31]

Different energy densities can be achieved by the manipulation of lasing hardware (fibre optic, output coupling optics) and welding parameters (weld time, focusing distance). When combined with different welding times, the material may interact with the laser differently. Figure 2.19 shows the range of physical behavior expected to result as a function of power density and pulse duration [42]. Optimization of welding parameters is important to attain sound welds while preventing unattractive physical activities such as hole drilling, excessive surface vaporization, and creation of large heat affected zones [42].

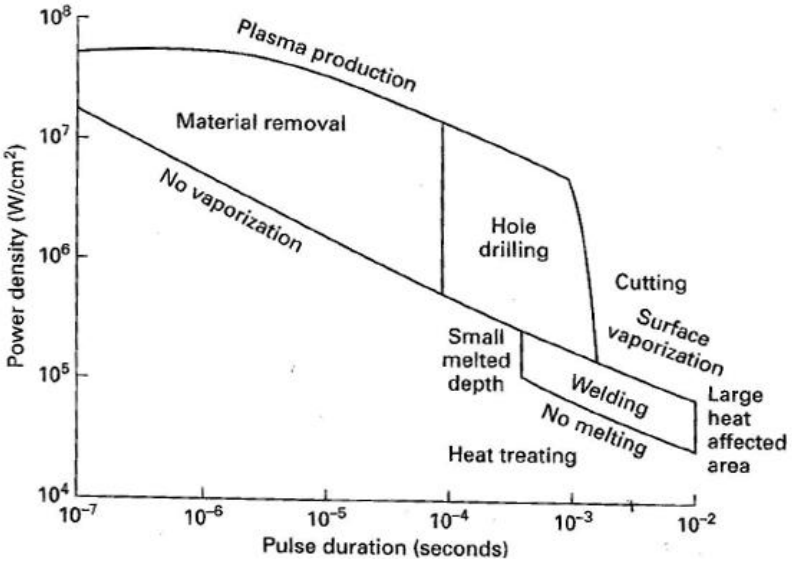

Figure 2.19: Laser-material interaction phenomena expected as a function of pulse duration and beam power density [42]

2.2.3 Shielding Gas

Inclusions in the weld metal microstructure are often detrimental to material properties [26-27]. Shielding gas of argon or helium is generally used to prevent reaction of atmospheric oxygen or nitrogen with the molten pool during welding. This is particularly important in the welding of Nitinol, because it has a high affinity for oxygen to form oxide. Proper selection of shielding gas also enhances the transmission of the incident laser beam for absorption by the workpiece [38].

2.2.4 Laser welding modes

There are two modes in which the incident laser beam is absorbed during laser welding, conduction and key-hole condition and they are shown in Figure 2.20 [26]. During conduction mode, surface materials are melted during the onset of laser interaction and the weld pool continuously grows radially due to heat conduction in all directions, creating a semi-elliptical weld pool of low aspect ratio [31]. By increasing the energy density, rapid removal of metal by vaporization creates a small keyhole. The entrapped ionized metal vapour enhances absorption of laser energy, producing much deeper welds.

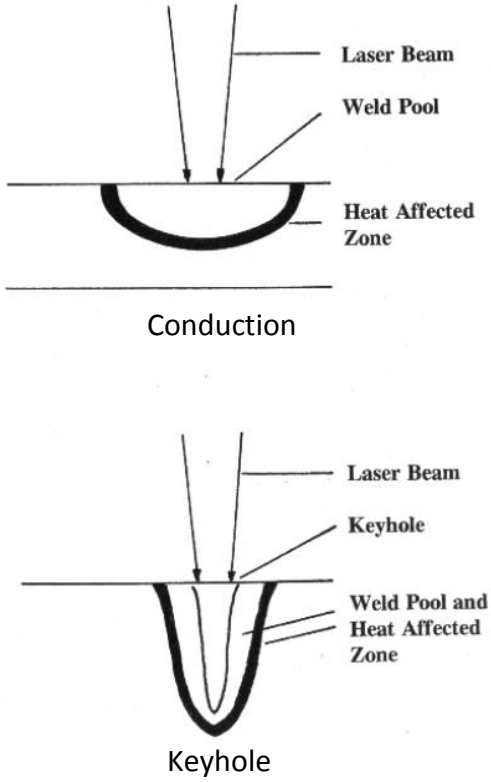

Figure 2.20: Comparison of conduction and keyhole welding modes [26]

2.3 Micro Resistance Spot Welding (MRSW) Fundamentals

Micro resistance spot welding is one form of a larger class of resistance welding that metallurgically bonds two faying surfaces using heat generated by the resistance to passage of electric current through the workpieces [42]. Similar to its large-scale counterpart, it involves the coordinated application of electric current and mechanical force of specified magnitude and duration [20]. During the RSW process two or more workpieces are clamped by two electrodes, establishing an electrical connection as shown in Figure 2.21. An AC or DC current is then supplied at low voltage for the generation of resistive heat to induce bonding, which could be solid-state or fusion [43].

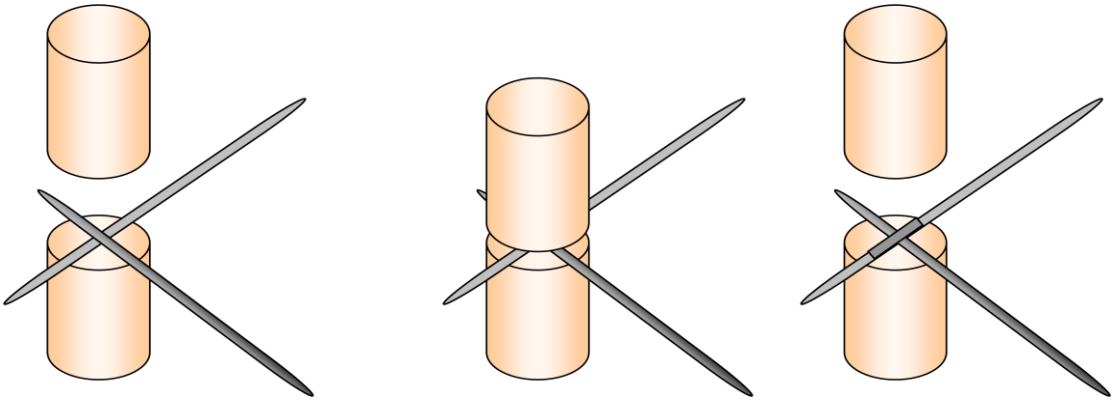

Figure 2.21: Schematic of MRSW process

The heat generation to induce bonding during resistance welding can be described using the following equation:

$$Q = I^2Rt \qquad (2.1)$$

Where *I* is welding current, and *t* is the duration of the current. Variable *R* is the total of resistances, which consists of contact resistances at the electrode/workpiece interfaces (*R1* and *R3*) and at the workpiece/workpiece interface (*R2*), and bulk resistances of workpieces (*R5* and *R6*) and electrodes (*R4* and *R7*), as shown in Figure 2.22. The heat generation is proportional to the square of the welding current and directly proportional to the resistance and welding time. Joining of workpieces occurs when sufficient heat is generated for melting (fusion) or diffusion of atoms (solid-state bonding) while accounting for heat lost due to atmospheric convection/ radiation and conduction to the thermal conductive electrodes [42]. Both welding current and welding time are process parameters while resistance is based on electrode force, material properties (resistivity, hardness, etc.), surface conditions (cleanliness, roughness, coating, etc.) and workpiece geometry (flat sheets, wires, etc.) [15, 20, 44]. The resistance values change dynamically during welding and their relative magnitude controls the process [42, 45]. The

contact resistance at the workpiece/workpiece interface is generally conditioned to be highest in relation to other resistance components, as that is of greatest interest for heat input for bonding [20]. This can be achieved by using electrodes made of high thermal and electrical conductive Cu-Cr-Zr alloy. As a result, heat can be conducted away quickly from the electrode/workpiece interfaces, minimizing melting and bonding between the workpieces and electrodes. However, very high contact resistance at the faying surface can result in severe explusion and therefore proper heat distribution between surface and bulk is required to attain good welds [45].

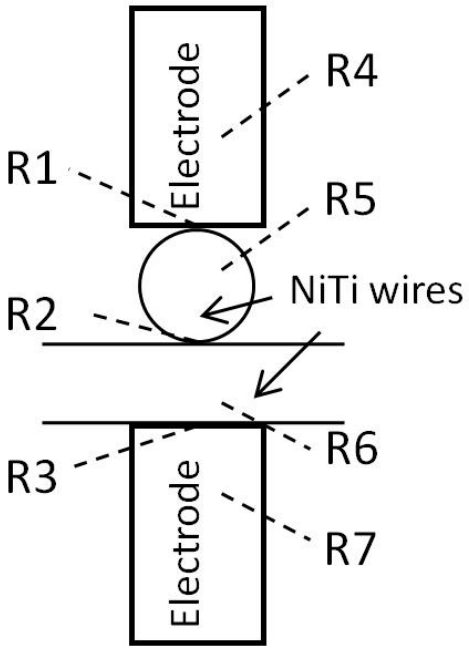

Figure 2.22: Resistances involved during MRSW

Although the principle of operation of MRSW is similar to its large-scale counterpart, one cannot simply transfer the metallurgical and operational knowledge between the two scales. Some of the major differences between the two processes are summarized in Table 2.1, which include scale of joints, magnitude of the welding parameters, materials, etc. Among them, the

differences in size and force of electrodes could be the most important factor that separates the two processes [42, 46]. Compared to large-scale resistance spot welding (LSRSW), a relatively small contact area is attained in MRSW due to the use of smaller electrodes and a much lower electrode force (Figure 2.23). This confines the area for current flow, creating a high-density energy source, which enables greater heating rate and higher peak temperature to be reached during welding. Also, due to the small scale of the electrodes, they are not equipped with internal water cooling that helps reduce electrode sticking.

Table 2.1: Comparison between the micro-scale RSW and large-scale RSW processes [20]

	Micro-scale RSW	**Large-scale RSW**
Sheet thickness	< 0.5 mm	> 0.5 mm
Electrode force	< 90-220 N	> 2200-4500 N
Electrode pressure $(\frac{Electrode\ \ force}{Tip\ area})$	< 30-60 MPa	> 120-240 MPa
Welding current	< 2-5 kA	> 5-10 kA
Electrode cooling	No	Yes
Materials	Mainly non-ferrous materials, such as Cu, Kovar, Ni, Ti, and silver (plated and bare)	Mainly steels, such as carbon steel and stainless steel (plated and bare), some Al alloys
Plating materials	Au, Ag, Ni, Sn, etc	Zn, Sn, etc
Typical application	Medical device and electronic components	Automotive body, electrical appliances

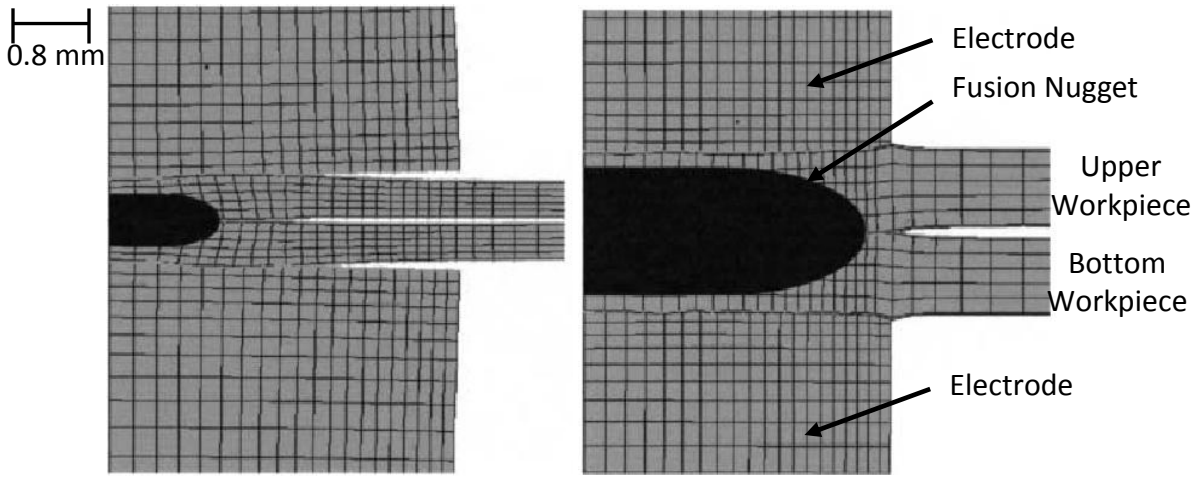

Figure 2.23: Model representation of contact area between (a) MRSW and (b) LSRSW [46]

2.3.1 Electrical Contact and Resistances

The electrical resistances that are responsible for heat generation during MRSW process were introduced in simple terms. However, the dynamics and factors that influence them can be quite complex in real physical situations [20]. In this section the Holm's contact theory will be described to better understand the relationship between contact resistance and heat generation [46, 49].

There are two main resistances responsible for heat generation: contact and bulk. The contact resistance can be further separated into two components, which are constriction resistance and film resistance. Therefore, the total resistance can be expressed as:

$$R = R_B + R_C + R_F \qquad (2.2)$$

Where R_B, R_C, and R_F are the bulk resistance, constriction resistance and film resistance, respectively [20, 44, 47].

Bulk resistance can be calculated using the following equation:

$$R_B = p\frac{l}{A} \qquad (2.3)$$

Where p is the resistivity of the material and l and A are the effective current path length and area [20, 44, 47].

For metals with clean surfaces (absence of oxide film), only constriction resistance needs to be considered. When two metal surfaces are brought in contact, the nominal contact area is different from the true contact area (Figure 2.24) [48]. Macroscopically smooth surfaces are rough microscopically: peaks and valleys, variation of inter-spacing, and geometrical differences all contribute to the roughness of the surface [48]. The true contact area could be as small as one to ten percent of the nominal contact area [45]. During the application of electrode force, contacting asperities collapse and point contacts become small areas of contact due to elastic and/or plastic deformation [44]. Simultaneously new contacts are also introduced at the interface [47-48]. The constriction resistance can be expressed in terms of the force (*F*), diameter (*D*) shown in Figure 2.24, modulus of elasticity (*E*), hardness (*H*), and electrical resistivity (*p*); as shown in Eq. 2.4 and Eq. 2.5 [42, 44].

$$R_C = \frac{0.57p}{\sqrt{n}}\left(\frac{E}{FD}\right)^{\frac{1}{3}} \quad : \quad Elastic\ Case \qquad (2.4)[42]$$

$$R_c = 0.89p\left(\frac{\xi H}{nF}\right)^{\frac{1}{2}} \quad : \quad Plastic\ Case \qquad (2.5)[42]$$

Where ξ is the pressure factor. Variable *n* is number of contact spots: polished, crossed cylinders have a value near 1, while overlapping, flat surfaces have values between 10 and 20. Plastic deformation is the predominant mechanism by which contact points are formed but in general, constriction resistance decreases with increasing applied force, which is illustrated in Figure 2.25 for various metals having a moderately flat and roughen surface (*n* = 10) [44-45].

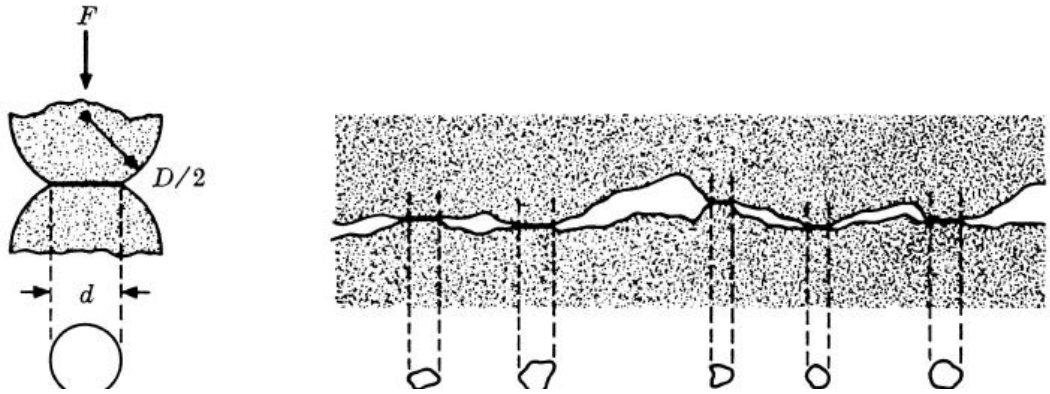

Figure 2.24: Single and multiple contact regions at an interface [44]

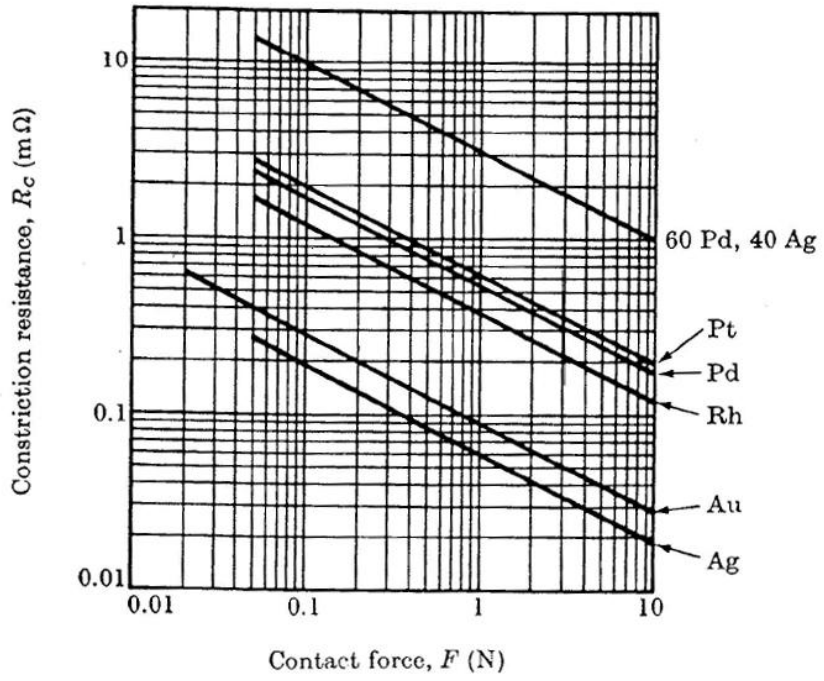

Figure 2.25: Contact resistance as a function of force for various materials [44]

Most metals have the tendency to form a non-conductive oxide film on the surface, which has very different electrical properties compared to the underlying base material. Excessive heat generated due to high electrical resistance of surface oxide films and contaminants may result in expulsion and/or electrode sticking. In practice, a mechanical or chemical cleaning treatment

is employed to remove them. However, great care is required when performing these cleaning operations as they can cause an increase in surface roughness and irregularity, which in turn lead to an increase in constriction resistance.

Initial contact resistance is considered the primary source of ohmic heating during resistance welding [40, 45]. As the peak temperature begin to rise, base material softens, which encourages progressive set-down and simultaneously lowering contact resistance (i.e. increase contact area due to the flattening of asperities) [42]. This is often observed in dynamic resistance measurements, where an initial peak resistance is observed before it diminishes to a negligible value after the first few welding cycles [16, 49]. Therefore, strict control on the surface conditions of materials is required in order to achieve consistent weld results, especially in MRSW where the surface area to volume ratio is much larger compared to LSRSW [42].

2.3.2 Joining Mechanism of Crossed-Wires

The special geometrical interaction in welding of crossed-wires can lead to different bonding behaviours when compared to traditional flat-sheet welding. For instance, bonding mechanisms were found to be different between a lap-joint of Ni films and crossed Ni wires. The former showed fusion welding and the latter underwent a solid-state bonding process [15, 20]. A point contact at the beginning ($n \cong 1$ in Eq. 2.4 and Eq. 2.5) in crossed-wire welding compared to flat sheet ($10 < n < 20$) can result in really high initial contact resistance, because of which balanced surface and bulk heating may not be attained for promoting fusion welding [45].

MRSW of crossed-wires of other materials has been previously examined in detail. Welds may be joined by solid-state, brazing, or fusion [15, 17-19]. The primary joining mechanism for Ni and 304 stainless steel (SS) wires was a solid-state bonding process with an initial transient liquid phase while Au coated Ni demonstrated a combination of brazing, solid-state bonding, and fusion welding [15, 17]. In contrast, for medical grade 316 SS the optimized bonding mechanism was fusion welding [19]. The bonding mechanism is strongly influenced by process

parameters (welding current, electrode force, etc.), material properties (resistivity, hardness, etc) and surface condition (oxide, roughness, etc.). For example, setting the electrode force too low can cause excessive interfacial heating and insufficient contact area for bonding while setting too high can result in cold welding [15]. Therefore, the condition for optimum bonding requires the balancing of welding parameters that generate the proper heat distribution along the workpieces.

Chapter 3: Experimental Method and Conditions

3.1 Material Selection

Commercially available 0.410 mm diameter pseudoelastic Nitinol wires (Memry Corp., USA) were used in this study. The material's nominal composition comprised 55.8wt% Ni with the balanced Ti. Complete chemical composition reported by manufacturer is detailed in Table 3.1. Previous thermomechanical processing had been performed on the wires by the manufacturer to optimize pseudoelasticity at room temperature. For the MRSW study, 316 low-carbon vacuum melted (LVM) stainless steel (SS) wires (Tegra Medical, USA) and 99% commercially pure nickel (Ni200) drawn wires of 0.380mm and 0.400 mm in diameter, respectively were also welded to themselves in the crossed-wire configuration in order to correlate the differences in resistivity and initial contact area between the workpieces to the joining mechanism.

Table 3.1: Chemical composition of Nitinol wires

Ni	Ti	C O Co Fe	Cr Cu	H	No
55.8	44.2	< 0.050	< 0.010	< 0.005	< 0.025

Nitinol's affinity to form a tenacious oxide layer may result in weld defects [59-61]. Hence, the as-received wires were immersed in a dilute solution of hydrofluoric acid and nitric acid to remove surface oxides and surface contaminants. Excessive immersion times could also reduce the cross-sectional diameter of wires. Figure 3.1 shows the percent reduction in diameter, which was linearly proportional to treatment time. As-received wires had a blackish appearance while treated wires had a more silvery colour to them. Backscattered electron (BSE) micrographs of the material before and after treatment are shown in Figure 3.2. Residual surface oxides remained visible at short treatment time. An immersion time of 20 s was

selected because of minimal residual oxides on the surface and a diameter reduction of less than 1 %.

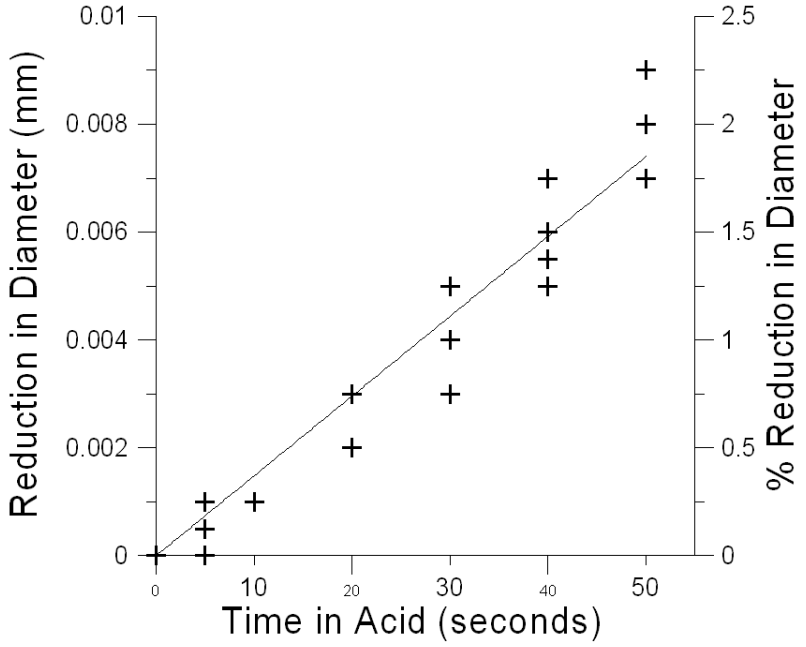

Figure 3.1: Effect of time in acid on percent reduction in diameter of Nitinol wire

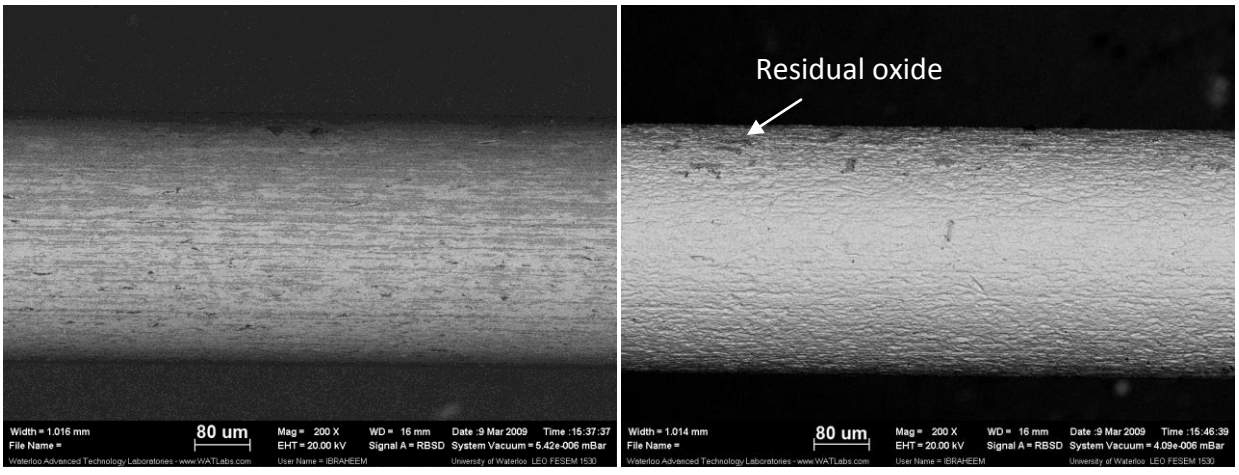

(a) (b)

Figure 3.2: SEM micrographs of wires (a) before and (b) after 20 s acid treatment

3.2 Resistance Spot Welding Equipment and Parameters

The MRSW system consisted of a MacGregor DC4000P DC power supply and a Miyachi 300 series Fast Response Weld Head coupled to a ±0.2 μm sensitivity Heidenhain displacement sensor, as shown in Figure 3.3. Cylindrical flat-ended class 2 Cu-Cr electrodes with a diameter of 3.2 mm were used. Wires were welded at right angles to each other, with the aid of a special fixture using variable currents from 120 A to 295 A. Weld time was 10 ms with an upslope and down slope time of 2 ms; a welding force of 5 kg-f was applied during the entire welding sequence (Figure 3.4). Short upslope and down slope times were chosen to enable fast heating and cooling.

Dynamic electrical signals (current, interfacial resistances, voltage drops) and displacement of the top electrode were monitored using a National Instruments Data Acquisition (DAQ) system. Interfacial resistances at the electrode-to-wire interfaces and wire-to-wire interface as *R1*, *R3*, and *R2*, respectively were analyzed (Figure 2.22). Displacement output (*B* in Figure 3.5) was converted to a percentage of embedment of the top wire into the bottom wire using Eq. 3.1, referred to as set-down. Plots of interfacial resistances and set-down were of averaged values from a minimum of 5 samples; the respective sample standard deviation, assuming Gaussian distribution was also plotted.

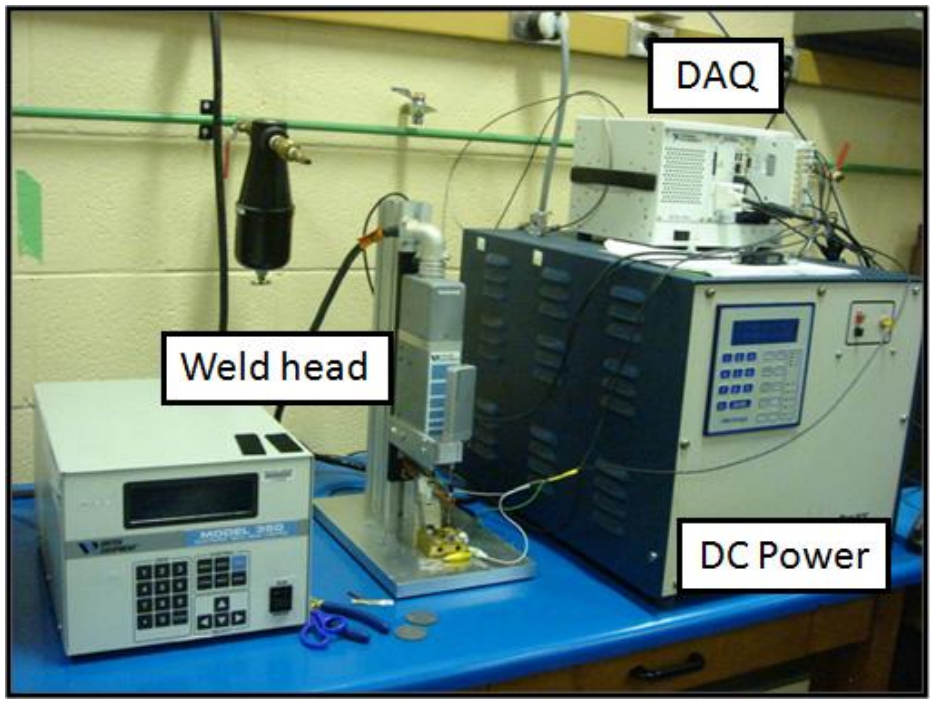

Figure 3.3: Micro-resistance spot welding machine setup

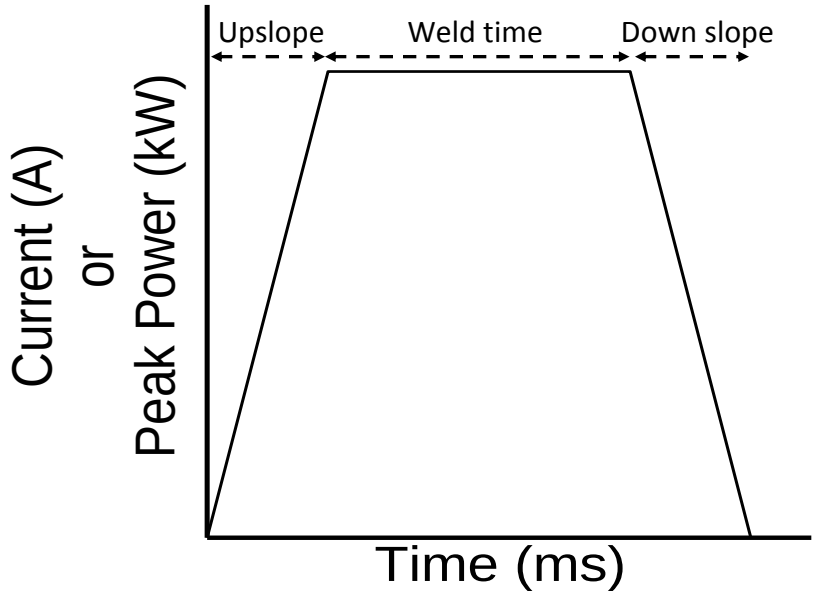

Figure 3.4: Schematic of welding schedule

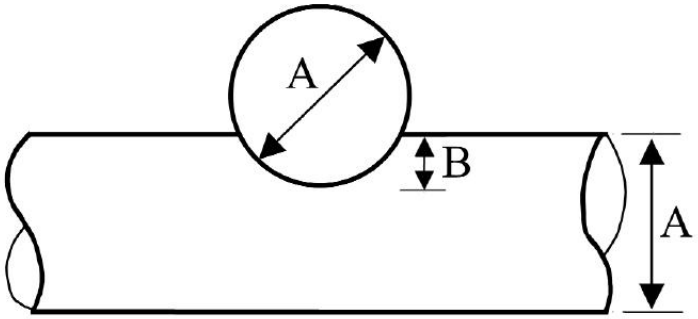

$$Set - down = \frac{B}{A}\ x\ 100 \qquad (3.1)$$

Figure 3.5: Schematic of set-down

3.3 Laser Welding Equipment and Parameters

Laser welding was performed using a Myachi Unitek pulsed Nd:YAG laser welder (Model LW50 A) that produces a laser beam with a wavelength of 1064 nm. The beam had a nominal spot diameter of 400 µm and a Gaussian power distribution. Peak power was varied between 0.55 kW and 1.75 kW. Welds were produced using a similar trapezoidal pulse schedule, which had a weld time of 5 ms and an upslope and down slope time of 1 ms. Argon shielding at a feed rate of 30 CFH was used to minimize oxidation during welding, in accordance with a previous study on titanium alloys [50]. The beam was focused centered at the intercept of the crossed wires using a positioning laser. A downward force was applied using a special fixture, which elastically deformed the wires onto a single plane, illustrated in Figure 3.7.

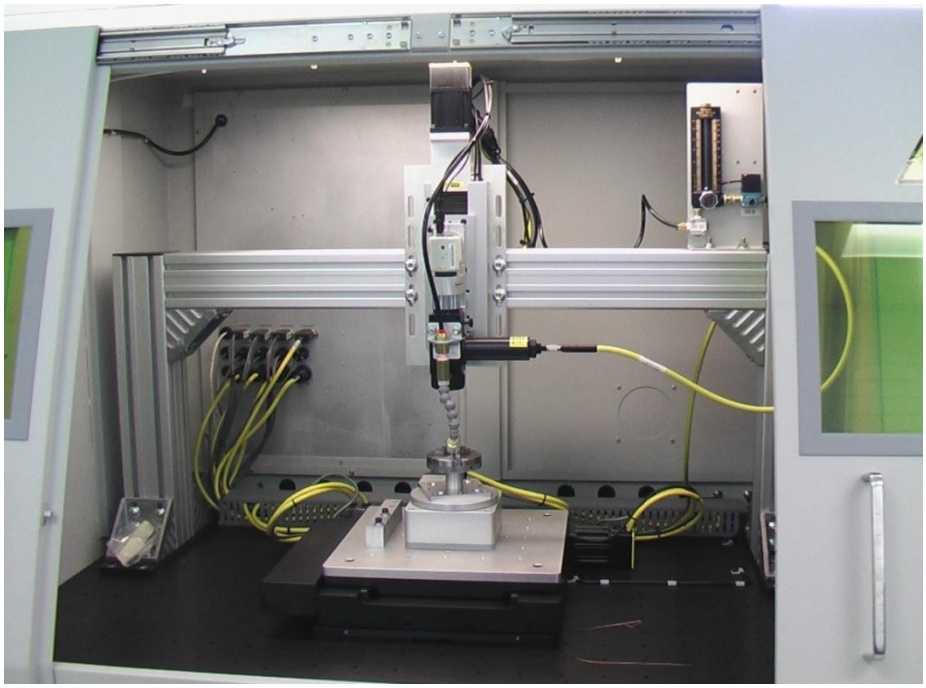

Figure 3.6: Laser micro-welding machine setup

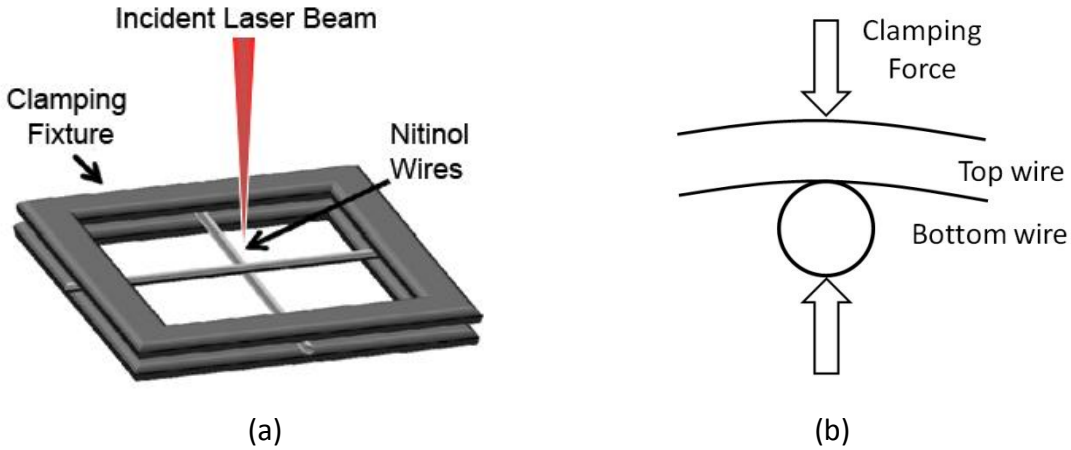

Figure 3.7: Schematic of (a) clamping fixture and (b) clamping force

3.4 Mechanical Testing and Microstructural Analysis

Joint performance of the crossed-wires was expressed as joint breaking force (JBF). Micro-tensile testing was conducted on an Instron 5548 micro-tensile tester at a crosshead speed of 0.4 mm/min. Tensile-shear test direction is indicated in Figure 3.8. A minimum of 7 samples were tested at each welding condition and the averaged values were taken with the highest and lowest values discarded. The dispersion of data was represented using sample standard deviation. Micro Vickers hardness was measured using a Shimadzu micro hardness tester. A series of 50 g indents, 40 µm apart, held for 20 s were made on the longitudinal centerline of the welds. The line of indents was defined to cover ample distance of base material beyond the weld area and HAZ. Hardness values were evaluated using the ImagePro software.

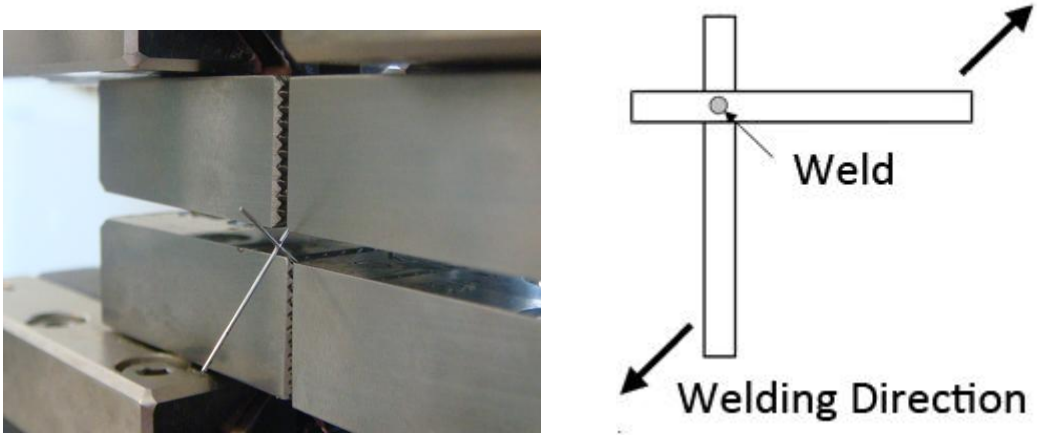

Figure 3.8: Tensile test direction

Weld cross-sections and fracture surfaces were examined using an Olympus optical microscope and a Jeol JSM 6460 scanning electron microscope. Surface topology was scanned and measured with a WYKO NT1100 Optical Profiler. Metallographic profiles were prepared by first cold mounting the samples in epoxy. For SEM analysis, samples were hot mounted in conductive resin. The samples were then ground from 120 grit to 1200 grit using sand papers and followed by a 2 step polish using 2 µm diamond and colloidal silica. Finally, the samples

were etched with 14 mL HNO_3, 3 mL HF and 82 mL H_2O solution for 25 s to 30 s to reveal the microstructure.

3.5 Phase Analysis

Phase transformation temperatures were measured by DSC using a Thermal Analysis Q2000 system equipped with a refrigerated cooling system (RCS). Tests were conducted between -75 ^{o}C and 100 ^{o}C, controlled at rate of 5 ^{o}C per minute. Onset temperatures of phase transformations, M_s and A_f, were determined as the intersection of tangent to the slope of maximum inclination of the appropriate peak with the base line, illustrated in Figure 3.9. Welded samples were carefully sheared off from the base metal material; however, due to the small scale some remnant base metal material remained on the DSC samples. Base metal, quenched in water from 1 hour of heating at 800 ^{o}C to attain solid-solution condition, was also tested to observe the intrinsic phase transformation behaviour. The measurements of as-received and annealed base metal are summarized in Table 3.2.

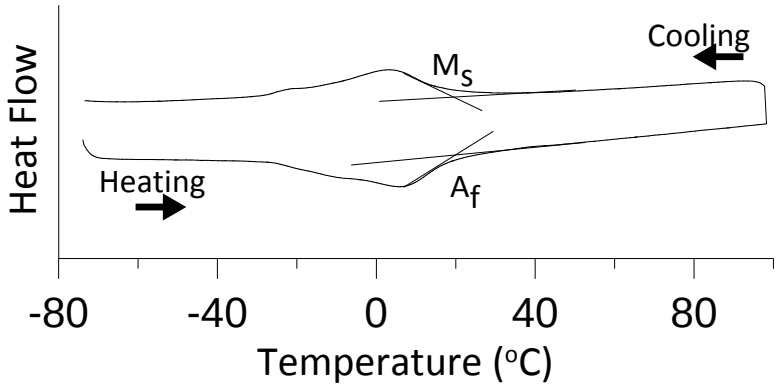

Figure 3.9: DSC curve of as-received material

Table 3.2: Phase transformation temperatures of as-received and annealed base metal material

	M_s (°C)	A_f (°C)
As-Received	19.14	19.65
Annealed	-28.66	-7.59

XRD analysis to determine the crystal structure of weld metal was conducted on a Rigaku micro-XRD that utilizes a 1.54 angstrom wavelength Cu k-alpha x-rays. A 0.3 mm collimator was used to focus at the weld cross section of metallographic samples. Data was processed using the JADE software that accompanied the XRD equipment.

Chapter 4: Micro-Resistance Spot Welding of Crossed NiTi Wires

4.1 Effects of Surface Oxides

Figure 4.1 shows the resistance profiles of welds using acid treated and untreated wires. Dynamic resistance was characterized by an initial peak resistance followed by a sharp decrease occurring within the first few milliseconds of heating. Subsequently, the resistance value gradually diminished to a relatively low value until the weld was completed, similar to literature [16]. Acid treated wires exhibited reduction in peak resistances at all interfaces (*R1*, *R2*, and *R3* in Figure 2.22), which can be attributed to smaller film resistance associated with the surface oxide and contaminants. The reduction in resistance allowed the use of higher currents before severe expulsion of the joint and/or sticking between electrode and joint occurred. Prolonged acid treatment duration did not further improve the relative peak resistance values, as shown in Figure 4.2. What was important was the larger value of *R2* relative to those of *R1* and *R3*, which, in accordance with Eq. 2.1, enabled greater resistive heat generation at the wire-to-wire interface for metallurgical bonding. Moreover, cleaning also prevents contaminants embedding in the microstructure during welding as they can significantly degrade joint quality and strength [51].

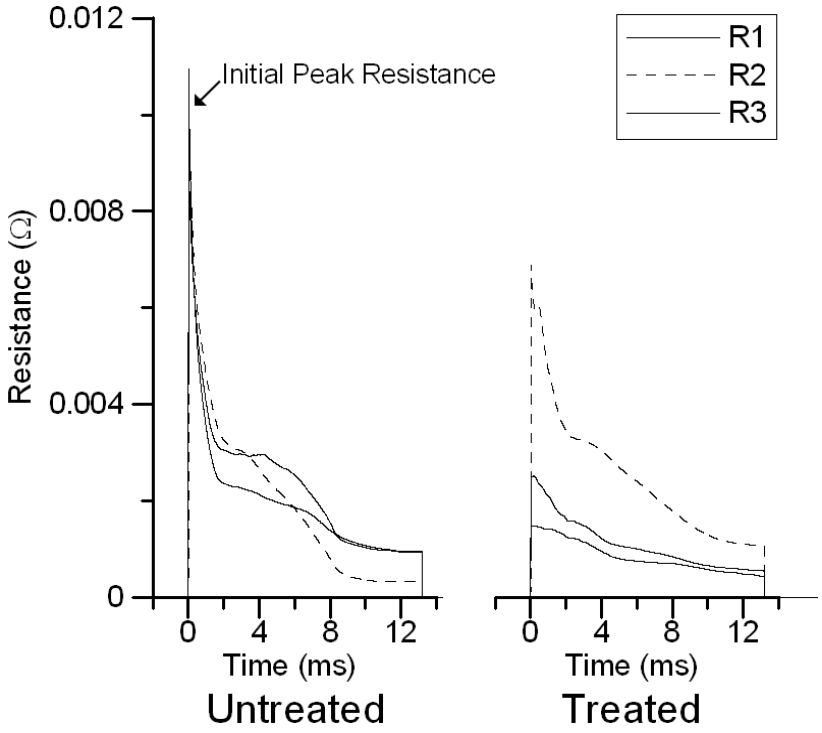

Figure 4.1: Effects of acid treatment on interfacial resistances

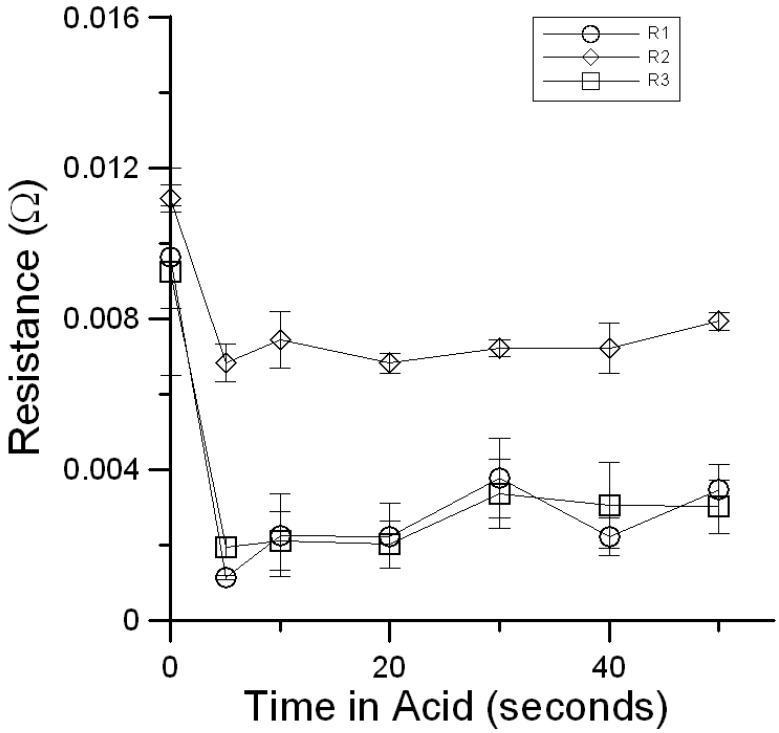

Figure 4.2: Interfacial peak resistances as a function of immersion time in acid

4.2 Microstructure of Cross-Wire Joints

Figure 4.3 shows the cross-sectional profiles of welds made between 145 A and 295 A. Heat generated near the interface during the initial application of current resulted in recrystallization of the original fine grained base metal structure, shown in Figure 4.3a (HAZ outlined using dashed lines). The bond interface was clearly visible at 145 A but was not present prior to etching, which suggested insufficient bonding likely due to entrapment of surface defects and contaminants (Figure 4.3b) [42]. Both base and weld metals showed a number of fine dispersed precipitates in the microstructure, which could be TiC compounds formed during the production of Nitinol ingot [52].

Increasing welding current to 195 A resulted in widening of the HAZ (Figure 4.3c). Weld microstructure exhibited grain growth at the faying surface, suggested by the partial disappearance of the bond interface (Figure 4.3d). Squeezed out metal and surface contaminants, commonly referred to as flash material was observed around the joint periphery. This was facilitated by the combination of initial high resistance heating at the faying surface and electrode force, which melts the surface material and pushes the molten material towards the joint periphery [42]. Figure 4.4 shows this partially molten flash material. Weld microstructure at currents up to 245 A experienced further widening of the HAZ and complete elimination of the bond interface while more flash material was expelled (Figure 4.3e and Figure 4.3f). Complete set-down was attained at 295A with columnar grains forming at the top and bottom surfaces due to surface melting (Figure 4.3g and Figure 4.3h). Finally, severe expulsion occurred when more than 295A of current was applied, resulting in no joint formation.

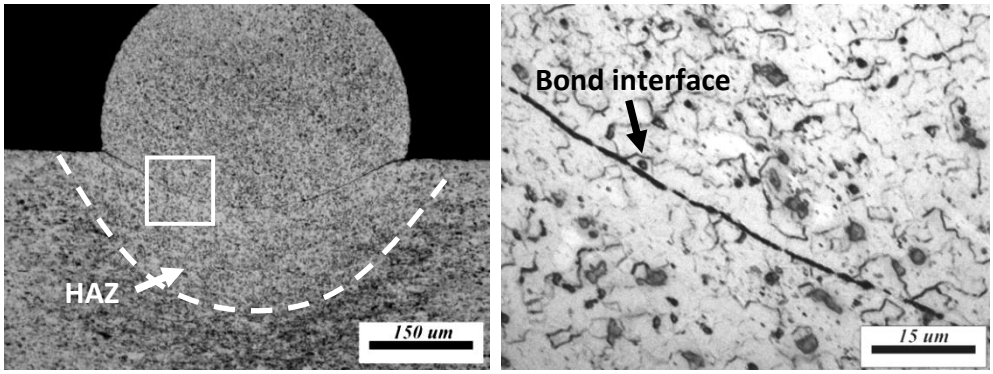

(a) 145 A (b) 145 A (100x)

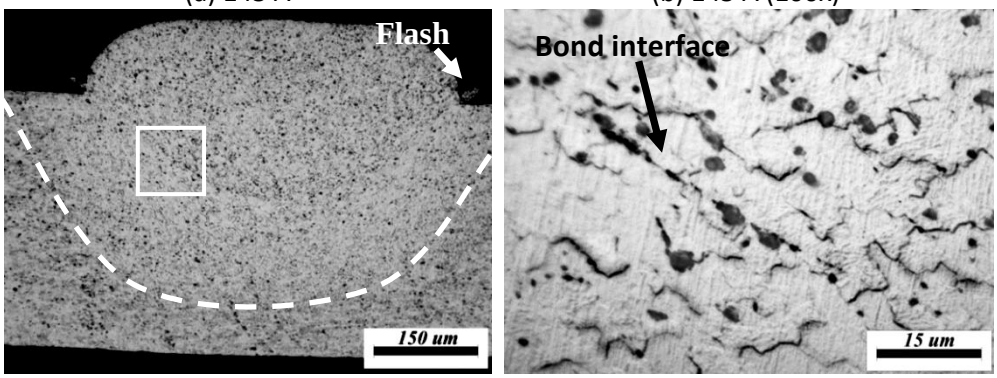

(c) 195 A (d) 195 A (100x)

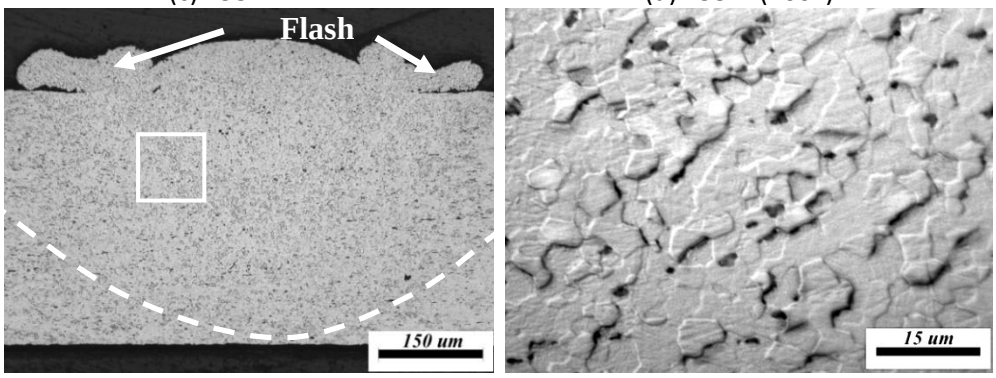

(f) 245 A (e) 245 A (100x)

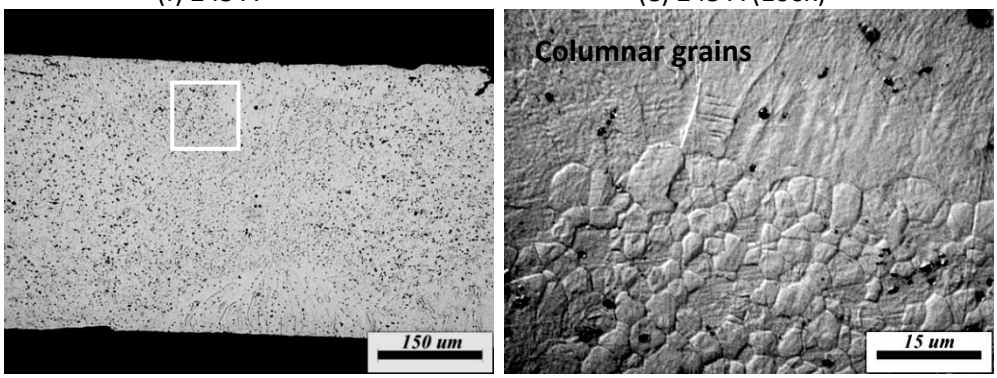

(g) 295 A (h) 295 A (100x)

Figure 4.3: Cross sections of joints welded at different welding currents

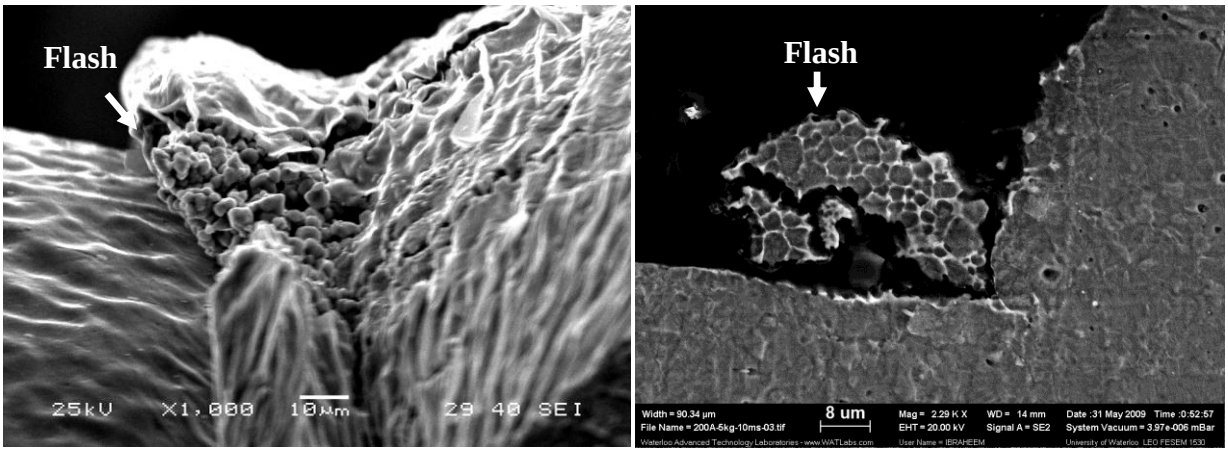

(a) (b)

Figure 4.4: (a) Outer and (b) cross-sectional views of the flash material

Hardness along the longitudinal centerline of welds prepared at select currents was measured and is shown in Figure 4.5. Base metal hardness was approximately 400 Hv, resulting from the fine grained structure produced during the cold-drawing fabrication process. Hardness values decreased 30-35% (softening) approaching the welds with the highest current welds showing the largest decrease. Softening in the welded region was more pronounced near the bond interface where the highest electrical resistance was measured (Figure 4.2).

The primary joining mechanism for MRSW of crossed Nitinol wires was solid state, similar to previous studies on Ni and 304 SS crossed-wires [15, 18]. The joining process can be described in 6 main stages, schematically shown in Figure 4.6. The initial stage 1 “cold collapse” describes the mechanical deformation imposed by the electrode force, from which a larger contact area was formed. Subsequent application of welding current increased the temperature at the interface, resulting in “dynamic recrystallization” (stage 2) of the fine grained base metal microstructure and softening in the HAZ. As peak temperatures surpassed the solidus temperature at the interface, “interfacial melting” (stage 3) occurred, followed by stage 4 “squeeze out” where the electrode force pushed the partially molten metal toward the weld perimeter. This stage is necessary for good solid state bonding as contaminants are removed from the junction, improving surface conditions for crystallographic matching and interdiffusion of atoms across the interface [15]. A large amount of expulsion was detected with increasing

welding currents, also referred to as stage 5 “excessive flash”, which introduced undesired defects in the weld metal. Further increase in currents induced melting of the wire surfaces (stage 6 “surface melting”) and sticking of welds to the electrodes, which can significantly affect weld quality and shorten electrode life [51].

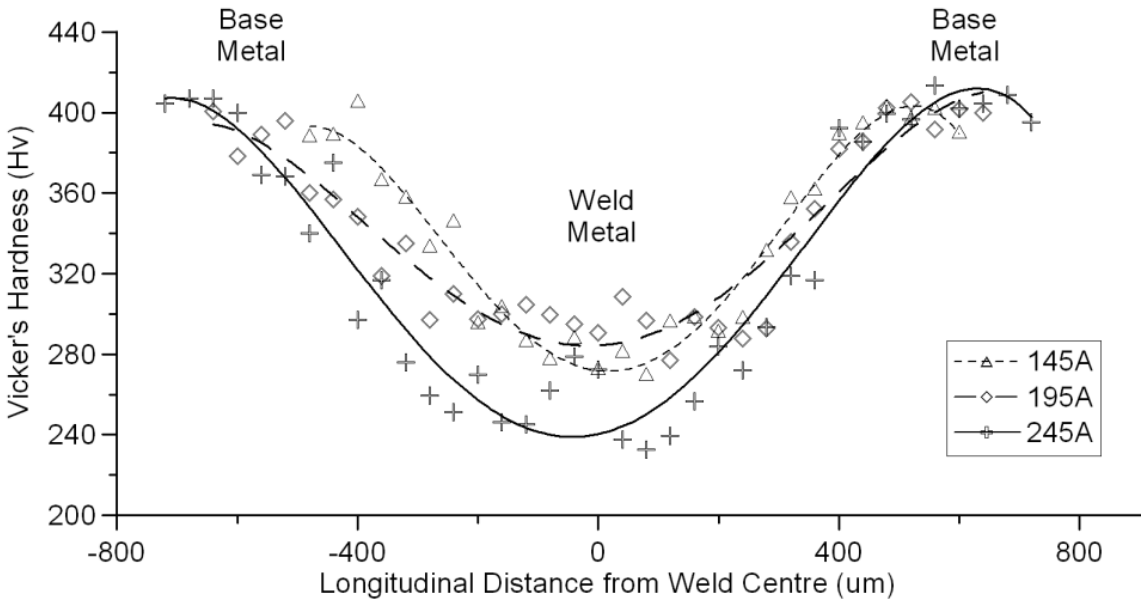

Figure 4.5: Hardness traces along cross-section of welds made using 145 A, 195 A and 245 A

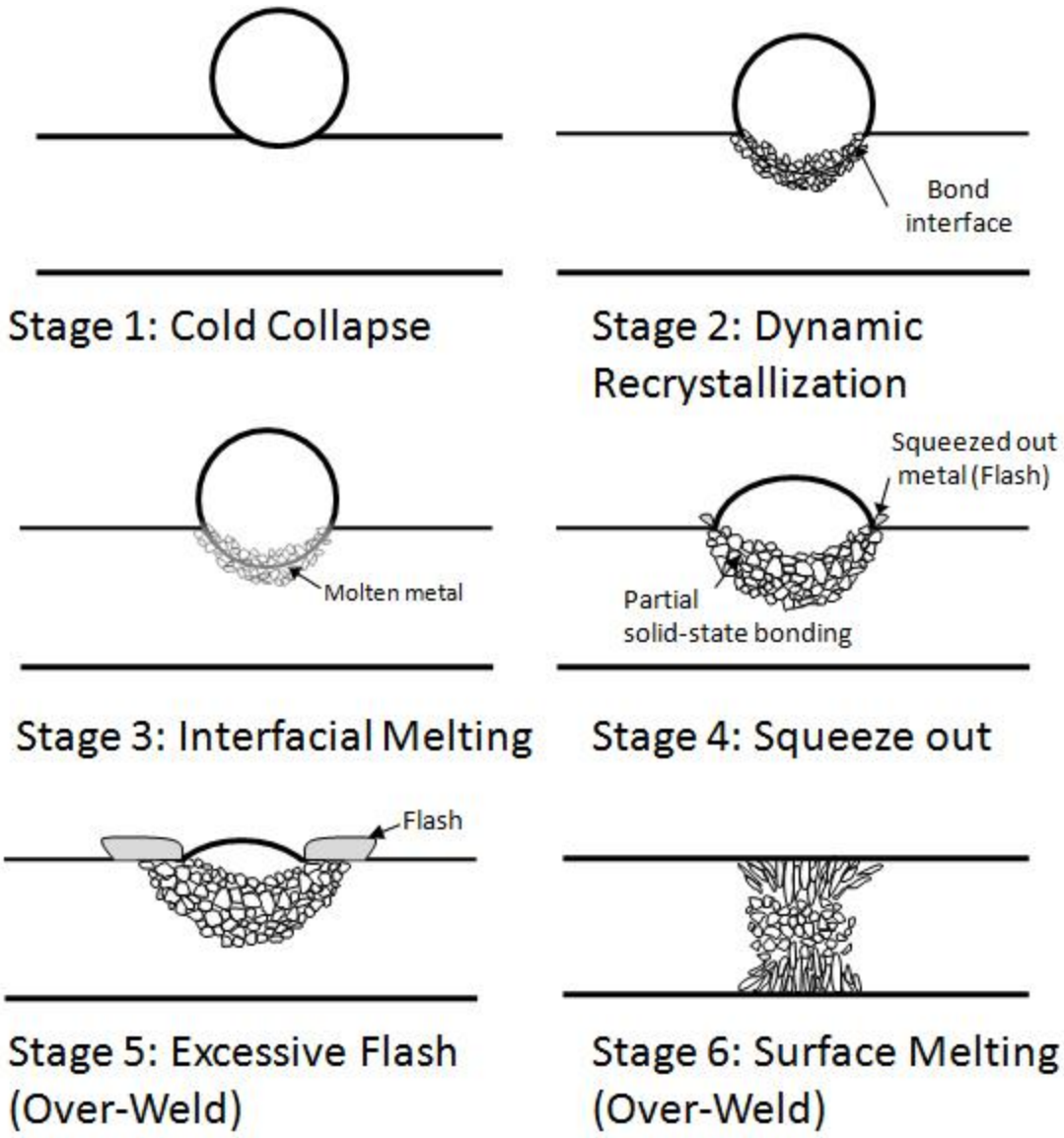

Figure 4.6: Main stages of the bonding mechanism of MRSW of crossed NiTi wires.

4.3 Mechanical Properties and Joint Breaking Force

The effects of welding current on set-down and JBF are shown in Figure 4.7. Set-down increased gradually with current and complete set-down was attained at 295A. A minimum welding current of 115 A was required to initiate bonding with JBFs increasing slightly up to 145 A. Joint strength improved sharply near 165A followed by a more gradual increase up to 195 A, where the maximum JBF of 18 N was attained at 70 % set-down. Further increase in

current resulted in overwelding and degradation to joint strength due to the introduction of weld defects.

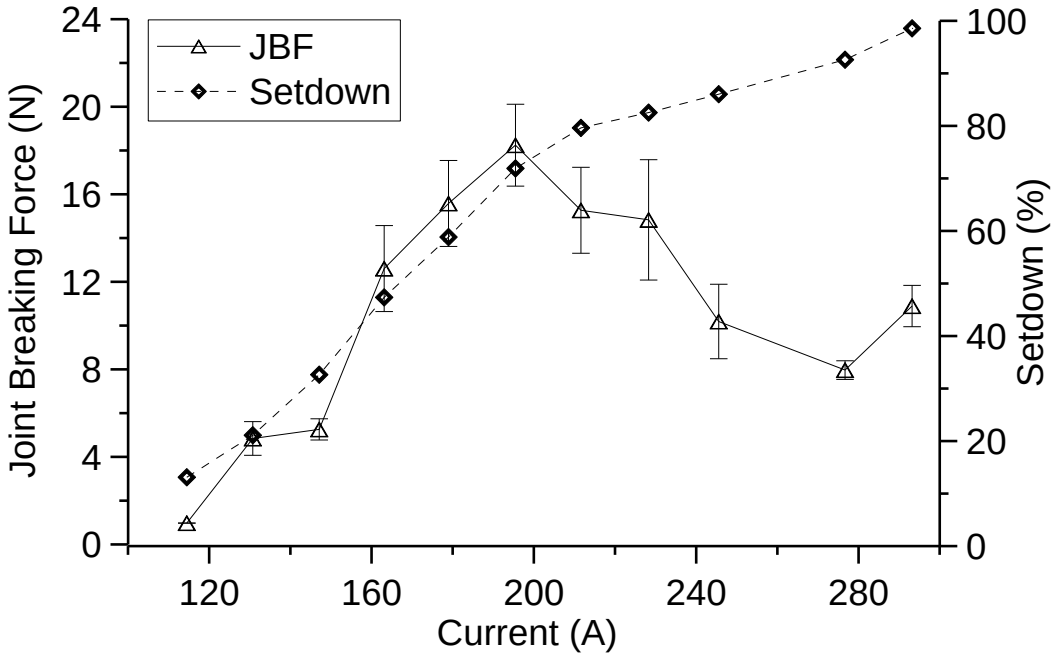

Figure 4.7: Effects of welding current on joint breaking force and set-down.

SEM micrographs of fractured samples welded between 145 A and 245 A are presented in Figure 4.8, which showed joints failed at the welded region for all currents tested. Joint strength and fracture mechanism of MRSW of crossed NiTi were strongly influenced by the weld morphology. Between 115 A and 145 A, at which low JBFs were attained, fracture occurred through the bond interface (Figure 4.8a). The relatively smooth fracture surface indicated a sudden brittle fracture mode (Figure 4.8b). By increasing the welding currents to 195 A and 245 A, joint strength gradually increased due to improved bond strength as set-down increased coupled with solid state bonding. This was reflected by the dimpled ductile fracture morphology (Figure 4.8d). However in the 195 A fracture surface, regions of the bond interface were visible (Figure 4.8e). At intermediate currents discontinuities along the bond interface (Figure 4.9) acted as stress raisers resulting in fracture initiation at the interface (Figure 4.8e), which then propagated through the softened HAZ. At higher currents, the HAZ became the preferred region for fracture as the bond strength continued to improve while the

HAZ was further softened due to recrystallization. Additionally, a sizeable separation at the edge was formed due to the increased flash material, creating a notch effect. Figure 4.10 shows a SEM micrograph of a failed joint halted at the onset of failure during a tensile test with the fracture path indicated by the arrow. Stress concentrated at the edge under loading, allowing fracture to easily penetrate into the HAZ, reducing the joint strength substantially.

Transition of fracture modes from interfacial at low currents (115 A to 145 A) to HAZ at high currents (210 A to 295 A) is schematically shown in Figure 4.11. Mixed mode failure occurred when using intermediate currents (165 A to195 A), also referred to as partial-interfacial. Increasing welding current creates a competition between two counter-balancing behaviours, increased interfacial bond strength and wire softening, which improve and degrade joint strength, respectively. The sum of their effect determines the actual joint strength. At low current, insufficient bonding led to interfacial failure while at high current, joints failed through the softer HAZ. Maximum JBFs were obtained at intermediate welding currents when bond strength and wire softening were balanced.

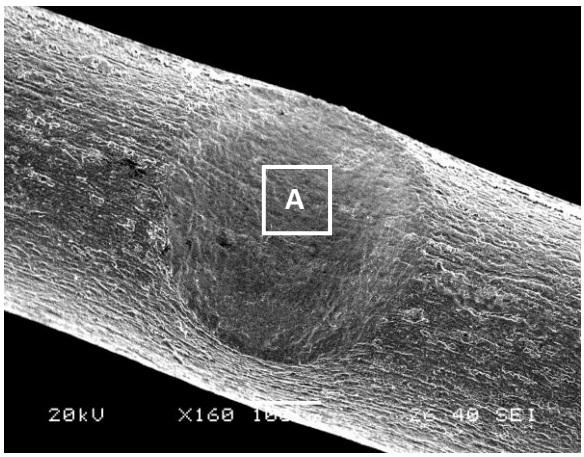

(a) 145 A

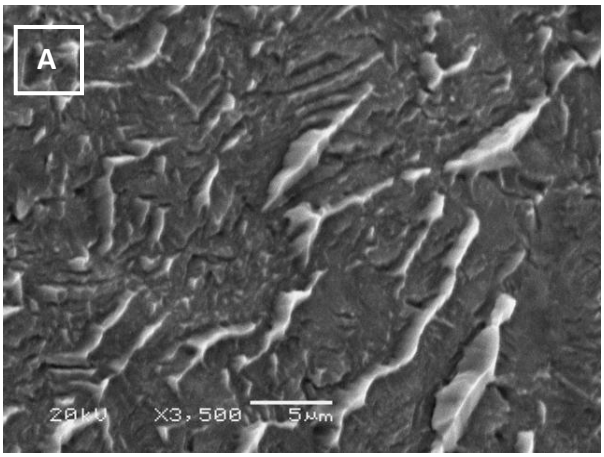

(b) 145 A (area A)

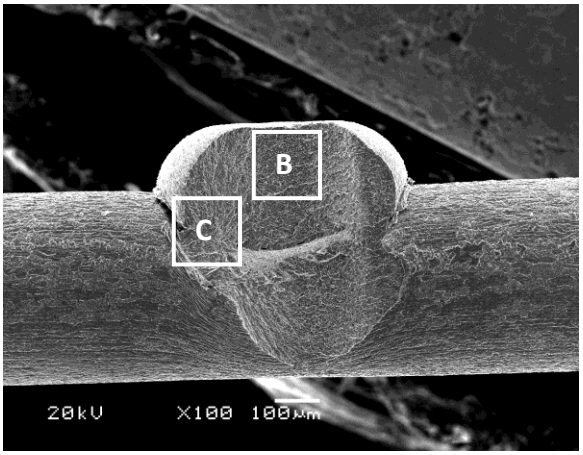

(c) 195 A

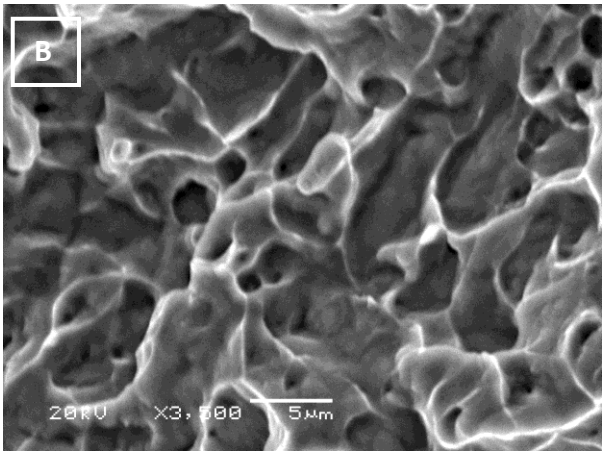

(d) 195 A (area B)

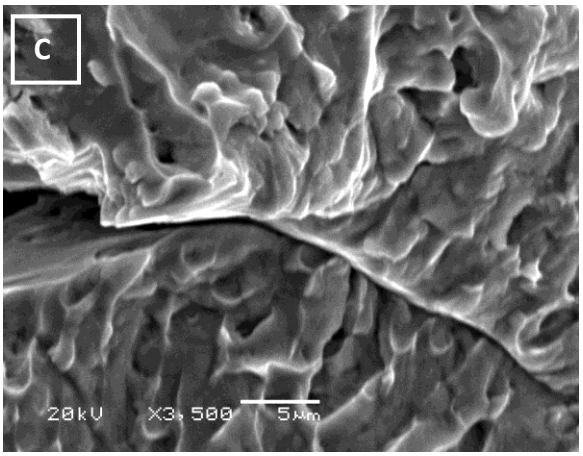

(e) 195 A (area C)

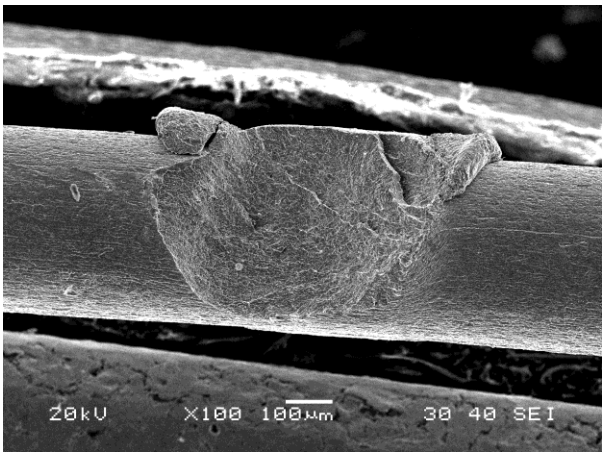

(f) 245 A

Figure 4.8: Fracture surfaces of joint welded at different welding currents

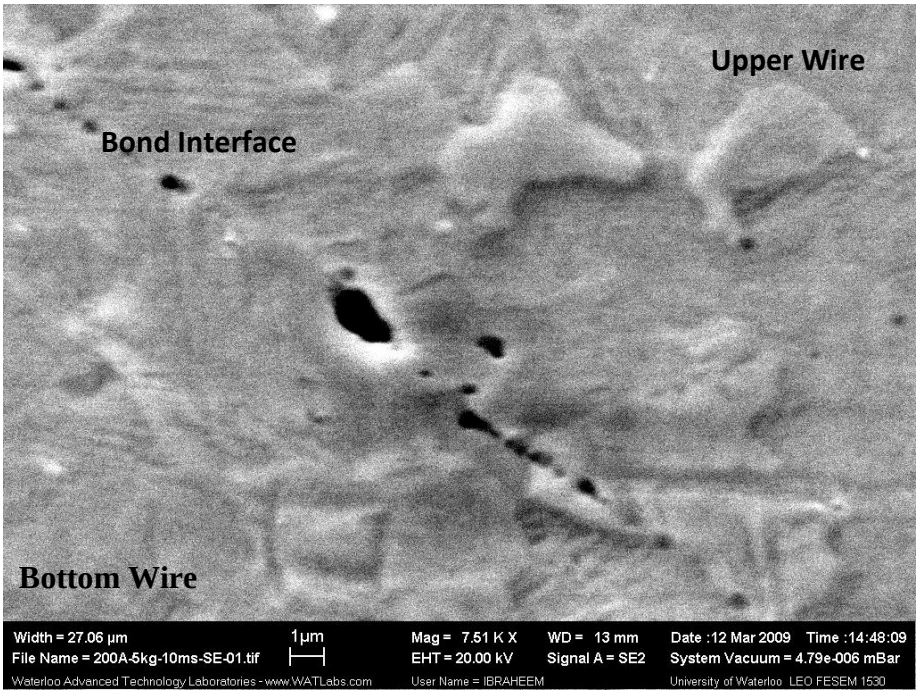

Figure 4.9: Bond interface of joint made at 195 A

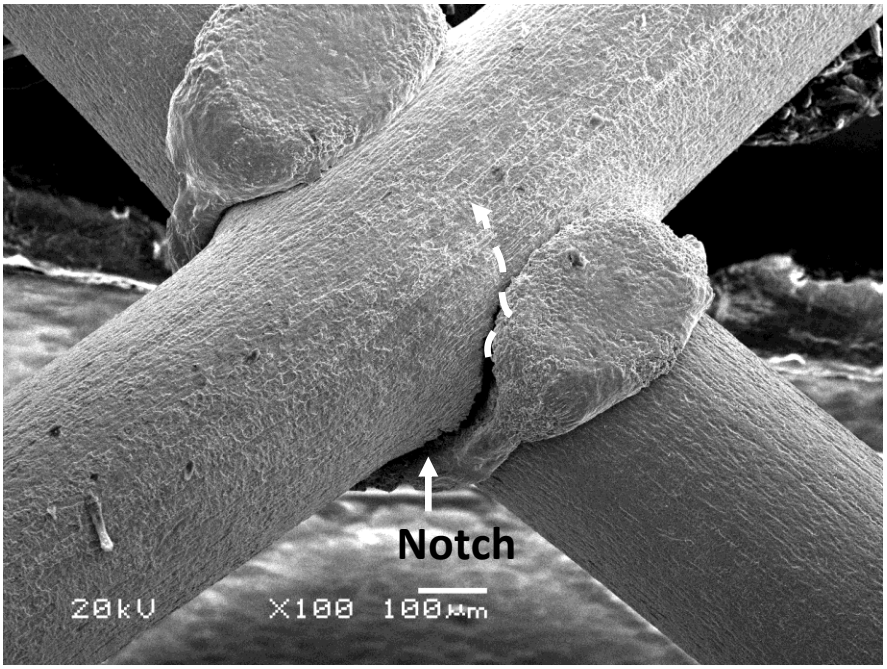

Figure 4.10: Partial failure of weld made at 245 A

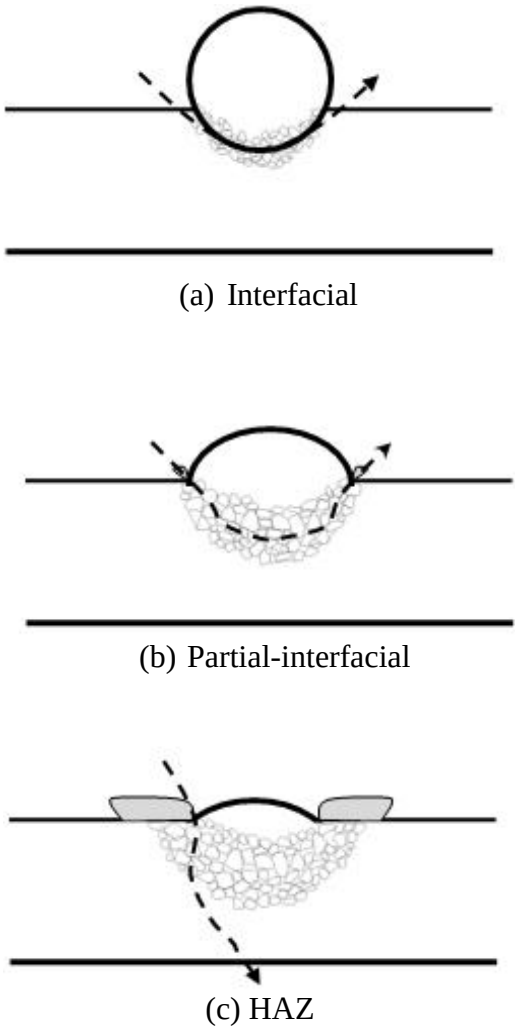

Figure 4.11: Schematic of failure modes transitioning

4.4 Phase Transformation

DSC curves for as-received, heat treated base materials, and welds produced at select weld currents are shown in Figure 4.12 with transformation temperatures (A_f and M_s) of weld summarized in Table 4.1. As-received and heat treated base metals are provided in Table 3.2. The weld metal experienced multiple transformations, including two pairs of high temperature peaks and low temperature peaks. Residual base metal on the tested specimens can account for the high temperature peaks, which had similar transformation temperatures to as-received

material. On the other hand, weld metal transformed at lower temperatures. Increasing welding currents showed little effect on the weld transformation temperatures.
The MRSW process modified weld metal to transform at lower temperatures, similar to annealing base metal at 800 ^{o}C. This phenomenon was experimentally verified by examining welds produced with fully annealed wires at a welding current of 195 A (Figure 4.13). The DSC sample underwent single phase transformation at temperatures similar to annealed base metal, suggesting near homogeneous microstructure. However, the temperature range where transformation occurred was wider, likely due to the mechanical strain imposed by the electrodes.

The intrinsic phase transformation behaviour of Nitinol is strongly influenced by thermomechanical processing. This alloy is known to exhibit broad temperature peaks when mechanically strained and narrow when fully annealed to its intrinsic state [21-22, 35-36]. Cold working can also result in higher transformation temperatures, because higher activation energy is required to overcome the internal stress induced by random dislocations [22, 35-36]. The base metal was previously cold rolled and aged, which explained the acquired transformation temperatures. During welding, the high temperature workpieces experienced resetting of the effects of previous thermomechanical processing and returned the material to near fully annealed state. Higher degree of base metal annealing occurred at higher welding current, which resulted in more defined temperature peaks. This correlated with the widening of the HAZ when welding current was increased. Moreover, transformation temperatures of weld metal were relatively constant at different welding currents, suggesting peak temperatures during welding were at or above solution-treatment temperature of 600 ^{o}C [33, 53].

The current results showed that welding significantly impacts the phase transformation behaviour of Nitinol. Resistance heating from the MRSW process anneals the original base metal, producing a HAZ that mimics solid-state solution treatment. These local modifications in

the weld zones can adversely affect the functional properties of Nitinol and need to be considered in applications where resistance micro-welding is implemented.

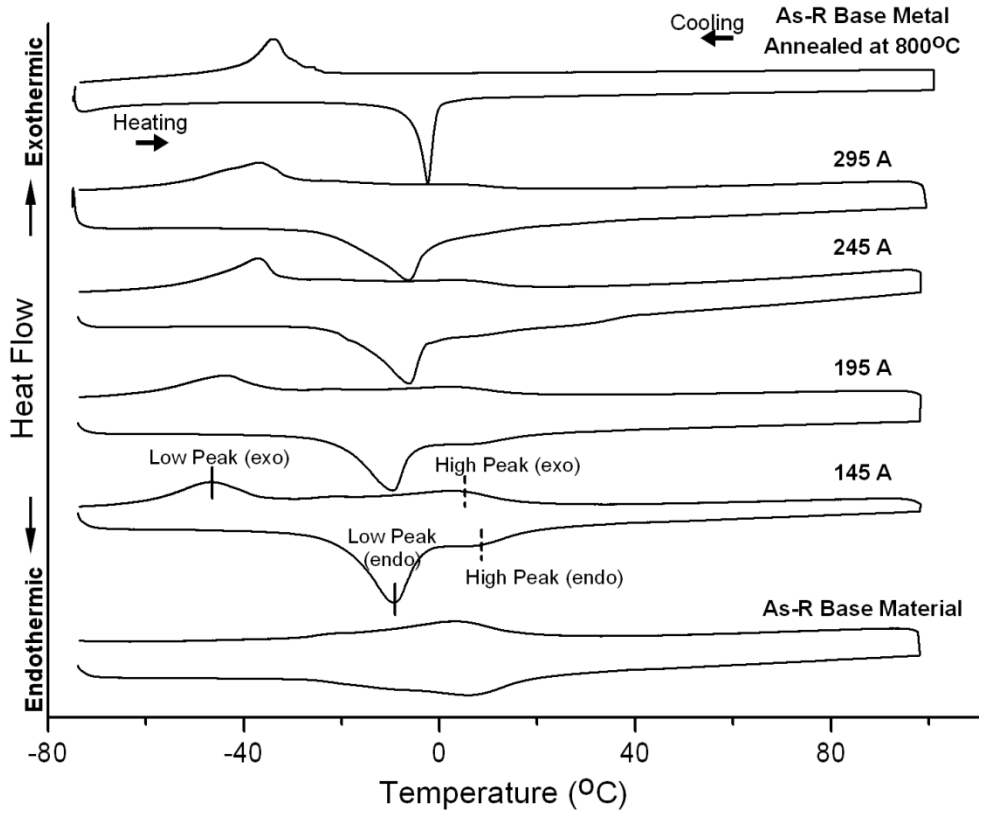

Figure 4.12: DSC heating and cooling curves of annealed wire, as-received wire, and weld made using various currents

Table 4.1: Transformation temperatures of weld made using 160 A, 195 A, and 245 A

	HAZ		Fusion Zone	
	M_s (°C)	A_f (°C)	M_s (°C)	A_f (°C)
145 A	-36.26	-3.88	18.05	19.50
195 A	-36.48	-5.84	17.06	18.75
245 A	-36.26	-2.26	14.50	n/a

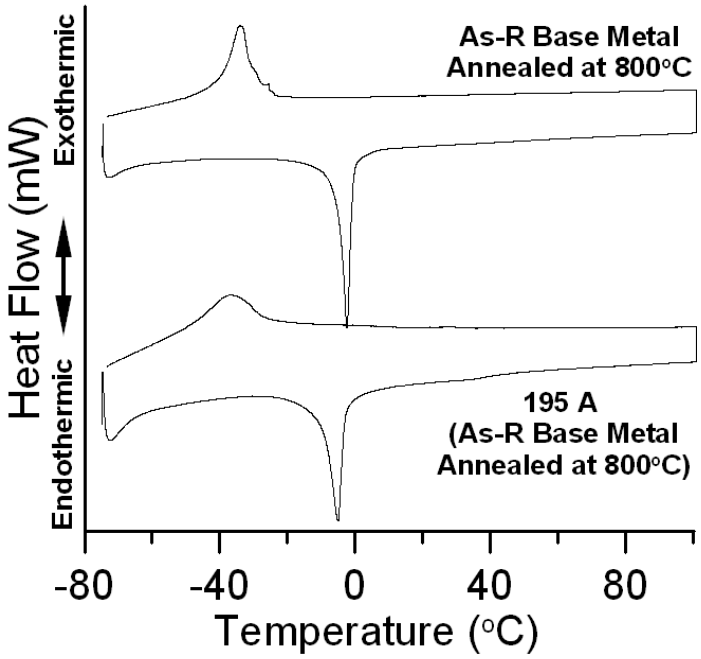

Figure 4.13: DSC heating and cooling curves of annealed wire and weld made at 195 A using annealed wire

4.5 Effects of Pseudoelasticity on Contact Resistance

The peak temperature reached and the type of joining mechanism to occur during MRSW depends on the amount of resistive heat generation. It has been shown that the primary ohmic heating for bonding is produced by the initial contact resistance, which can be divided into constriction resistance and film resistance [44, 49]. Figure 4.14 shows the *R2* interfacial resistance during MRSW of Nitinol, Ni, and 316 SS crossed-wires. The initial peak resistances suggested that for the same welding schedule (*I* = 200 A) the generation of heat or peak temperature reached was highest for 316 SS, then Nitinol and finally nickel, matching literature as the primary joining mechanism for 316 SS and Ni was fusion and solid-state, respectively [15, 19]. Fusion welding occurs when peak temperature surpasses the liquidius temperature (Nitinol, Ni, and 316 SS have similar melting points as listed in Table 4.2). Similarly, the current study showed solid-state bonding in MRSW of Nitinol wires.

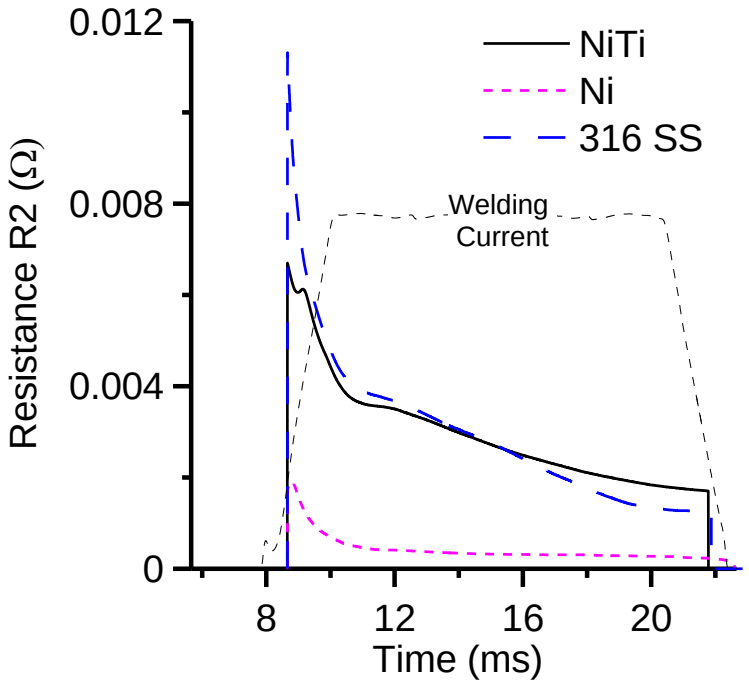

Figure 4.14: Interfacial resistance *R2* for MRSW of crossed-wires of NiTi, Ni, and 316 SS (*I* = 200 A)

The interfacial resistances are strongly influenced by several factors. Holm's contact theory that was detailed in Sect. 2.2.1 basically states that the electrical resistivity and the total contact area dictate the constriction resistance (Eq. 2.4 and Eq. 2.5). The theory is based on metal that deforms elastically and plastically, and therefore, Nitinol and other shape memory alloys that exhibit pseudoelasticity may behave very differently.

Electrical resistivity is a material property and for Nitinol, 316 SS, and Ni, they are given in Table 4.2. In contrast, contact area is determined by material strength and hardness, and electrode force. The initial contact area after stage 1 "cold collapse" for the three types of wire was measured and summarized in Table 4.3. In simple terms, larger resistivity and smaller contact area would enable higher heat generation for fusion welding. Hence, Ni wires showed solid-state bonding because of lower resistivity and higher contact area compared to 316 SS.

Table 4.2: Melting temperature and resistivity for various materials

	Melting Temperature (^{o}C)	Resistivity (μΩ·mm)
Austenitic NiTi	1310	820
316 SS	1400	740
Ni	1453	69.3

Table 4.3: Diameter and depth of indentations of the wires at *F* = 5 kg-f

	Diameter (μm)	Z (μm)
NiTi	n/a	n/a
316 SS	141.5 ±4.37	4.20 ±0.16
Ni	175.07 ±3.72	8.2 ±0.1

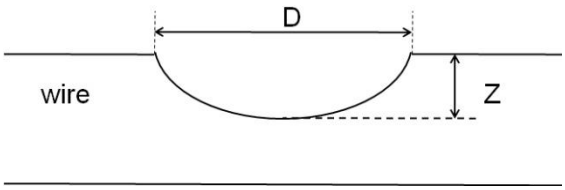

On the other hand, deformation in Nitinol wires could not be properly measured using an optical profiler because of recovery of pseudoelastic strain, which was exemplified from a one-cycle cyclic compression test, shown in Figure 4.15. Permanent strain was observed for 316 SS wires while pseudoelastic responses were observed for Nitinol wires. It can be seen that the nominal contact area (strain at 5 kg-f) was higher for Nitinol, which could be one of the reasons the joining mechanism for this alloy was solid-state despite having similar resistivity as 316 SS. Moreover, at early stages of heating, material expansion was observed in Nitinol but not in 316 SS and Ni wires. The displacement signal for the three types of wires that corresponds to Figure 4.14 is shown in Figure 4.16, with the exception of Ni at which a current of 400 A was used instead to obtain similar displacement. As the temperature in the wires increased, the critical stress became higher than the electrode force applied, which caused the thermodynamic instability of SIM and the recovery of strain as represented by the positive displacement signal (Figure 2.9). Eventually the wires softened due to recrystallization and

gradual increase in set-down occurred. Although the exact role of pseudoelasticity in contact resistance remains unclear, its effects are visible and cannot be neglected. Therefore, a systematic study on the effects of pseudoelasticity on contact resistance with emphasis on the true contact condition, and consideration of film resistance and surface conditions is required to further understand the relationship between material science and process parameters of MRSW of Nitinol and other shape memory alloys.

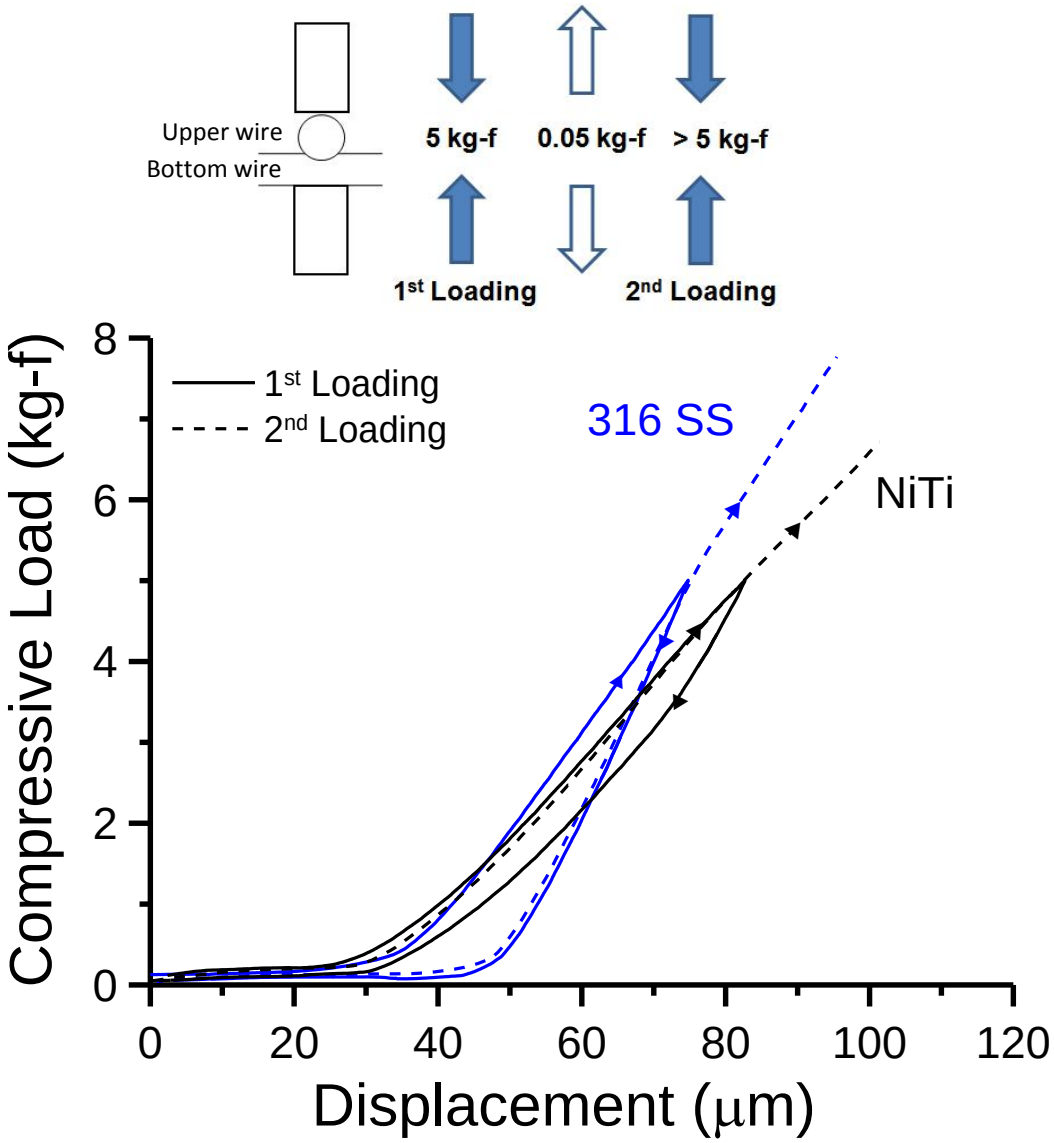

Figure 4.15: Compressive tests on NiTi and 316 stainless steel crossed-wires: (1) load to 5 kg-f, (2) unload to 0.05 kg-f, and (3) load to failure

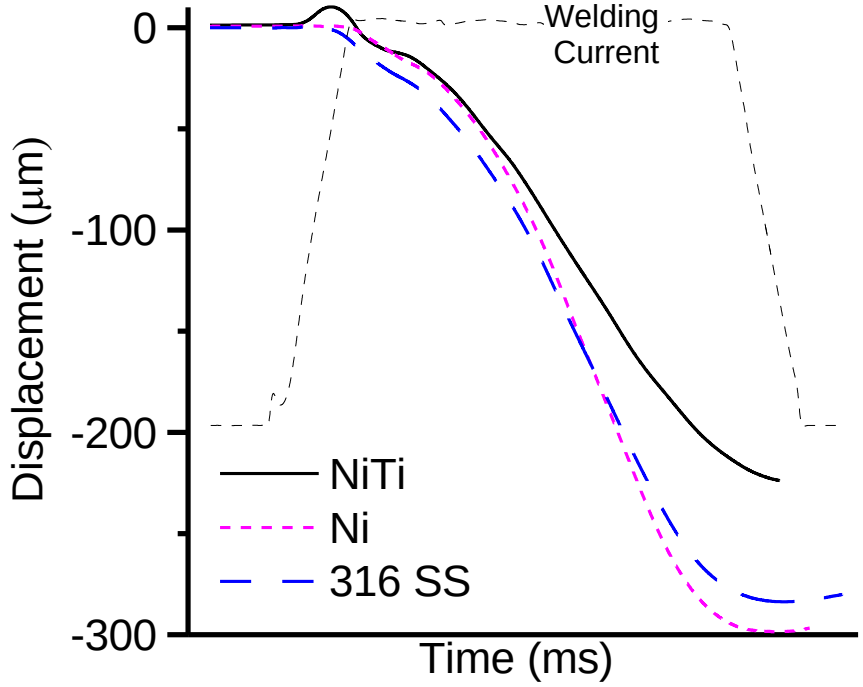

(a)

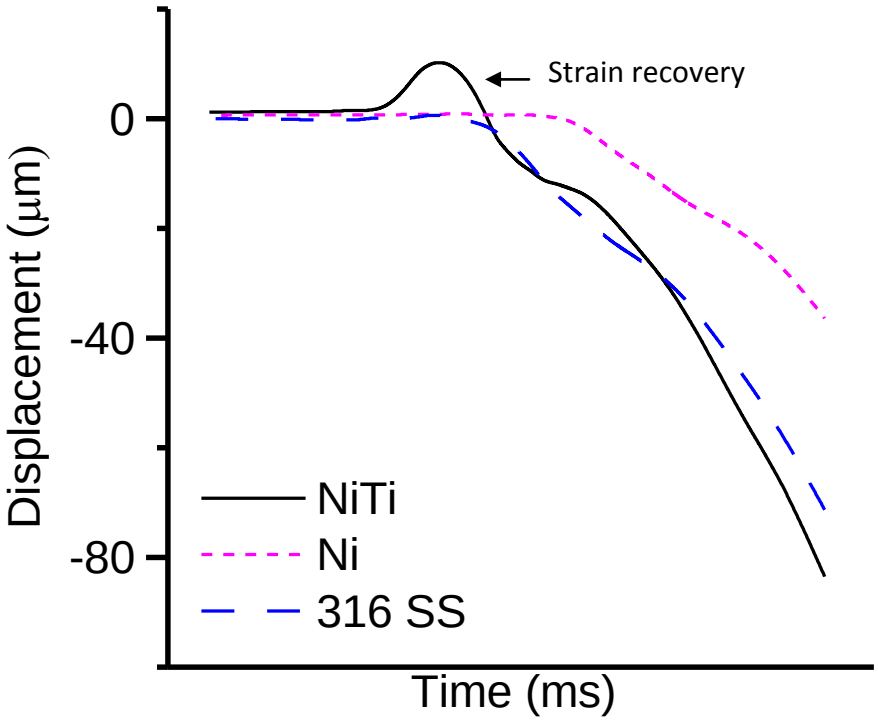

(b) Zoom-in

Figure 4.16: Displacement signal for MRSW of crossed-wires of NiTi (*I* = 200 A), Ni (*I* = 400 A), and 316 SS (*I* = 200 A).

Chapter 5: Laser Micro-Welding of Crossed Nitinol Wires

5.1 Effects of Oxide Removal

By minimizing surface contaminants, joint strength increased substantially from 26 N to 109 N. Although the welded regions could not be differentiated visually from the surface (Figure 5.1), the cross-sectional SEM profiles shown in Figure 5.2, revealed distinct microstructures in the fusion zone. The dendritic structure was easily observed in welds when wires were previously cleaned. In contrast, welds using untreated wire contained dispersed Ti-Ni-O intermetallics, which can act as nucleation sites during solidification, resulting in a change in solidification structure [54-55]. Similar observations have been reported during the production of Nitinol ingots where inclusions of carbon and oxygen must be kept to a minimum [56]. Ti-Ni-O and TiC IMCs have lattice structure of large misfits with Nitinol, creating incoherent precipitates that can cause premature failure.

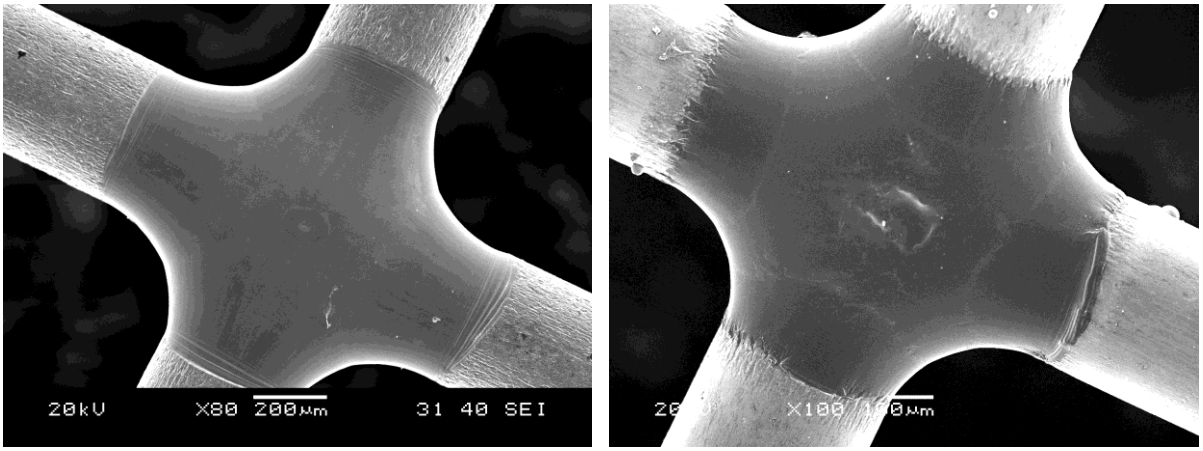

(a) (b)

Figure 5.1: SEM micrographs of welds (a) with and (b) without surface cleaning with acid solution after welding.

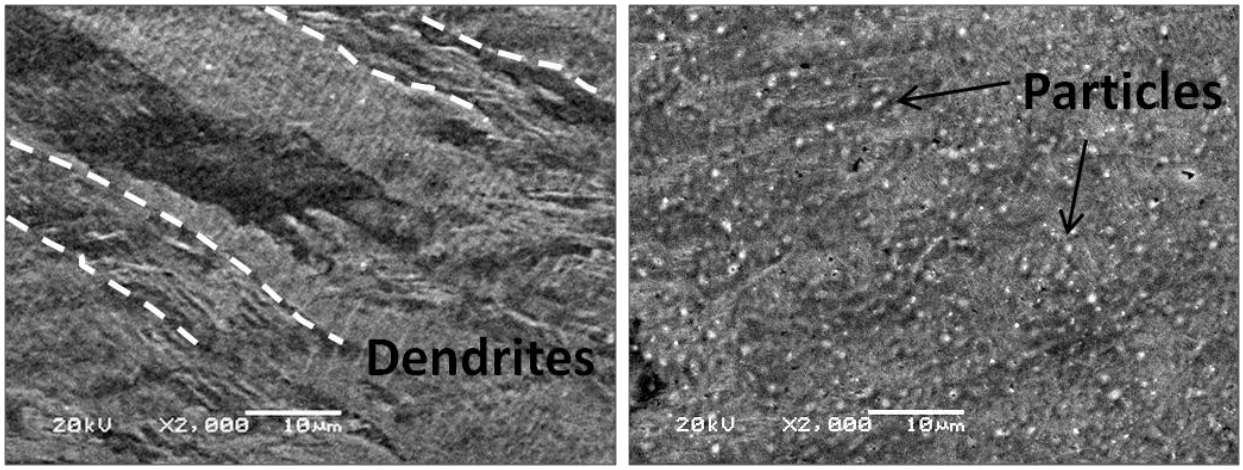

(a) (b)

Figure 5.2: Fusion zones of welds (a) with and (b) without surface cleaning with acid solution.

5.2 Mechanical Behaviours of Welded Joints

Laser welding was found to effectively preserve pseudoelasticity, which was not observed in the previous study implementing the micro-resistance spot welding (MRSW) process. A load-displacement curve of welds produced using LMW and MRSW is shown in Figure 5.3. The three distinct mechanical responses typical to pseudoelasticity were exhibited in the LMW sample, including (1) elastic response of the austenitic phase, (2) stress induced martensite transformation, and (3) elastic/plastic response of martensite upon failure. In contrast, resistance welded crossed-joints fractured prematurely to the formation of SIMs resulting in the lost of pseudoelasticity.

The effect of peak power on the joint breaking force (JBF) of weld specimens is shown in Figure 5.4. A minimum peak power of 0.55 kW was required to produce welds. Near the onset of joining (0.5-0.7 kW) low JBFs were attained. Joint strength increased steadily beyond 0.7 kW, with maximum JBFs of 110-120 N achieved between 0.85 kW and 1.7 kW. The equivalent fracture stress (based on wire diameter) was approximately 70-80% of base metal, comparable to literature [4, 6-7]. Peak powers exceeding 1.7 kW resulted in over-welding.

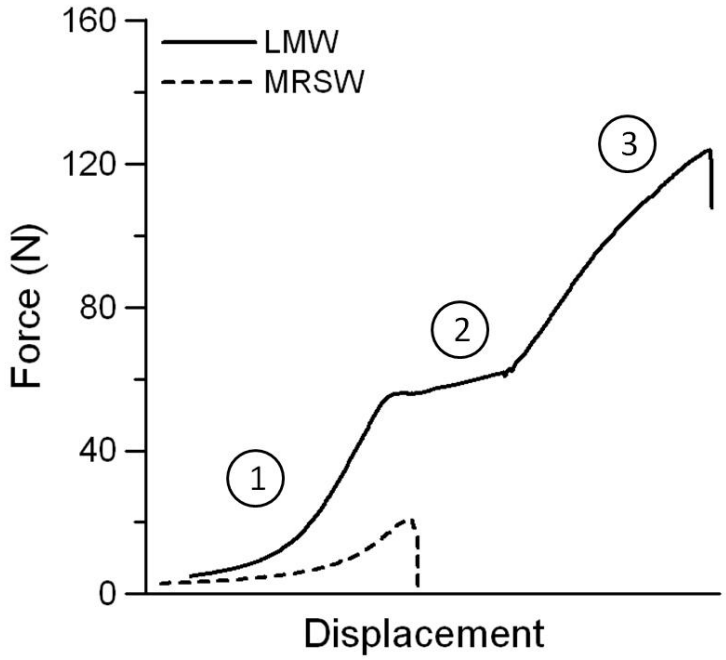

Figure 5.3: Force and displacement curve using 1.0 kW peak power: (1) elastic response of austenite, (2) stress-induced martensite, and (3) elastic/plastic deformation of martensite

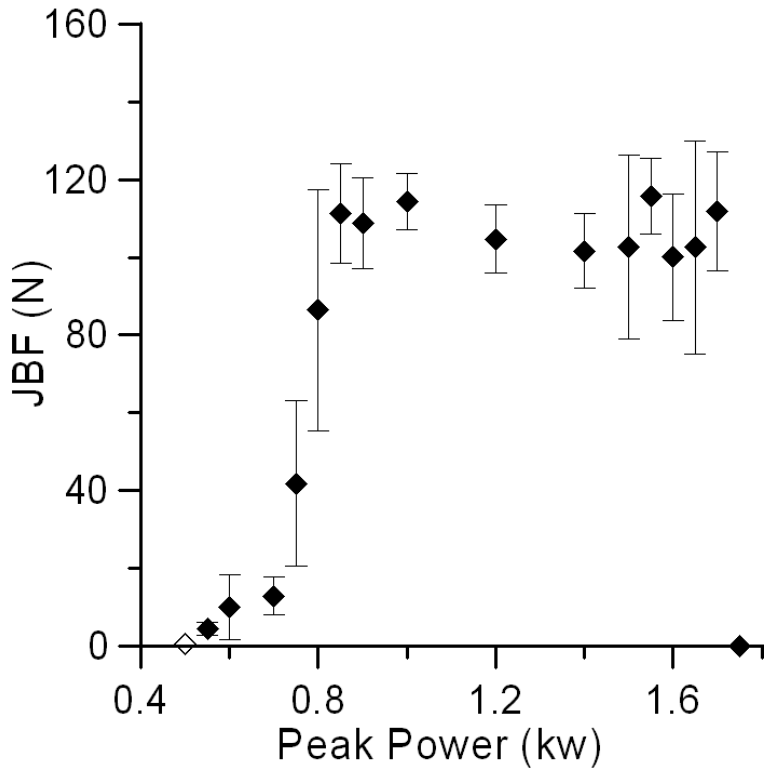

Figure 5.4: Effects of peak power on joint breaking force

5.3 Effects of Peak Power on Joint Formation and Fracture Mechanism

Differences in weld and base metal properties can generally be related to differences in joining mechanisms. During MRSW of Nitinol, resistance heating at the interface promoted solid-state bonding through grain growth. Joint strength was shown to be a function of interfacial bond strength and heat affected zone (HAZ) softening due to recrystallization. In contrast, joining in the current study was primarily fusion based with joint strength depending primarily on weld penetration and growth.

Figure 5.5 shows SEM micrographs of weld using a peak power input of 0.6 kW, which had a low JBF of approximately 10 N. The visible/unmelted bottom wire in Figure 5.5b signified insufficient energy was provided by the incident beam at this condition. Lack of bonding resulted in a notch that served as a site for fracture initiation. This can be observed in Figure 5.5d where a non-bonded region is visible near the weld interface of the fracture surface. Failure then proceeded along the weld metal, characterized by a fine dimpled morphology shown in Figure 5.6b. In contrast, base metal failure exhibited a ductile morphology of larger dimples (Figure 5.6a).

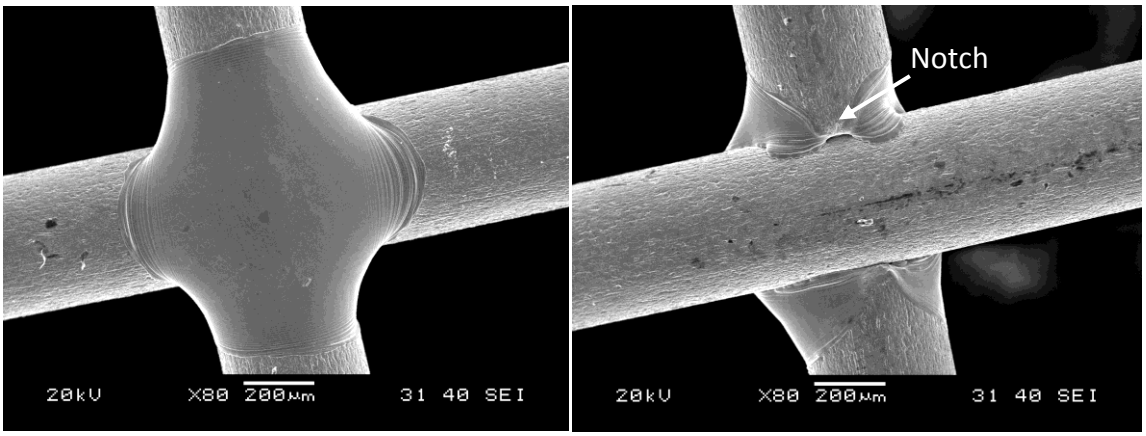

(a) Top of weld (b) Bottom of weld

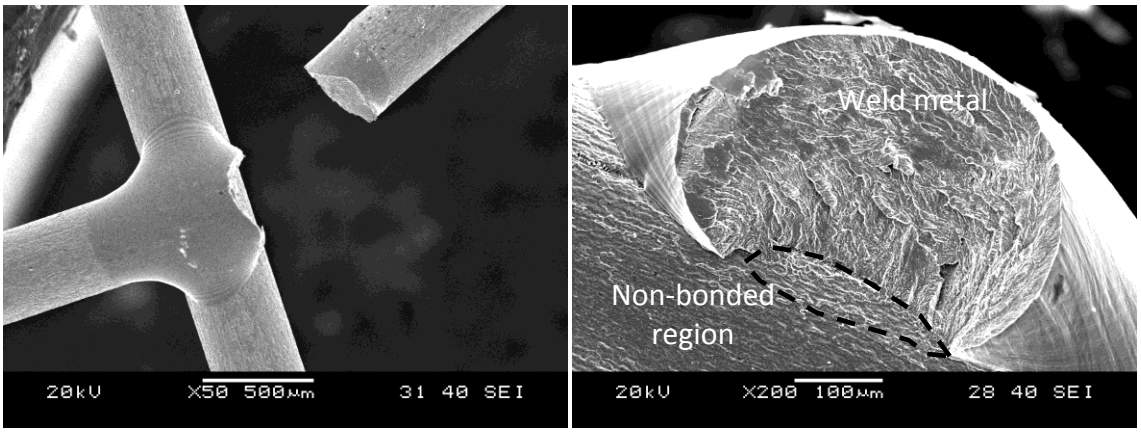

(c) Fractured weld (b) Fracture surface

Figure 5.5: SEM surface of welds made at 0.6 kW peak power

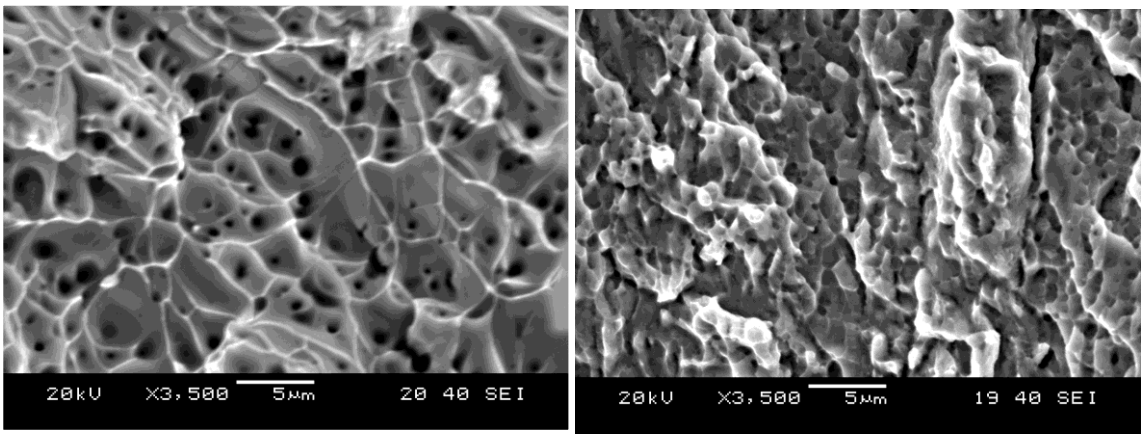

(a) (b)

Figure 5.6: Hi-magnification SEM fracture surfaces of (a) base and (b) weld metal

Full penetration was observed when peak powers above 0.8 kW were applied (Figure 5.7), which was accompanied by a substantial improvement in strength (from 10 N to 80 N). A fusion-zone gradient was clearly visible, with melting at the bottom surface not as pronounced as on the top side (Figure 5.7b). When compared to the 0.6 kW weld, failure transitioned from one wire to through the fusion zone of both wires. (Figure 5.7c and Figure 5.7d).

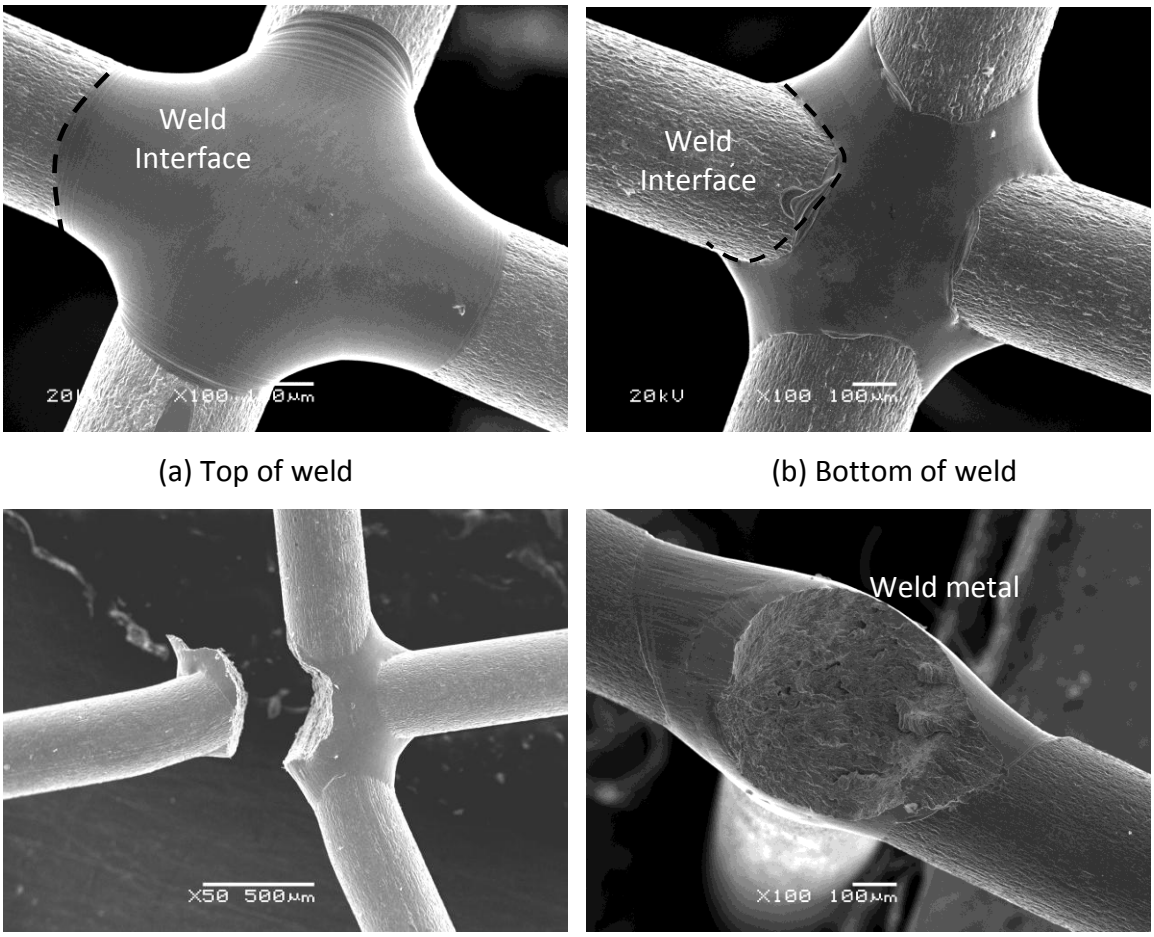

(a) Top of weld (b) Bottom of weld

(c) Fractured weld (b) Fracture surface

Figure 5.7: SEM surfaces of welds made at 0.8 kW peak power

A smoother joint surface was observed when using conditions producing maximum JBF values (0.85 kW to 1.7 kW) (Figure 5.8 and Figure 5.9). In addition to eliminating stress risers, smooth surfaces are essential to in-vivo medical devices for minimizing damage to organs and tissues during implementation and operation [19]. Fracture in these joints proceeded along the base and weld metal at the lower power range (regions are traced out in Figure 5.8d) to only weld metal at the upper power range (Figure 5.9d). Joints were more susceptible to undercutting at high peak power inputs (Figure 5.9a), which reduces local load bearing capacity and this was reflected in the higher standard deviation of strength at high powers in Figure 6. Finally, over-welding was observed when peak powers of 1.75 kW or higher were applied (Figure 5.10).

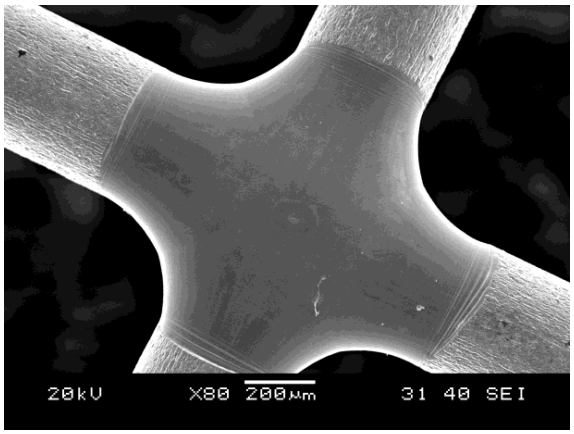

(a) Top of weld

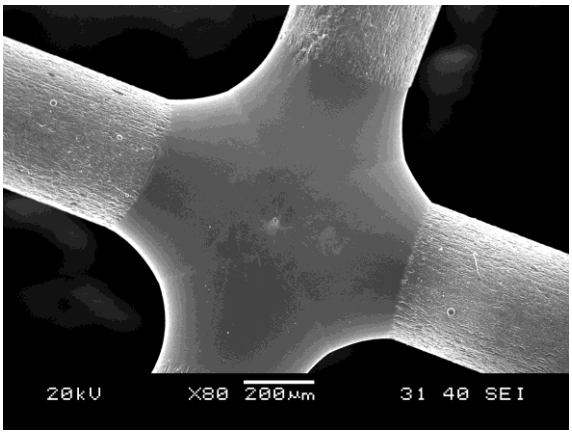

(b) Bottom of weld

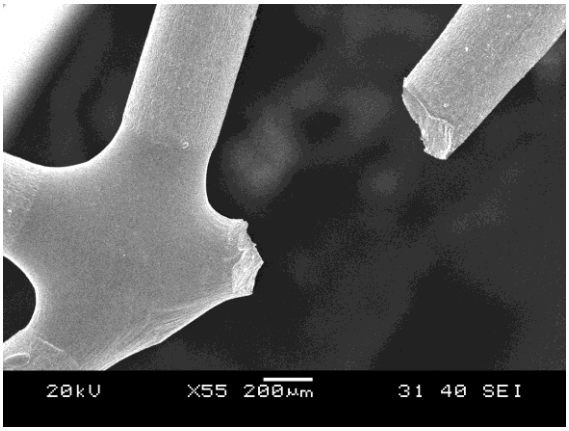

(c) Fractured weld

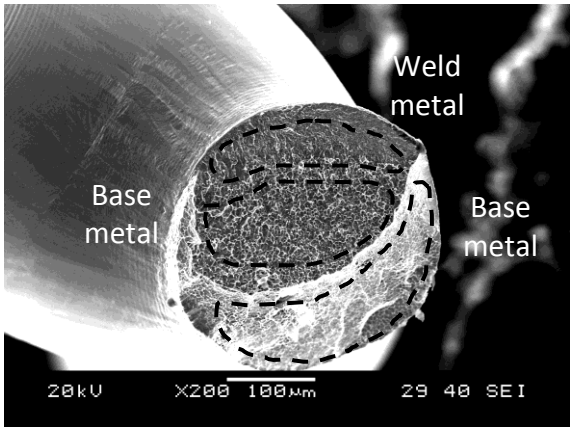

(b) Fracture surface

Figure 5.8: SEM micrographs of welds made at 1.0 kW peak power

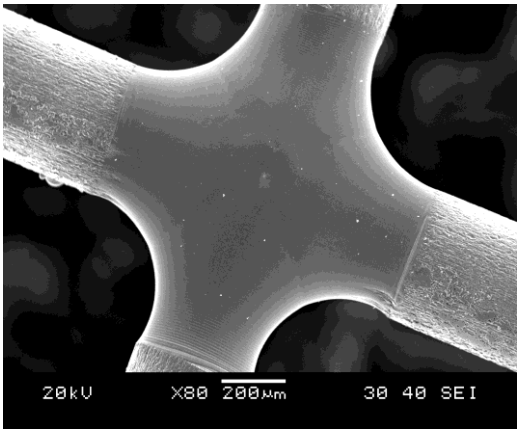

(a)

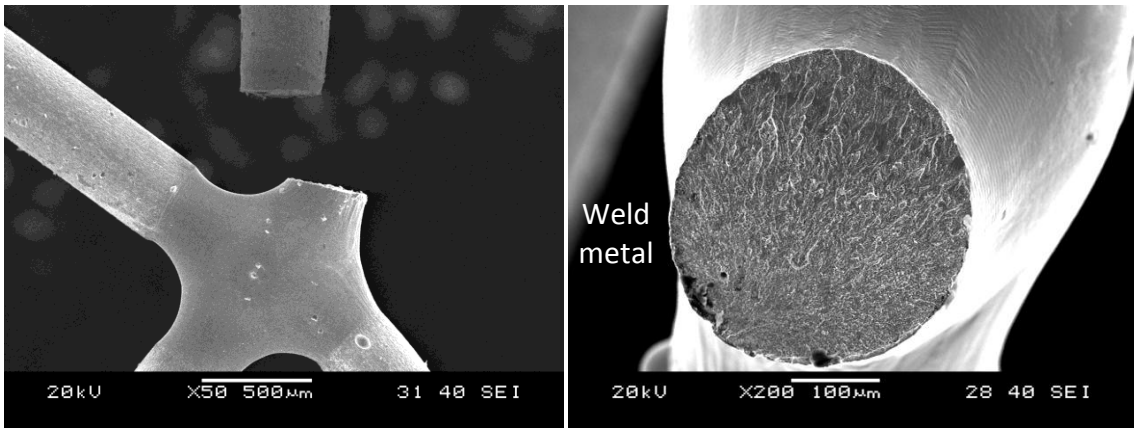

(b) Fractured weld (c) Fracture surface

Figure 5.9: SEM micrographs of welds made at 1.6 kW peak power

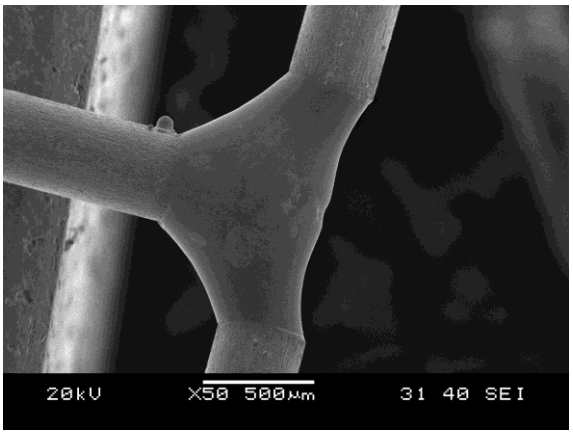

Figure 5.10: SEM micrographs of welds made at 1.75 kW peak power

5.4 Microstructure and Hardness

A cross-sectioned joint made at 0.6 kW is shown in Figure 5.11. Base metal consisted of a fine grained unidirectional structure produced during the cold drawing process. The upper wire that was in contact first with the laser irradiation consisted of a columnar dendritic structure due to rapid solidification from the liquidus temperatures. The bottom wire was partly melted, as shown by the recrystallized microstructure (Figure 5.11b). Lack of bonding was again observed at the peripheral junction of the two wires (Figure 5.11c).

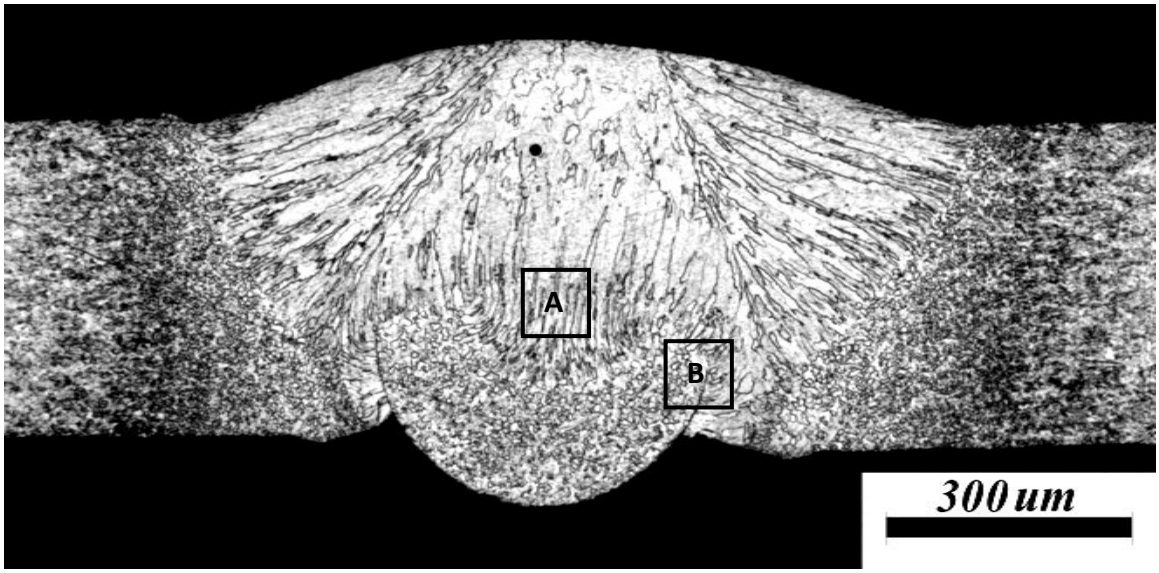

(a) Cross-section

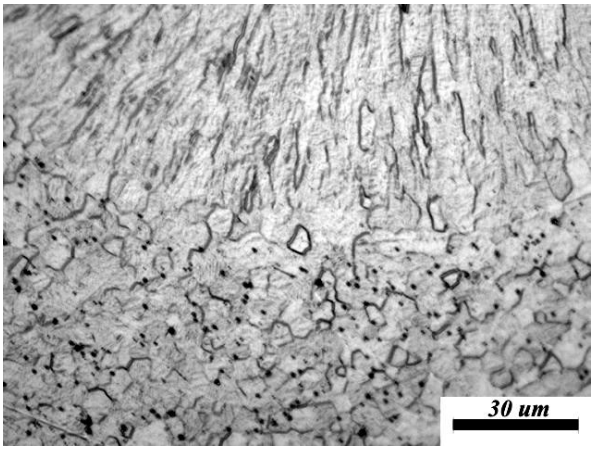

(b) Area A

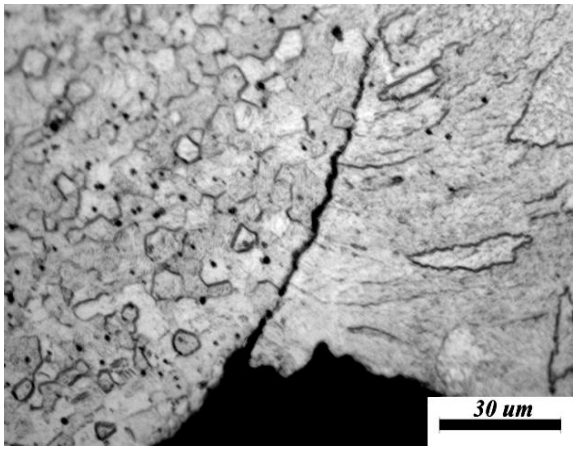

(c) Area B

Figure 5.11: OM Cross-sectioned micrographs of welds made at 0.6 kW peak power

Cross-sectioned views of a weld produced at 1.0 kW showed weld widths at the top and bottom to be more equal (Figure 5.12). The fusion zone consisted of large columnar dendritic grains oriented normal to the centerline, suggesting the primary direction of heat withdrawal was conduction into the wires (Figure 5.12a). At the weld interface, a region of smaller columnar grains formed likely due to competitive growth (Figure 5.12b). Extending away from the fusion zone was a HAZ and finally the fine grained base material. A network of second phase particles

was detected within the fusion zone (Figure 5.12c); these were suspected to be $NiTi_2$ intermetallic as observed in referenced work, but their origin currently remains unclear [7, 8].

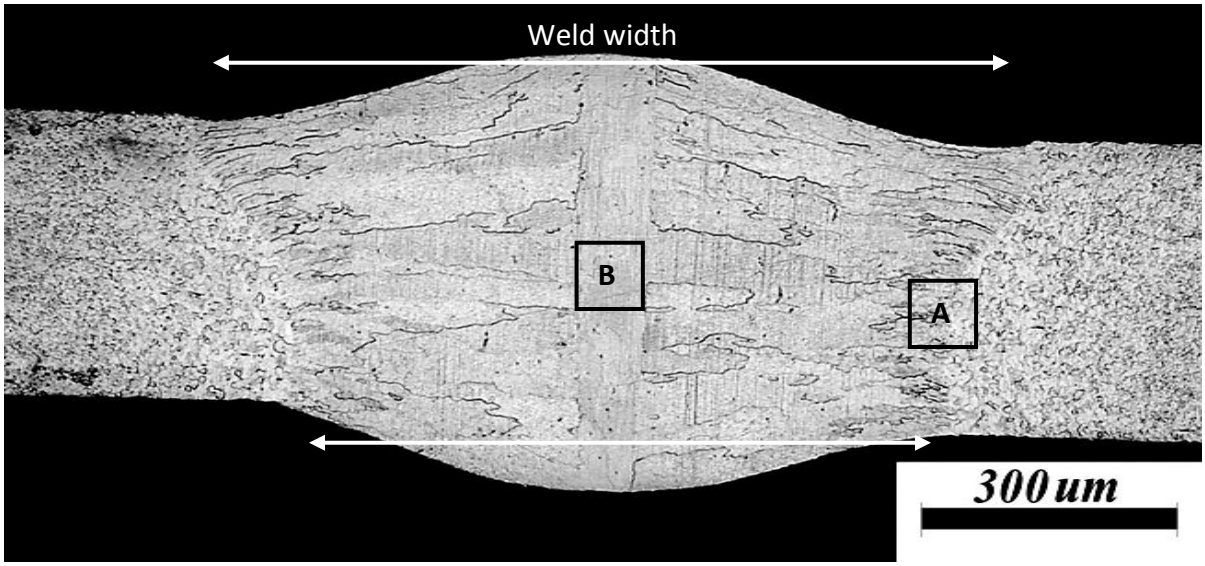

(a) Cross-section

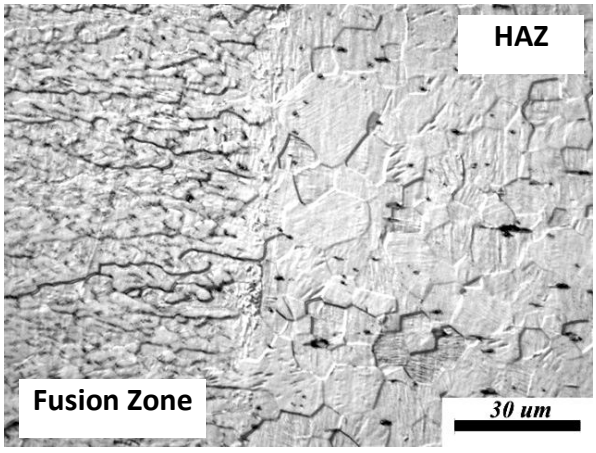

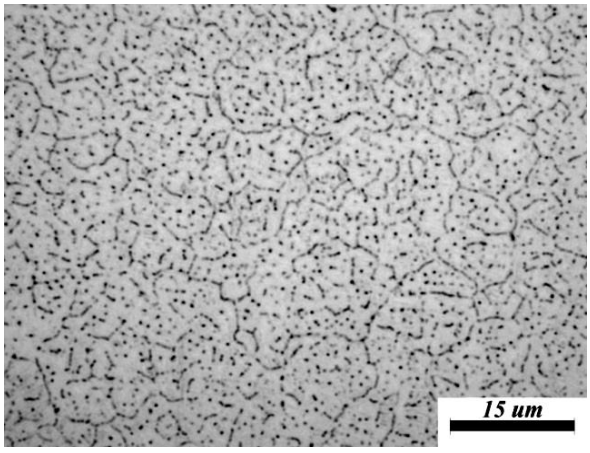

(b) Area A (c) Area C

Figure 5.12: Cross-sectioned micrographs of welds made at 1.0 kW peak power

Further increasing peak powers resulted in a wider fusion zone and HAZ with balanced melting at the top and bottom faces. This trend was clearly observed from the microhardness profiles, shown in Figure 5.13. The base metal had a hardness of 400 Hv while the resolidification structure of the fusion zone experienced a 30% decrease to approximately 280 Hv. Heat

conduction into the wire produced a gradient effect of recrystallization and grain growth of base metal. In turn, this resulted in softening due to the elimination of previous cold working. The increased size of fusion zone and HAZ with increasing peak powers was found to have minimal effects on JBFs as similar fracture strength was maintained between 0.85 kW to 1.7 kW.

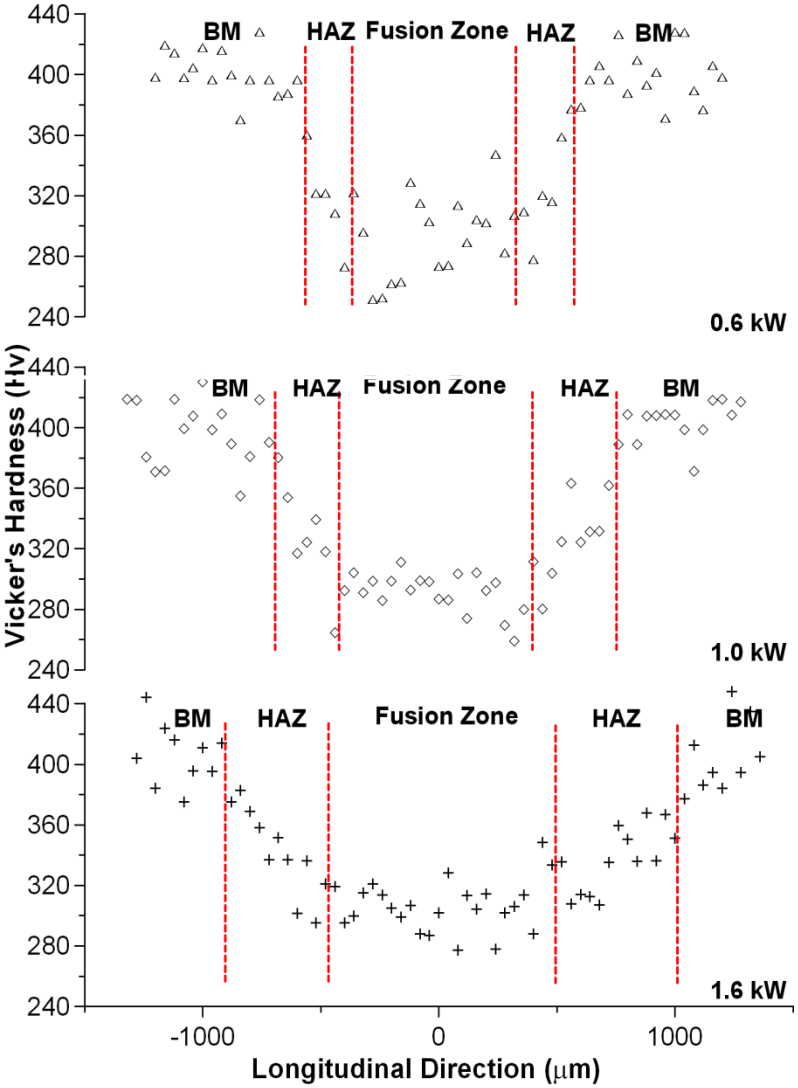

Figure 5.13: Vickers hardness across the fusion zone of welds using peak powers of 0.6 kW, 1.0 kW and 1.6 kW

5.5 Local Phase Transformation in the Welded Joint

DSC curves of base metal, fully annealed base metal, and select welds are shown in Figure 5.14 with respective onset temperatures summarized in Table 3.2 and Table 5.1. At room temperature, base metal primarily consisted of an austenitic structure. Broad temperature peaks of base metal, as a result of the preceding thermomechanical processing during wire fabrication could no longer be observed after welding [22, 35-36]. In comparison, weld metals exhibited multiple transformations, including a pair of distinct high and low temperature peaks. The HAZ can account for the low temperature peaks, which were similar to those of fully annealed wire. Heat conduction through the wires during welding removes the effects of prior cold-working and heat treatments, similar to an annealing process [35-36]. Hence, the low temperature peaks were more prominent for the 0.6 kW sample because of the additional contribution of the recrystallized base metal of the bottom wire (Figure 5.11).

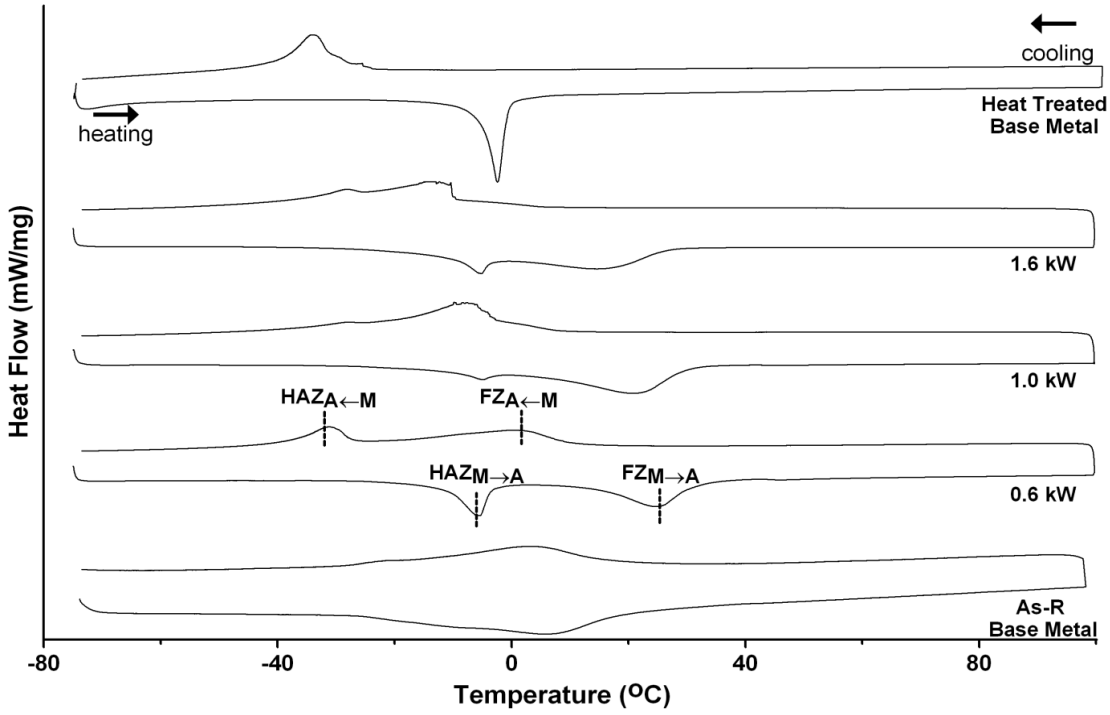

Figure 5.14: DSC curves for as-received base metal, heat treated base metal and welds using peak powers of 0.6 kW, 1.0 kW and 1.6 kW.

Table 5.1: Temperature onsets of phase transformations in welds using select peak powers

	HAZ		Fusion Zone	
	M_s (°C)	A_f (°C)	M_s (°C)	A_f (°C)
0.6 kW	-27.46	-3.49	12.57	38.44
1.0 kW	-24.12	-3.04	7.74	34.16
1.6 kW	-27.49	-3.81	5.68	28.36

The distinct peaks of the fusion zones at high temperatures, denoted by FZ peaks in Figure 16 suggested modification to the original crystal structure. Onset temperatures, M_s and A_f, of the fusion zones were in the range of 5-13^{o}C and 28-38^{o}C, respectively, with a common transformational hysteresis near 20-25^{o}C [1]. The modification to phase transformation temperatures varied with peak power inputs, showing that different welding parameters may have different effects on the transformation temperatures.

Room temperature XRD analysis of fusion zones confirmed the phase conversion induced by LMW of Nitinol. Two conditions were tested for the 1.0 kW weld including heating above A_f and cooling to room temperature (*condition 1*) and cooling below Ms and heating to room temperature (*condition 2*). As expected from the DSC data, base material produced peaks corresponded to the B2 structure of austenite (Figure 5.15a). Similarly, *condition 1* retained a homogeneous austenitic structure (Figure 5.15b). However, the co-existence of austenite and martensite at room temperature was detected for *condition 2* (Figure 5.15c). This is due to the transformational hysteresis of the fusion zone, in which the structure can be thermally conditioned between A_s and A_f resulting in incomplete martensite-to-austenite transformation at room temperature.

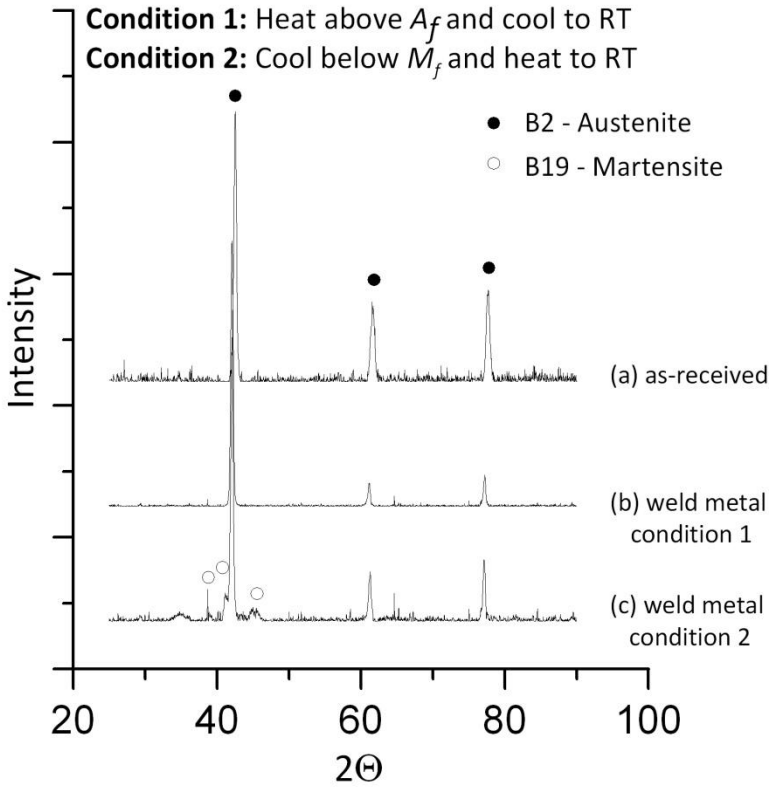

Figure 5.15: Room temperature XRD results for (a) as-received base metal and weld metal (1.0 kW) of (b) *condition 1* and (c) *condition 2*

The current result combined with those of MRSW of Nitinol showed welding has a significant impact on the phase transformation behaviour of Nitinol. The effects were different and could be correlated to the different joining mechanisms: fusion in LMW and solid-state in MRSW. In the MRSW process, resistance heating anneals the original base metal, producing a HAZ that mimics solid-state solution treatment. Changes to the transformation temperatures of LMW welds can be more complex due to their dependency on the microstructural state of base material (i.e. whether it was aged or solution-treated) [9]. Moreover, formation of common intermetallics (Ni_3Ti, $NiTi_2$) can alter the Ni to Ti ratio, which can dictate the intrinsic phase transformation temperatures [1]. Modifications can also occur from the difference in grain orientation and size of the solidification structure [57-58]. However, current results showed an increase in phase transformation temperatures, although not as substantial as those reported in literature [4, 14]. Discrepancies may be attributed to the differences in thermomechanical

treatment history or process parameters, which may result in different welding modes and physical behaviours of the material, described in Sect. 2.2.2 and Sect. 2.2.4 [42]. However, it should not be forgotten that the aforementioned ways of adjusting phase transformations will also have a direct influence on the pseudoelastic properties as shown here and in literature [14]. Therefore, in-depth microstructural analysis such as high resolution field emission SEM or transmission electron microscopy (TEM) is necessary to uncover the missing links for explaining the observed phenomena.

Chapter 6: Conclusions

6.1 MRSW of Crossed NiTi Wires

Resistance spot welding of crossed Nitinol wires was investigated by studying the mechanical properties, microstructures and phase transformation. Bonding mechanisms were detailed with micrographs along with images of the fracture modes. The main conclusions include the following:

1. Surface cleaning was essential in MRSW of Nitinol. The relative difference in interfacial peak resistance at the electrode-to-wire interfaces compared to wire-to-wire interface allowed heat to generate at the faying surface, minimizing electrode-wire sticking.
2. The bonding mechanism of MRSW of crossed Nitinol wires was predominantly a solid-state bonding process with 6 main stages: 1) cold collapse; 2) dynamic recrystallization; 3) interfacial melting; 4) squeeze out; 5) excessive flash; and 6) surface melting.
3. Fracture modes transitioned from interfacial failure at low current to partial-interfacial failure at intermediate current, and finally, to HAZ failure at high current. Maximum joint breaking force was attained by balancing the competing factors of increasing interfacial bond strength and softening in the HAZ.
4. Heat generated during the welding process locally annealed the previously strain hardened base material, which altered the transformation temperatures of weld metal from near room temperature to sub-ambient. The transformation temperatures of weld metal were similar to those of solution treated material.

6.2 LMW of Crossed NiTi Wires

The current study analyzed the effects of Nd:Yag laser welding on the mechanical and phase transformation behaviours of crossed Nitinol wires. Joint formation was also observed via metallurgical observations. The main findings include the following:

1. Removal of surface contaminants such as oxides is essential to laser welding of Nitinol. Entrapment of contaminants in the weld microstructure can reduce the mechanical strength significantly.
2. Weld in crossed NiTi wires welds possessed excellent strength and were able to retain pseudoelasticity as compared to the RMW process.
3. Fracture surfaces of base and weld metals revealed dimpled ductile surfaces. Failure mode was strongly dependent on the weld morphology. At low peak power inputs, failure was initiated by welding defects. At the power range where max JBF was obtained, failures occurred along the base and weld metals in the lower end and weld metal in the upper end.
4. The microstructure of crossed Nitinol wires consisted of columnar dendritic structure in the fusion zone and a recrystallized structure in the HAZ. Both fusion zone and HAZ grew with increased peak power inputs. Hardness was reduced 30% in the fusion zone compared to base metal but was found to be insignificant to the overall fracture strength.
5. Phase transformation behaviour in the HAZ and Fusion zone was altered, induced by the laser welding process. The HAZ exhibited an intrinsic phase transformation behaviour due to the annealed structure that mimicked solution treated Nitinol. The fusion zone showed phase transformations at higher temperatures, and could be thermally conditioned to have a structure of predominantly austenite or a mixture of martensite and austenite at room temperature.

6.3 Recommendations for Future Work

Nitinol wires of a single composition were used throughout this study. Nitinol alloys are typically classified as either Ni-rich or Ti-rich; the former was studied. Ti-rich Nitinol alloys are used because of the wider temperature range in which martensite is stable; however, solidification cracking during rapid solidification can be a problem. As a result, the MRSW and LMW of Ti-rich Nitinol should also be studied thoroughly.

In the MRSW study, the primary joining mechanism of Nitinol was solid-state. Welding defects were detrimental to the joint strength, which caused the loss of pseudoelasticity. Preliminary study has found that the pseudoelasticity affected the contact resistance, which could lead to a change in heat generation. However, its role still remained unclear and further investigation is required. One possible way is to perform MRSW of Nitinol at an elevated temperature above M_d, at which austenite no longer exhibits the pseudoelastic behaviour.

Laser micro-welded Nitinol was found to have altered functional properties, as shown by the enabling of shape memory effect at room temperature due to the co-existence of austenite and martensite. Results also showed different welding parameters have different effects on the modification to the original crystal structure and phase transformation behaviours. A parametric study on the effects of welding parameters (welding current, welding time, defocus distance) on Nitinol combined with detailed microstructural analysis such as high-resolution SEM or TEM should improve the fundamental understanding of LMW of Nitinol.

Lastly, Nitinol-based applications are generally used in harsh environment such as high temperature and pressure for aerospace applications, and in-vivo for medical device applications. Long term reliability study in elevated temperature and in-vitro electrochemical testing of corrosion properties are all studies that are lacking and required to maximize the usefulness of welded Nitinol.

References

1. G. B. Kauffman, I. Mayo, The story of Nitinol: The serendipitous discovery of the memory metal and its applications, The Chemical Educator, 1997, vol. 2(2), 1-21.
2. T. W. Duerig, K. N. Melton, D. Stockel, C. M. Wayman, Engineering aspects of shape memory alloys, Butterworth-Heinemann, 1990.
3. J. V. Humbeeck, Shape memory alloys: a material and a technology, Advanced Engineering Materials, 2001, vol. 3(11), 837-850.
4. D. Stoeckel, A. Pelton, T. Duerig, Self-expanding Nitinol stents: material and design considerations, Eur Radiol, 2004, vol. 14, 292-301.
5. D. Hodgson, S. Russell, Nitinol melting, manufacture and fabrication, Minimally Invasive Therapy and Allied Technologies, 2000, vol. 9(2), 61-66.
6. X. J. Yan, D. Z. Yang, X. P. Liu, Influence of heat treatment on the fatigue life of a laser-welded NiTi alloy wire, Materials Characterization, 2007, vol. 58, 262-266.
7. M.I. Khan, S.K. Panda, Y. Zhou, Effects of welding parameters on the mechanical performance of laser welded Nitinol, Materials Transactions, 2008, v 49, 2702-2708.
8. P. Scholossmacher, T. Haas, A. Schüssler, Laser-welding of a Ni-rich TiNi shape memory alloy: mechanical behaviour, Journal de Physique Colloque C5, 1997, 251-256.
9. Y. Ogata, M. Takatugu, T. Kunimasa, K. Uenishi, K. F. Kobayashi, Tensile strength and pseudo-elasticity of YAG laser spot melted Ti-Ni shape memory alloy wires, Materials Transactions, 2004, vol. 45, 1070-1076.
10. Y.T. Hsu, Y.R. Wang, S.K. Wu and C. Chen, Effect of CO_2 laser welding on the shape - memory and corrosion characteristics of TiNi alloys, Metallurgical and Materials Transactions A, 2001, vol. 32A, 569–576.
11. A. Tuissi, S. Besseghini, T. Ranucci, F. Squatrito and M. Pozzi, Effect of Nd-YAG laser welding on the functional properties of the Ni–49.6 at.% Ti, Material Science and Engineering A, 1999, A 273–275, pp. 813–817.

12. A. Falvo, F. M. Furgiuele, C. Maletta, Laser welding of a NiTi alloy: mechanical and shape memory behaviour, Materials Science and Engineering A, 2005, vol. 412, 235-240.
13. M. Nishikawa, H. Tanaka, M. Kohda, T. Nagaura, K. Watanabe. Behaviour of welded part of Ti-Ni shape memory alloy, Journal De Physique Colloque C4 Supplement, 1982, vol. 12(C4),839-844.
14. J. Beyer, P. A. Besselink, J. H. Lindenhovius. Shape memory and microstructure of welded TiNi alloy, Shape Memory Alloys Proceedings of the International Symposium, 1986, 492-497.
15. P.C. Hall, Resistance welding Ti-rich Nitinol wire, SMST-2000: The International Conference on Shape Memory and Superelastic Technologies, Pacific Grove, CA, USA, 2000, 67-75.
16. M. I. Khan, Y.Zhou, Effect of local phase conversion on the tensile loading of Pulsed Nd:YAG laser processed Nitinol, Materials Science and Engineering A, 2010 (Accepted).
17. S. Fukumoto, Y. Zhou, Mechanism of resistance microwelding of crossed nickel wires. Metallurgical and materials Transactions A, 2004, vol. 35A, 3165-3176.
18. S. Fukumoto, H. Tsubakino, Y. Zhou, Heat input and deformation control in resistance microwelding of fine nickel wires. Welding International, 2006, vol. 20(9), 692-697.
19. S. Fukumoto, Z. Chen, Y. Zhou, Interfacial phenomena and joint strength in resistance microwelding of crossed Au-plated Ni wires, Metallurgical and Materials Transactions A, 2005, vol. 36A, 2717-2724.
20. S. Fukumoto, T. Matsuo, H. Tsubakino, A. Yamamoto, Resistance microwelding of SUS304 stainless steel fine wires, Materials Transactions, 2007, vol. 48(4), 813-820.
21. M. I. Khan, J. M. Kim, M. L. Kuntz, Y. Zhou, Bonding mechanisms in resistance microwelding of 316 low-carbon vacuum melted stainless steel wires, Metallurgical and Materials Transactions A, 2009, vol. 40A, 910-919.
22. W. Tan. Small-scale Resistance Spot Welding of Thin Nickel Sheet, PhD. Thesis, University of Waterloo, Waterloo, Ontario, Canada (2004).
23. K. Kuita, H. Matsumoto, H. Abe, Transformation behavior in rolled Nitinol, Journal of Alloys and Compounds, 2004, vol. 381, 158-161.

24. C. P. Frick, A. M. Ortega, J. Tyber, A. El. M. Maksound, H. J. Maier, Y. Liu, K. Gall, Thermal processing of polycrystalline Nitinol shape memory alloys, Materials Science and Engineering A, 2005, vol. 405, 34-49.

25. T. Saburi, T. Tatsumi, S. Nenno, Effects of heat treatment of mechanical behaviour of Ti-Ni alloys. Journal De Physique Colloque C4 Supplement, 1982, vol. 12(C4), 261-266.

26. W. Kiattiwongse, A. Khantachawana, P. Santiwong, Effect of direct electric resistance heat treatment on mechanical properties of Nitinol orthodontic arch wires, Advanced Materials Research, 2008, vol. 55-57, 249-252.

27. M. Fujio, M. Masakuni, Y. Ohura, Japanese Nitinol alloy wire: use of the direct electric resistance heat treatment method, European Journal of Orthodontics, 1988, vol. 10, 187-191.

28. W. W. Duley, Laser Welding, John Wiley & Sons,1999.

29. C. Dawes, Laser Welding, McGraw-Hill, 1992.

30. ASTM Standard F2005, Standard Terminology for Nickel-Titanium Shape Memory Alloys, ASTM International, West Conshohocken, PA, 2009.

31. ASTM Standard F2004, Standard Test Method for Transformation Temperature of Nickel-Titanium by Thermal Analysis, ASTM International, West Conshohocken, PA, 2009.

32. Y. Liu, Z. Xie, J. Van Humbeeck, and L. Delaey, Some results on the detwinning process in Niti shape memory alloys, Scripta Materialia, 1999, vol. 41(12), 1273-1281.

33. M. I. Khan, Pulsed Nd:YAG laser welding of Nitinol, Comprehensive examination, University of Waterloo, Waterloo, Ontario, 2008.

34. R. E. Reed-Hill, R. Abbaschian, Physical Metallurgy Principles: Third Edition, PWS Publishing Company, Boston, USA, 1994.

35. K. Otsuka, X. Ren, Physical metallurgy of Ti-Ni-based shape memory alloys, Progress in Materials Science, 2005, vol. 50, 511-678.

36. C. P. Frick, A. M. Ortega, J. Tyber, A. El. M. Maksound, H. J. Maier, Y. Liu, K. Gall, Thermal processing of polycrystalline NiTi shape memory alloys. Materials Science and Engineering A, 2005, vol. 405, 34-49.

37. D. A. Miller, D. C. Lagoudas. Influence of cold work and heat treatment on the shape memory effect and plastic strain development of NiTi, Materials Science and Engineering A, 2001, vol. 308, 161-175.
38. H. Matsumoto, Transformation behaviour of NiTi in relation to thermal cycling and deformation, Physica B, vol. 1993, vol. 190, 115-120.
39. Y. Zheng, F. Jiang, L. Li, H. Yang, and Y. Liu, Effect of ageing treatment on the transformation behaviour of Ti-50.9 at.% Ni alloy, Acta Materialia, 2008, vol. 56, 736-745.
40. R. C. Crafer and P. J. Oakley, Laser Processing in Manufacturing, Chapman & Hall, 1993.
41. Population inversion, Wikipedia, http://en.wikipedia.org/wiki/Population_inversion, 2010.
42. Spontaneous Emission, Wikipedia, http://en.wikipedia.org/wiki/Spontaneous_emission, 2010.
43. Stimulated Emission, Wikipedia, http://en.wikipedia.org/wiki/Stimulated_emission, 2010.
44. Y. Zhou, Microjoining and Nanojoining, Woodhead Publishing Ltd., Cambridge, England, 2008.
45. M. I. Khan. Spot welding of Advanced High Strength Steels, MASc. Thesis, University of Waterloo, Waterloo, Ontario, Canada (2007).
46. D. Baker, D. C. Koehler, W. O. Fleckenstein, C. E. Roden, Physical design of electronic systems vol. 3, integrated device and connection technology, Prentice-Hall, Inc., Englewood Cliffs, NJ, 1971.
47. J. G. Kaiser, G. J. Dunn, T . W. Eagar, The effect of electrical resistance on nugget formation during spot welding. Welding Research Supplement, 1982, 167s-174s.
48. B. H. Chang, M. V. Li, Y. Zhou, Comparative study of small scale and 'large scale' resistance spot welding, Science and Technology of Welding and Joining, 2001, vol. 6(5), 1-8.
49. R. Holm, Electric Contacts, Theory and Applications, Berlin, Springer-Verlag, 1976.
50. P. G. Slade, Electrical Contacts Principles and Applications, New York. 1999.

51. P. H. Thornton, A. R. Krause, R. G. Davies, Contact resistances in spot welding, Welding Research Supplement, 1996, vol. 75(12), 402s-412s.
52. X. Li, J. Xie, Y. Zhou, Effects of oxygen contamination in the argon shielding gas in laser welding of commercially pure titanium thin sheet, Journal of Materials Science, 2005, vol. 40, 3437-3443.
53. S. J. Dong, G. P. Kelkar, Y. Zhou, Electrode sticking during micro-resistance welding of thin metal sheets, IEEE Transactions on Electronics Packaging Manufacturing, 2002, vol. 25(4), 355-361.
54. Z. Zhang, J. Frenzel, K. Neuking, G. Eggeler, On the reaction between Nitinol melts and crucible graphite during vacuum induction melting of Nitinol shape memory alloys, Acta Materialia, 2005, vol. 53, 3971-3985
55. F. Jiang, L. Li, Y. Zheng, H. Yang, Y. Liu, Cyclic ageing of Ti-50.8at.% Ni alloy, Intermetallics, 2008, vol. 16, 394-98
56. G. S. Firstov, R. G. Vitchev, H. Kumar, B. Blanpain, J. Van Humbeeck, Surface oxidation of NiTi shape memory alloy, Biomaterials, 2002, vol. 23 (24), 4863-4871
57. V. G. Chuprina, I. M. Shalya, Reactions of TiNi with oxygen, Power Metallurgy and Metal Ceramics, 2002, vol. 41(1-2), 85-89
58. S. K. Sadrnezhaad, S. B. Raz, Effect of microstructure on rolling behaviour of NiTi memory alloy, Materials and Manufacturing Processes, 2008, vol. 23(7), 640-650
59. H. Sehitoglu, R. Hamilton, D. Canadinc, X. Y. Zhang, K. Gall, I. Karaman, Y. Chumlyakov, J. J. Maier, Detwinning in NiTi alloys, Metallurgical and Materials Transactions A., 2003, vol. 34 ,5-13
60. F. J. Gil, J. M. Manero, J. A. Planell, Effect of grain size on the martensitic transformation in NiTi alloy, Journal of Materials Science, 1995, vol. 30, 2526-2530